The use of orthogonal bremsstrahlung beams for imaging in radiation therapy

Arman Sarfehnia

Department of Medical Physics
McGill University, Montreal
April, 2006

A thesis submitted to the Faculty of Graduate Studies and Research in partial fulfillment of the requirements of the degree of Master of Science in Medical Radiation Physics

Your file Votre référence
ISBN: 978-0-494-28527-5
Our file Notre référence
ISBN: 978-0-494-28527-5

To both my grandfathers, Rostam and Aflatoon, who were strong and fought hard, though both lost their beautiful lives to cancer. I will remember you forever.

ABSTRACT

Since portal images are created by megavoltage, forward-directed bremsstrahlung beams, their image quality is inferior to that of images produced by kilovoltage beams. In this study, characteristics of orthogonal bremsstrahlung photons produced by megavoltage electron beams were studied and their suitability for radiotherapy imaging was evaluated. Orthogonal bremsstrahlung beams with kilovoltage effective energies can be obtained from megavoltage electrons striking low atomic number targets. A 10 MeV electron beam emerging out of the research port of a Varian Clinac-18 linac was made to strike carbon, aluminum and copper targets. Percentage depth dose and attenuation measurements of forward and orthogonal beams were performed, and experimental results were compared with Monte Carlo-calculated findings. Images of simple contrast objects taken using the orthogonal bremsstrahlung beams showed superior contrast levels in comparison to those produced by the forward beams.

ABRÉGÉ

Puisque les images portales sont crées par des faisceaux de photons bremsstrahlung émis vers l'avant avec des énergies dans les mégavolts, la qualité d'image obtenue est inférieure à celle d'images produites avec des énergies dans les kilovolts. Nous avons étudié des photons produits orthogonalement par des électrons ayant des énergies dans les mégavolts et la pertinence d'utiliser ces photons pour améliorer l'imagerie. Des électrons de 10 MeV, sortant du port de recherche d'un linac Clinac-18 de Varian a été dirigé vers des cibles en carbone, aluminium et cuivre. Nous avons mesuré et calculé à l'aide de Monte Carlo, la PDD et l'atténuation des faisceaux dirigés vers l'avant ainsi que dans la direction orthogonale. Des faisceaux de bremsstrahlung orthogonaux dont l'énergie effective est dans les kilovolts peuvent être obtenus à partir d'électrons dans les mégavolts frappant des cibles dont le numéro atomique est petit.

ACKNOWLEDGMENTS

First and foremost, I would like to thank Dr. Ervin Podgorsak for the wonderful program he has created here at McGill over the 25 years of his directorship in this department. I would also like to thank him because he was one of my most inspiring teachers and a great supervisor. This project could not have gone so smoothly without his expertise and his immense knowledge in the field, as well as his patience to teach me and guide me every step of the way.

Many thanks also to Dr. Jan Seuntjens. I truly do appreciate all the help, support, and guidance that I received from him throughout this project. He was always there for me and never hesitated to answer my questions and address my problems. I would also like to thank my good friend, Keyvan Jabbari, who also never hesitated to sit down and discuss the expected spectrum of the orthogonal bremsstrahlung beams with me.

This project would not have been possible without the help of the three engineers of the oncology department of the Montreal General Hospital: Pierre Leger, Vlad Bobea, and Joe Larkin. Moreover, I would like to express my sincere thanks to Robin Van Gils, the electro-mechanical technician of the medical physics unit.

I would like to acknowledge all the assistance that I received from Dr. Wamied Abdel-Rahman. He helped me especially during my first year of studies here at McGill and managed to always find the time to answer my seemingly never-ending questions.

I would like to express my gratitude to Margery Knewstubb, the department secretary, as well as all the staff, professors, and clinical physicists for their help, support, and smiles. I am fascinated at how everyone in this department loves what they are doing, and I believe that is the true strength of this department.

My sincere thanks to all my colleagues and fellow students, both at the masters and the PhD level, for their support. I know that it would have been much more difficult to continue the program without their academic-related as well as moral support.

Two special friends Jongmin Cho and Peter Petric I must also thank since they encouraged me to come to McGill and told me much about the program and life in Montreal. Also, I appreciate Jongmin's graduation gift: A frame with the following quote by Emerson on it "Do not go where the path may lead, go instead where there is no path and leave a trail". I wish my friend knew what a great impact his gift has had on my life.

I would also like to acknowledge the moral support that I received from my family without whom none of this would have been possible. It was only through their encouragements and continuous support that I have been able to go on and discover the field I truly like.

And most importantly, I thank the Lord Almighty, the One who created all things and who has a reason behind them also. Much in my life I do not comprehend and I simply accept, but this I comprehend that it is solely my faith in Him that makes me strong and that gives me a reason to go on and challenge myself. I humbly thank Him who gave me all that I have and much more.

TABLE OF CONTENTS

LIST OF TABLES

LIST OF FIGURES

Chapter 1

INTRODUCTION

1.1 Preface

The beginning of diagnostic imaging and radiation oncology was marked by Wilhelm Conrad Roentgen. Shortly after the discovery of x rays in November of 1895 by Roentgen, the potential use of these beams for diagnostic purposes became apparent. Further discoveries of natural radioactivity by Becquerel in 1896 and of radium by Marie and Pierre Curie in 1898 triggered a century of innovation and technological advancement in the use of ionizing radiation for diagnosis and treatment of human disease.

The use of x rays was not confined to imaging as the effects of photons on biological organisms and body cells were studied. The scientific community began to understand the adverse effects of x rays on cellular DNA and genetic material. The potential capability of x-ray beams in causing mitotic cell death at low doses or complete destruction of cells at higher doses was soon unveiled. The discovery of this property opened the doors to a new era of therapeutic and curative use of radiation beams.

Low energy x-ray beams produced by Coolidge type x-ray tubes were the first to be used for therapeutic purposes. The success rate was limited as a result of the high skin dose received by patients from the low energy x-ray beams. Hence, the

desire to achieve higher energies to improve beam penetration into tissue thereby producing better dose distributions within the body became the research focus of the scientific community. An important milestone was accomplished by the Canadian physicist Harold E. Johns and his invention of cobalt teletherapy unit in 1951 that enabled physicians to use megavoltage gamma rays for patient treatment. Over the next 30 years much higher energies were achieved by linear accelerators (linacs) and the myth of megavoltage treatment facilities became a reality.

During the past century, the x-ray imaging and radiation therapy have undergone significant development in parallel, yet essentially independently of one another. However, this has changed recently as the benefits of an integrated system has been re-evaluated. In oncology, the research has changed direction from achieving higher energy beams to accomplishing more conformal treatment plans accompanied by improvements in patient immobilization as well as target definition and localization.

The ultimate goal of radiotherapy is treatment of cancer with minimal damage to healthy tissues in order to minimize the probability of cancer recurrence, secondary cancers or other adverse radiation-related health effects. It has become evident that this goal can only be accomplished through the integration of imaging systems and therapy units. In fact, all the major developments in radiotherapy, such as 3D conformal radiotherapy, image guided radiotherapy (IGRT) and adaptive radiotherapy (ART) are intimately linked with advances in imaging.

In this thesis, a novel technique of imaging in radiotherapy will be introduced and discussed. The technique is based on the use of bremsstrahlung beams emitted orthogonally to the direction of a megavoltage electron beam striking the target.

1.2 Imaging and radiotherapy

Since the introduction of intensity modulated radiation therapy (IMRT) and the advancements made in the field of conformal radiotherapy, it has become possible to perform highly conformal radiotherapy treatments that contain very complex fields and sharp dose gradients[1]. However, although we possess the tools to deliver treatments of great complexities, the use of such conformal techniques is only beneficial if we have means to determine the exact position of the tumour at the time of treatment[2]. It is well known that a conformal plan with a tight planning target volume (PTV) and sharp gradient drop-offs is undesirable if the exact tumour position is not well known. This is because any slight miss-positioning of the patient (geographical miss) or any change in the location of the tumour may result in only partial treatment of the tumour and radiation damage to healthy tissues nearby. Hence, the ability to determine the exact position of the target volume immediately prior to each fractionated treatment is of utter importance, if the efforts toward conformal radiotherapy and sparing of normal tissues is to result in a successful treatment outcome[2,3].

Imaging prior to treatment serves the following three important purposes:

- Confirmation of tumour position with respect to computed tomography (CT), magnetic resonance (MR) or positron emission tomography (PET) images used at the time of treatment planning.

- Confirmation of proper machine operation.

- Monitoring of the size and shape of the tumour throughout the course of the fractionated treatment process.

1.3 Techniques of imaging in radiation therapy

In this section, several commonly used techniques of treatment verification imaging in radiation therapy including portal imaging, cone beam CT, tomotherapy, and ultrasound are reviewed.

Portal imaging is perhaps the most common type of imaging in radiotherapy. Most modern linear accelerators come equipped with this technology which consists of taking a two dimensional x-ray image using megavoltage therapy quality beam with a film or, more commonly, with the help of an electronic portal imaging device (EPID) as the detector.

The second technique is relatively new and referred to as *cone beam CT* (CBCT). Three dimensional CBCT images can be produced using kilovoltage (KV) or megavoltage (MV) beams. In the former case, an x-ray tube and a detector are attached to the linac gantry orthogonally. Hence, conventional x-ray quality images can be produced using this technique. In the case of the MV cone beam CT, the megavoltage energy therapy beam is used for imaging. The major difference between CBCT images and portal images lies in the fact that the former produces a reconstructed 3-dimensional (3-D) volumetric image of the patient, while the latter is simply a 2-D image of the patient's anatomy.

The use of *Tomotherapy*® as a means for both imaging and therapy has been expanding rapidly. Current tomotherapy units are composed of a 6 MeV linear accelerator mounted onto a CT-like gantry that enables the linac to rotate freely in a circular motion. Tomotherapy allows for three-dimensional megavoltage cone beam computed tomography (3D MV-CBCT) imaging while it is also used to deliver conformal helical treatments to patients. A 3D MVCT obtained with a tomotherapy machine is very similar to a 3D MV-CBCT taken using a conventional linac although the photon beam from a tomotherapy unit is only

divergent in one direction while the beam used to produce cone-beam CTs is inherently divergent in both directions.

The use of other imaging modalities and their combination with therapy units has expanded throughout recent years. The use of *ultrasound in radiotherapy* especially in treatment of prostate cancer has become a common practice[4,5]. The integration of magnetic resonance imaging (*MRI*) with conventional high energy linacs and cobalt units is still under research[6]. Finally, some facilities simply include a CT unit in the treatment room. In these facilities, the position of the treatment couch in the treatment room can be monitored and tumour localization, using CT prior to treatment, can be achieved through fixing the patients to the couch.

1.4 Shortcomings of current techniques

Each of the techniques described above has its own shortcomings that will be explained briefly in order to put the advantages and disadvantages of current techniques into perspective, thus giving the reader a better means to understand the strengths and weaknesses of the novel method of imaging that will be introduced in this work.

Although portal imaging is conceptually very simple, the major problem with current high energy portal images is their lack of contrast. Since megavoltage beams are used to produce these images, the images have contrast levels far below those produced with kilovoltage x rays[7] in diagnostic radiology. The physics behind this phenomenon is discussed in the next chapter.

Since MV-CBCT, like portal imagers uses megavoltage beams, it also lacks high soft tissue contrast. On the other hand, KV-CBCT units produce high contrast 3D images, but they are very bulky and heavy. Moreover, since the images are

produced by a kilovoltage unit that is completely separate from the treatment unit, care must also be taken to ensure that the position of the KV beam is strongly correlated with that of the MV beam.

Integrating other imaging modalities with radiotherapy often results in greater complexity of the units, increased price, as well as increased maintenance requirements. Although quite popular, use of ultrasound prior to treatment is not free of shortcomings, since the position of the ultrasound transducer needs to be accurately known and easily tracked in the treatment room. Another disadvantage of this technique is the large dependence of image quality on the skills of the technician performing the task. The images of an ultrasound not only suffer from a lower resolution compared to most diagnostic x-ray images, but may be different depending among other factors on the amount of pressure applied on the skin during the imaging procedure[4]. In addition, there are significant and unresolved differences between target volumes determined by ultrasound in comparison to those determined by CT or MR scanning.

1.5 Goal of the thesis

In this chapter an attempt was made to highlight the importance of imaging in radiotherapy. Various common techniques of image guided radiotherapy were discussed and their advantages and shortcomings were noted.

In this thesis, we introduce a novel technique of imaging in radiotherapy using the orthogonal component of bremsstrahlung beams. This work contains experimental results as well as Monte Carlo calculated data that were obtained to investigate the radiation quality of the orthogonal bremsstrahlung beams and to evaluate the feasibility of their use for imaging in radiation therapy. Using different techniques of beam-quality measurement, the quality of forward and orthogonal bremsstrahlung beams was determined and evaluated. Moreover,

simple contrast objects were imaged using radiographic films exposed to both the orthogonal and forward bremsstrahlung beams and the quality and contrast level of images obtained was evaluated.

The specific goals of this thesis are as follows:

- To provide a detailed description of the physics of bremsstrahlung beams, their production, and their dependence on various physical parameters.
- To introduce, explain, and justify several beam quality measurement techniques that were used in this work.
- To provide a description of the Monte Carlo codes and techniques used.
- To explain the properties and significance of both the experimental and Monte Carlo calculated results obtained.
- To promote the feasibility of this novel imaging technique and the advantages and disadvantages that it holds over other currently used techniques.

1.6 References

1 A. Gustafsson, B. K. Lind, and A. Brahme, "A generalized pencil beam algorithm for optimization of radiation therapy," Med. Phys. **21**, 343-356 (1994).

2 G. A. Ezzell, J. M. Galvin, D. Low, J. R. Palta, I. Rosen, M. B. Sharpe, P. Xia, Y. Xiao, L. Xing, and C. X. Yu, "Guidance document on delivery, treatment planning, and clinical implementation of IMRT: report of the IMRT Subcommittee of the AAPM Radiation Therapy Committee," Med. Phys. **30**, 2089-2115 (2003).

3 D. L. Van den Berge, M. D. Ridder, and G. A. Storme, "Imaging in radiotherapy," Eur. J. Radiol. **36**, 41-48 (2000).

4 K. M. Langen, J. Pouliot, C. Anezinos, M. Aubin, A. R. Gottschalk, I. C. Hsu, D. Lowther, Y. M. Liu, K. Shinohara, L. J. Verhey, V. Weinberg, and M. Roach, 3rd, "Evaluation of ultrasound-based prostate localization for image-guided radiotherapy," Int. J. Radiat. Oncol. Biol. Phys. **57**, 635-644 (2003).

5 J. Morr, T. DiPetrillo, J. S. Tsai, M. Engler, and D. E. Wazer, "Implementation and utility of a daily ultrasound-based localization system with intensity-modulated radiotherapy for prostate cancer," Int. J. Radit. Oncol. Biol. Phys. **53**, 1124-1129 (2002).

6 B. W. Raaymakers, A. J. Raaijmakers, A. N. Kotte, D. Jette, and J. J. Lagendijk, "Integrating a MRI scanner with a 6 MV radiotherapy accelerator: dose deposition in a transverse magnetic field," Phys. Med. Biol. **49**, 4109-4118 (2004).

7 T. S. Curry, J. E. Dowdey, R. C. Murry, and E. E. Christensen, Christensen's physics of diagnostic radiology, 4th ed (Lea & Fabiger, Philadelphia, PA, 1990).

Chapter 2

BREMSSTRAHLUNG BEAMS

2.1 Introduction

In this chapter the fundamental aspects of bremsstrahlung photon production and the various interactions of photons as well as electrons with matter are discussed first. The second portion of the chapter summarizes the work done over the past three decades on angular distribution of bremsstrahlung spectra as well as the dependence of photon yield on target material.

2.2 Charged particle interaction with matter

2.2.1 *Modes of interaction*

When a charged particle with a charge q_1 enters an absorber material, it undergoes Coulomb interactions with orbital electrons and nucleic protons of the absorber atoms. In scalar form, the Coulomb force F_{Coul} is given by

$$F_{Coul} = \frac{q_1 q_2}{4\pi\varepsilon_o r^2} \ . \qquad (2.1)$$

In Eq. (2.1) the parameters are as follows:

q	is the charge of the two interacting particles, distinguished by the subscript
r	is the separation distance between the two particles
ε_o	is the permittivity of vacuum (8.854×10^{-12} C/Vm)

Charged particle interactions are often categorized based on the magnitude of the Coulomb force between them. Since this force is strongly dependent on the separation distance between the orbital electrons and nuclei of the absorber atom and the travelling charged particle, one could also categorize the interactions based on the relative size of the classical impact parameter b and the atomic radius a, as shown in Fig. 2.1. Three possible interaction categories are listed below[1].

1. Simple interactions of a charged particle with an orbital electron where the impact parameter b is much greater than the atomic radius a ($b >> a$) are called *soft collisions.* Only a small amount of energy is transferred to the orbital electrons in these types of interactions.

2. Coulomb interactions of the passing charged particles with impact parameter b of the order of the atomic radius a ($b \approx a$) are called *hard collisions.* The energy loss per interaction is much greater in hard collisions than in soft collisions. However, in both instances the energy transfer to orbital electrons eventually results in heat production and slowing down or changing of the direction of the incoming particles. The electrons that gain sufficiently high kinetic energies through hard collisions to carry this energy a significant distance away from the track of the primary particle and produce their own ionizations of absorber atoms are often termed delta rays[2].

3. When a charged particle comes close to the nucleus of an absorber atom, i.e., the impact parameter b is much smaller than the atomic radius a ($b << a$), it may interact with the external nuclear Coulomb field. It is in this type of interaction that the charged particle is accelerated and some or all of its kinetic energy is released in the form of *bremsstrahlung* photons.

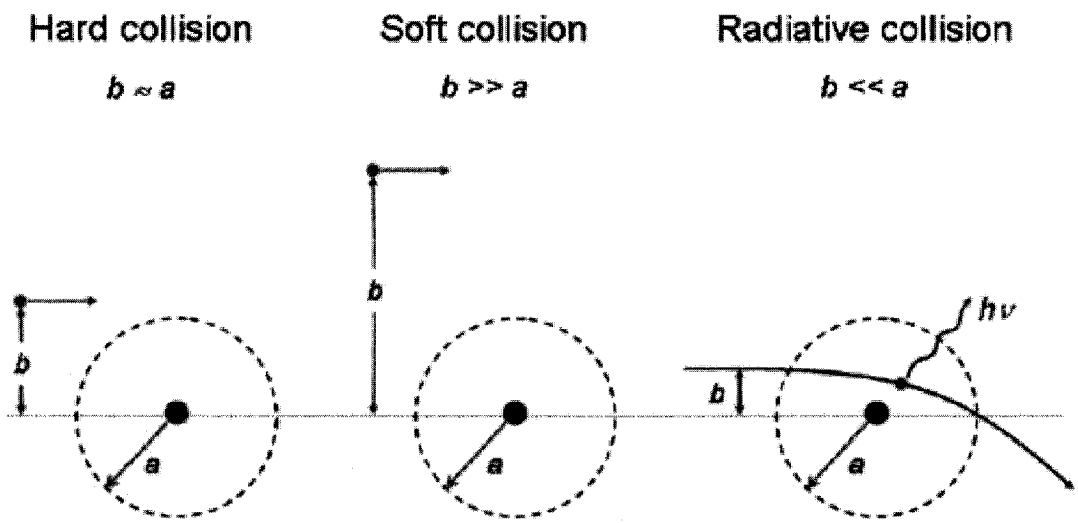

Figure 2.1: Three different interactions types of a charged particle with an atom. The categories have been established based on the relative size of the impact parameter b and atomic radius a (Ref. 1).

2.2.2 *Stopping power*

The rate of energy loss per unit length by a charged particle as it traverses a given absorber material is characterized by the material's linear stopping power S. Stopping power is a function of the charge, size and energy of the incoming particle as well as the properties of the absorbing medium. The charged particle-orbital electron interactions are categorized together and give rise to the linear collision (ionization) stopping power (S_{col}). The charged particle-nucleus interaction contributes to what is known as the linear radiative stopping power (S_{rad}).

Based on its definition, total stopping power can be expressed as the expectation value of the energy lost per unit length $\mathrm{d}\langle E\rangle$ of a charged particle in track dx,

$$S = \frac{\mathrm{d}\langle E\rangle}{\mathrm{d}x}. \tag{2.2}$$

The unit of the linear stopping power is MeV/cm. Through dividing the linear stopping power by the density of the absorbing medium the dependence of the stopping power on material type can be almost eliminated (a minor dependence on polarization correction δ remains[3]) and the mass stopping power is obtained. Writing the final product in terms of the two categories of stopping power, the general equation for the mass stopping power becomes

$$\frac{S}{\rho} = \frac{1}{\rho}\frac{\mathrm{d}\langle E\rangle}{\mathrm{d}x} = \frac{S_{col}}{\rho} + \frac{S_{rad}}{\rho}. \tag{2.3}$$

The energy spent in collision interactions results in local ionizations and excitations of the absorber atoms, contributing to the dose near the track. The radiative stopping power, on the other hand, describes the loss of energy in inelastic radiative collisions that is often carried away from the interaction site by the bremsstrahlung photons.

Collision stopping power

The collision stopping power can be further broken down into its two components: soft and hard interactions. A cut-off energy Δ is often used to define and separate the two events. The amount of energy lost in soft collisions ranges from a threshold energy to the cut-off energy, while the extent of energy lost in hard collisions ranges from the cut-off energy to a maximum E_{max}. This maximum equals the energy of the charged particle if the two particles are of equal mass and distinguishable (e.g., an electron and a positron interaction), or half the initial maximum energy of the incident particle if the interaction happens between two indistinguishable particles (e.g., two electrons interacting). It may be that the charged particle traversing the matter has a much greater mass compared to the orbital electrons of the medium. In such cases, the maximum energy transfer from the charged particle to the orbital electron E_{max} is equal to $2m_e v_\infty^2$, where m_e is the mass of the orbital electron and v_∞ is the velocity of the heavy charged particle prior to the interaction.

Radiative stopping power

The rate of bremsstrahlung production by charged particles traveling through medium is described by the mass radiative stopping power. In this section we focus on electrons and positrons as the only charged particles capable of bremsstrahlung photon production (i.e., having a non-zero radiative stopping power). In the following section this estimation is discussed further and its validity justified. The mass radiative stopping power can be calculated at any point by taking into account three contributing factors, including the total cross section for bremsstrahlung production σ_{rad}, the initial total energy E with which the particle enters the desired slab of the medium, and the number of atoms per unit mass N_a with $N_a = N_A/A$ where N_A is the Avogadro number and A is the atomic mass

number of the target. Of course, the total particle energy can be written in terms of its rest mass energy and its kinetic energy: $E = m_e c^2 + E_k$. Equation (2.4) describes the mass radiative stopping power,

$$\frac{S_{rad}(E)}{\rho} = N_a . \sigma_{rad}(E) . E . \qquad (2.4)$$

The cross section σ_{rad} may be described classically, relativistically, or quantum mechanically depending on the kinetic energy of the incident particle and the degree of accuracy required. By substituting in the equations representing various terms of the above formula and collecting all the constant terms together under a constant k, we obtain

$$\frac{S_{rad}(E)}{\rho} = k \frac{Z^2}{A} \left(E_K + m_e c^2\right) \langle B_r \rangle , \qquad (2.5)$$

where $\langle B_r \rangle$ is a slowly varying function of the atomic number of the absorbing material as well as the incident particle's total energy. $\langle B_r \rangle$ has a value of 16/3 for light charged particles in the non-relativistic energy ranges and its value approaches 15 for particle kinetic energies of 100 MeV [1]. A simple analysis of Eq. (2.5) shows that the mass radiative stopping power increases with absorbing material's atomic number (by estimating Z/A to have a constant value of 0.5), and the incident charged particle's kinetic energy. Figure 2.2 shows a graph of mass radiative and collision stopping power for three different materials.

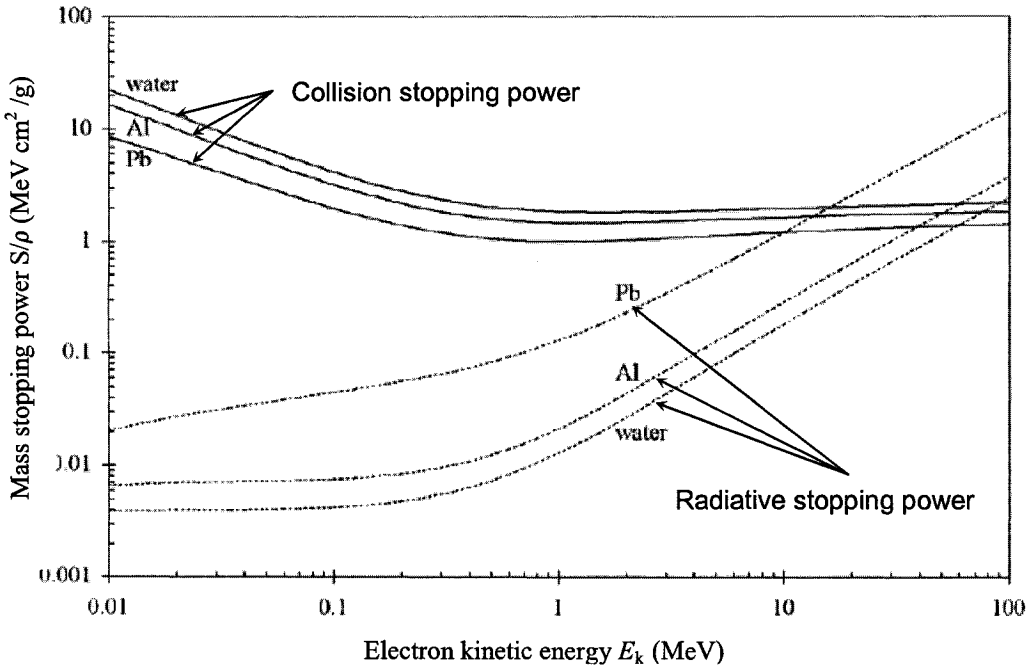

Figure 2.2: Mass collision and radiative stopping powers for three different materials: water, aluminum and lead (Ref. 2).

The bremsstrahlung photon yield $B(E_K)$ is defined as the percentage of the kinetic energy of the incident electron beam that goes into bremsstrahlung photon production. Hence, this quantity is calculated by normalizing the portion of the energy of the light charged particle that is spent in inelastic radiative collisions to the total amount of energy lost by the particle in the absorbing medium (for thick targets, of course the total energy loss is equal to the total initial kinetic energy of the particle)

$$B(E_K) = \frac{\int_0^{E_K} \frac{S_{rad}(E)}{S_{tot}(E)} dE}{\int_0^{E_K} \frac{S_{tot}(E)}{S_{tot}(E)} dE} = \frac{1}{E_K} \int_0^{E_K} \frac{S_{rad}(E)}{S_{tot}(E)} dE . \qquad (2.6)$$

2.2.3 *Intensity distribution of bremsstrahlung photon production*

The energy flow of the bremsstrahlung radiation per unit area or the intensity of emitted radiation is given by the Poynting vector $\vec{S}$

$$\vec{S} = \vec{E} \times \vec{B} / \mu_o \,, \tag{2.7}$$

where $\vec{E}$ and $\vec{B}$ are the electric and magnetic fields, respectively, associated with the accelerated charged particle. By substituting the electric and magnetic fields with respective terms describing each, one obtains

$$\left|\vec{S}(r,\theta)\right| = \frac{1}{16\pi\varepsilon_o}\frac{q^2a^2}{c^3}\frac{\sin^2\theta}{r^2}\,, \tag{2.8}$$

where

q is the charge of the accelerating particle

a is the acceleration of the particle

θ is the angle of bremsstrahlung photon emission between the accelerating charged particle's direction of travel and the radius vector connecting the position of particle in space to the point of interest

ε_o is the permittivity of vacuum

c is the speed of light in vacuum

r is the separation distance between the accelerating charged particle and the point of interest in space

It is important to note from Eq. (2.8) that the emitted radiation intensity goes as the square of incident particle's charge and acceleration.

Since often the charged particles we are concerned with are relativistic, the classical formula obtained above does not apply, and under relativistic conditions, the emitted radiation intensity becomes

$$\left|\vec{S}(r,\theta)\right| = \frac{1}{16\pi\varepsilon_o}\frac{q^2a^2}{c^3r^2}\frac{\sin^2\theta}{(1-\beta\cos\theta)^5}, \tag{2.9}$$

where $\beta = v/c$ is the charged particle's velocity normalized to the speed of light in vacuum. Equations (2.8) and (2.9) describe the total energies of a charged particle that go into bremsstrahlung photon production per unit area, per unit time in both classical and relativistic energy regimes, respectively. By integrating this energy flux over the surface area of a sphere, one obtains the power *P* emitted by the accelerated charged particle in the form of bremsstrahlung radiation as follows:

$$P = \frac{dE}{dt} = \int\left|\vec{S}\right|dA = \frac{1}{6\pi\varepsilon_o}\frac{q^2a^2}{c^3}. \tag{2.10}$$

Equation (2.10) is commonly known as the classical Larmor relationship and shows that anytime a particle of charge *q* is accelerated or decelerated, it emits part of its kinetic energy in the form of bremsstrahlung photons [1].

Now considering the fact that interactions between charged particles are governed by Coulomb forces and equating the general equation describing these forces (Eq. 2.1) to the basic classical Newtonian definition of force, we obtain

$$ma = \frac{q_1q_2}{4\pi\varepsilon_o r^2}, \tag{2.11}$$

from where it follows that

$$a \propto \frac{q_1 q_2}{m}, \tag{2.12}$$

suggesting that acceleration of a charged particle is inversely proportional to its mass. Hence, the acceleration that a heavy charged particle undergoes, while traversing an absorber, is much smaller than that of electrons or positrons. Equation (2.10) shows that the power emitted by charged particles in the form of bremsstrahlung is dependent on the square of the acceleration. It can thus be deduced that, in contrast to light charged particles, heavy charged particles do not contribute appreciably to bremsstrahlung photon production. This explains why in the previous section we ignored the contribution of heavy charged particles to bremsstrahlung photon production in comparison to that of light charged particles.

2.2.4 *Angle of maximum intensity*

By taking the derivative of $|\langle S \rangle|$ with respect to angle θ and setting the equation equal to zero, one can find the value of θ for which the function is maximized, i.e., the angle of maximum radiation intensity emission. Hence,

$$\left.\frac{\mathrm{d}|\langle S \rangle|}{\mathrm{d}\theta}\right|_{\theta=\theta_{\max}} = 0 \tag{2.13}$$

from where it follows that

$$\theta_{\max} = \arccos\left\{\frac{1}{3\beta}\left(\sqrt{1+15\beta^2}-1\right)\right\}, \tag{2.14}$$

where β is the charged particle's velocity normalized to the speed of light in vacuum. In the limit, as $\beta \to 0$, $\theta_{max} \to 90°$, while as $\beta \to 1$, $\theta_{max} \to 0°$. It can then be generalized that, as the energy of the charged particles striking an absorbing material increases, the radiation intensity becomes more and more forward peaked. Of course, this is not to say that all photons are produced in the forward direction, for there remains a finite probability for a photon to be produced at any given angle.

Figure 2.3 shows a polar diagram of the intensity distribution of the bremsstrahlung photon production for electrons of various energies incident on an absorber material. The figure was obtained by plotting the proportionality $\left|\langle S(r,\theta)\rangle\right| \propto \sin^2(\theta)/(1-\beta\cos\theta)^5$ from Eq. (2.9) for various β values, and θ_{max} was obtained using Eq. (2.14). Note that for electrons of low kinetic energy E_K, θ_{max} is close to 90°, while for higher energy electrons, the photons are preferentially emitted in the forward direction. Moreover, note that the size of the lobes is a direct estimation of the intensity of bremsstrahlung photon production. At higher incident electron energies, the relative intensity of bremsstrahlung production is higher, as described by the Larmor relationship.

If an electron beam with a certain energy spectrum is incident on a target, then the resulting intensity distribution plot is obtained through a superposition of the intensity distribution plots for each of the constituent charged particle energies. One such result is shown in Fig. 2.4. The shape of the bremsstrahlung radiation intensity distribution is directly related to the incident electron beam's energy spectrum: The higher the mean energy of the electron spectrum striking the target material, the more forward-peaked is the resulting bremsstrahlung distribution.

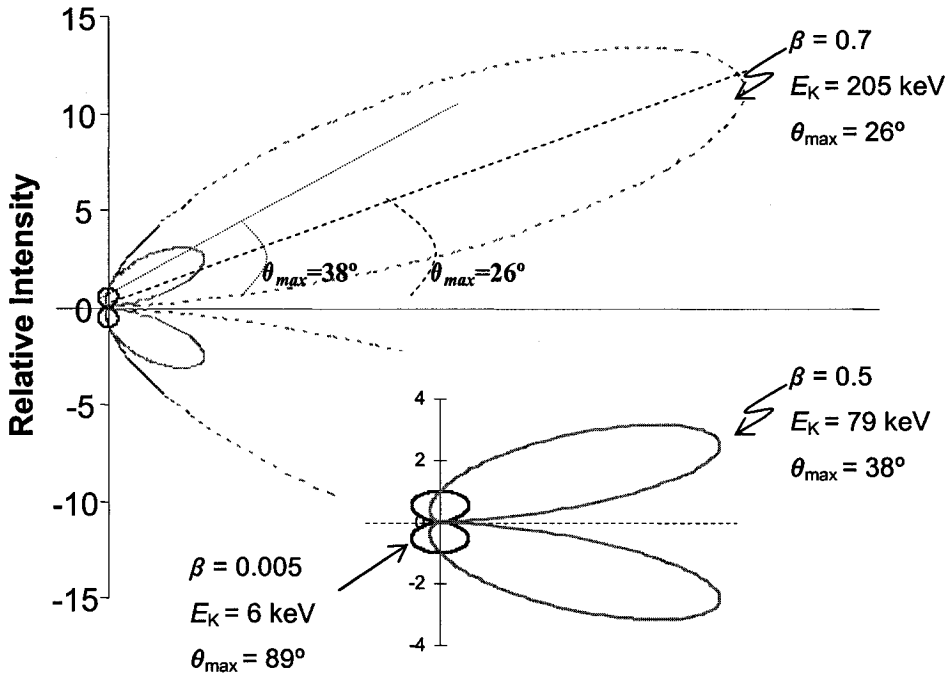

Figure 2.3: Radiation intensity distributions for three accelerated electrons of different kinetic energies E_K. For each case, the electron's speed β, kinetic energy E_K, and the angle of maximum bremsstrahlung intensity distribution θ_{max} have been noted.

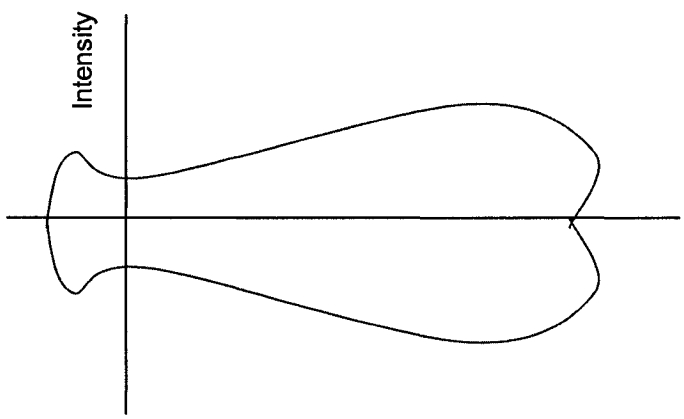

Figure 2.4: A schematic diagram of a possible bremsstrahlung radiation intensity distribution map for a high energy electron beam of a given energy spectrum.

2.3 Photon interactions with matter

Whether created through a bremsstrahlung interaction, a nuclear decay or an annihilation event, photons also interact with matter as they travel through medium. Many modes of photon interaction with matter are known, most notably: photoelectric effect; Rayleigh scattering; Compton scattering; pair production; triplet production; and photonuclear reaction. In this section we focus briefly on three of these interactions that are most relevant to our discussion. Figure 2.5 shows the mass attenuation coefficient for lead. This graph serves as an example to illustrate the dominant effect of photoelectric interaction at low photon energies, the dominance of Compton effect at intermediate energies, and the dominance of the pair production event in the megavoltage energy range.

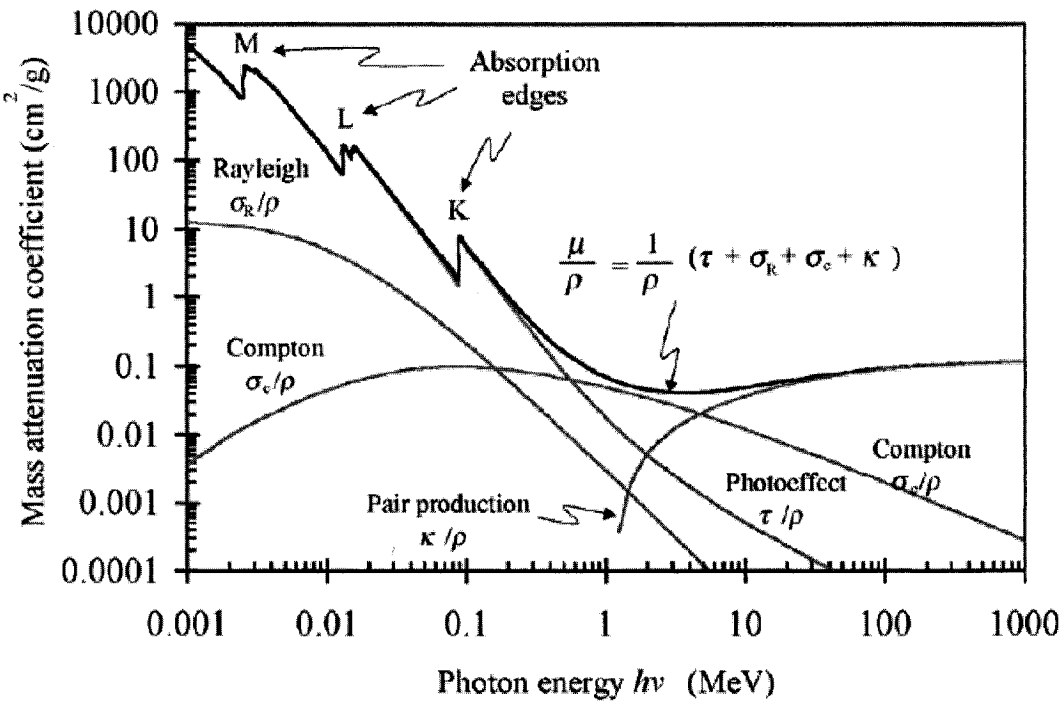

Figure 2.5: The total mass attenuation coefficient μ/ρ for lead, as well as the four most important mass coefficients that constitute the total coefficient (Ref. 1).

2.3.1 *Compton effect*

Figure 2.6 schematically shows an incoherent or Compton scattering event of a photon of energy $h\nu$ with an electron. Depending on the initial energy of the incident photon, the assumption of the electron being free and stationary may or may not be accurate. As the photon energy drops to values of the order of E_B (binding energy of the electron), the approximation of a free electron breaks down. Throughout this work, however, we are concerned with photon energies that are generally much higher than E_B. After an interaction, the energies of the scattered photon $h\nu'$ and recoil electron E_K are given, respectively, by

$$h\nu' = h\nu \frac{1}{1+\varepsilon(1-\cos\theta)} \tag{2.15}$$

and

$$E_K = h\nu \frac{\varepsilon(1-\cos\theta)}{1+\varepsilon(1-\cos\theta)}, \tag{2.16}$$

where $\varepsilon = h\nu / m_e c^2$, and θ is the angle of photon scatter, as shown in Fig. 2.6. Furthermore, Eq. (2.17) describes the relationship between the angles of photon scatter and electron recoil, as defined in Fig. 2.6

$$\cot\phi = (1+\varepsilon)\tan\left(\frac{\theta}{2}\right). \tag{2.17}$$

Since the Compton effect represents an interaction of a photon with a free electron, the attenuation coefficient per electron ${}_e\sigma^c$ and the mass attenuation coefficient σ_m^c are independent of the attenuator's atomic number Z, while the atomic coefficient ${}_a\sigma^c$ depends linearly on Z.

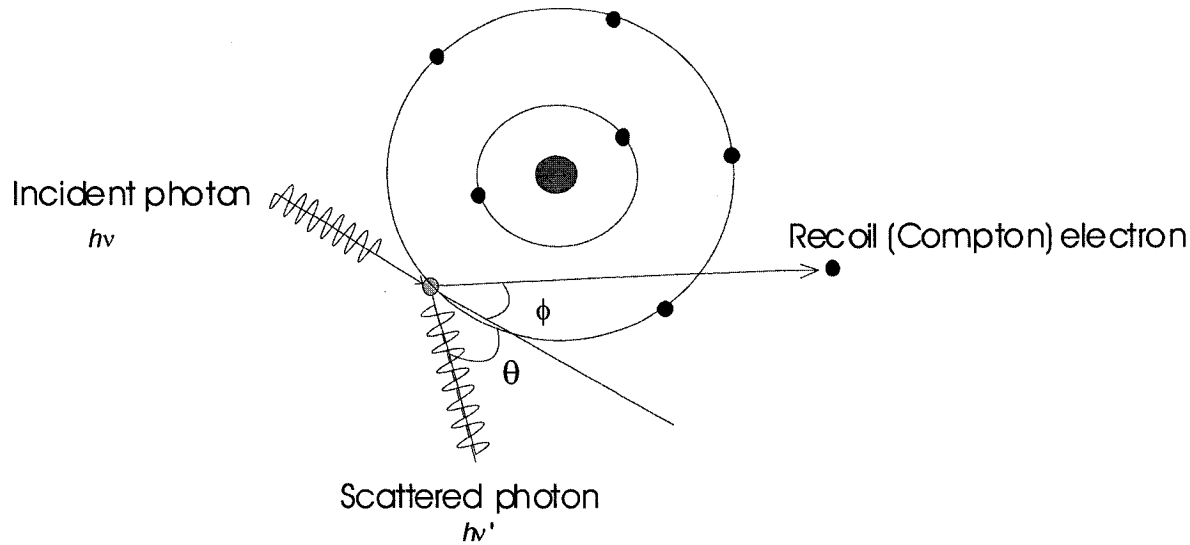

Figure 2.6: A schematic diagram of a Compton interaction between a photon of energy *hv* and a "free and stationary" orbital electron.

In the event of a Compton interaction, Eq. (2.15) shows that, as the energy of the incident photon beam is increased, a higher percentage of the beam's energy is transferred to the scattered photons. Moreover, the scattered photons have a higher probability of being emitted at smaller angles, i.e., they are forward-peaked as well.

As shown in Fig. 2.6, a vacancy is created in the atomic shell of the absorber atom as a result of the Compton interaction. An atom with a vacancy in its inner shell is highly excited and returns to its ground state through one or more electronic transitions from higher atomic shells to lower ones. The energy difference between binding energies of the shells involved in the transition is emitted either radiatively in the form of characteristic (fluorescent) radiation or non-radiatively in the form of Auger electrons [1].

Since the energy transitions in atoms occur between shells and sub-shells of known and discrete energy levels, the energy difference emitted as a result of a transition is characteristic of the atom, hence, the term characteristic radiation. Figure 2.7 displays the probability of characteristic radiation emission, i.e.,

fluorescent yield, as a function of the atomic number of the excited atom. The probability of characteristic photon production as a result of a transition of electrons from higher shells to fill a K-shell vacancy is determined by ω_K. Similarly, ω_L refers to the fluorescent yield for a transition occurring to fill an L-shell vacancy. As previously mentioned, the energy difference between transitions may also be emitted from an atom through the ejection of an electron from higher shells, termed an Auger electron, carrying away the excess energy less the binding energy of the Auger electron itself. The probability of an Auger electron emission is given by unity minus the probability of the fluorescence production.

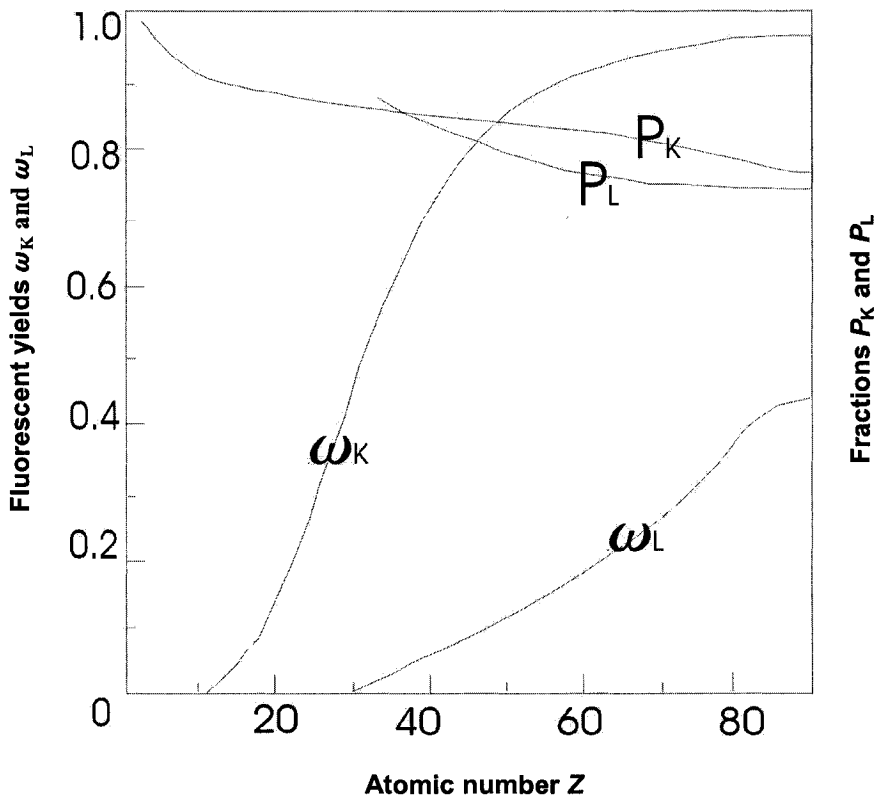

Figure 2.7: Fluorescence yield for vacancies of the K-shell ω_K, and L-shell ω_L as a function of atomic number Z. The fractions P_K and P_L have also been shown for $hv > E_{B,K}$ and ($E_{B,L} < hv < E_{B,K}$), respectively (Ref. 1)

2.3.2 *Pair production*

At photon energies above $2m_ec^2$, the conversion of energy to matter and production of an electron-positron pair becomes energetically possible. As shown in Fig. 2.8, after interacting with the strong electric field of the nucleus, a photon of energy $h\nu$ greater than 1.022 MeV may be completely absorbed through the mechanism of pair production. Through this process, an electron-positron pair is produced. Due to conservation of energy, 1.022 MeV of the energy of the incident photon goes into the production of this pair, while any remaining energy of the photon is divided in any possible combination between the two particles. Of course, due to conservation of momentum, some energy is also transferred to the nucleus; however, because of the relatively large mass of the nucleus, this energy is so small that it can be neglected.

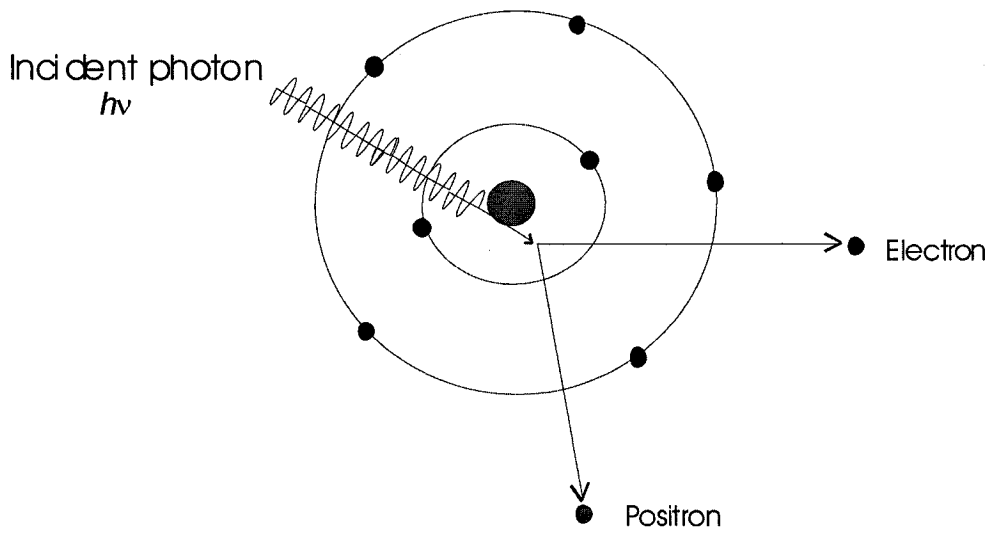

Figure 2.8: A schematic diagram of pair production. A photon of energy $h\nu$ greater than two electron rest masses is capable of interacting with the nuclear electric field of an atom to produce an electron/positron pair.

The positron produced in the process travels through matter while exciting and ionizing atoms. Once the positron is brought to rest, it will combine with a free electron forming a positronium; a temporary state in the decay of positron where the positron is bound to an electron. Following the annihilation, two photons, each of energy 0.511 MeV are ejected in opposite directions fulfilling the conservations of energy, momentum, and charge. Lastly, it should be noted that the mass attenuation coefficient of pair production is proportional to the atomic number of absorbing material.

2.3.3 *Photoelectric effect*

At kilovoltage photon energies, photoelectric interaction has the highest cross-section. It is the interaction between a photon and a tightly bound orbital electron of the atoms of the absorber material. In the process, the photon is completely absorbed, while the orbital electron is ejected with a kinetic energy $E_K = h\nu - E_B$, where E_B is the binding energy of the orbital electron. The curve P_k, shown in Fig. 2.7, describes the probability of creating a vacancy in the K-shell of the absorber's atom by a photon of energy higher than the binding energy of the K-shell. The curve P_L in turn displays the probability of creating a vacancy in the L-shell by a photon of energy greater than the L-shell binding energy and lower than the K-shell binding energy of the absorber's atom. The vacancy in the inner shells of the excited atom is subsequently filled by a series of electronic transitions and the difference in energy after a transition is emitted by the production of either a characteristic photon or an Auger electron as described in Section 2.3.1. It is important to note that the photoelectric atomic cross section is strongly dependent on the atomic number of the absorbing material. This dependence can be anywhere from Z^4 at relatively low photon energies to Z^5 at high photon energies.

2.3.4 *Beam hardening and beam softening effects*

As a photon beam of a particular energy penetrates a target material, some of the photons interact with the target in one of the modes listed in Section 2.3 at a rate proportional to the probability of the given interaction, as specified by their individual attenuation cross-sections. Hence, through the simple attenuation formula $N = N_0 e^{-\mu x}$, one could describe the number of photons interacting through a certain mode, as the beam penetrates a given thickness *x*.

For a heterogeneous x-ray beam of maximum energy lower than roughly 10 MeV travelling through a medium, the low energy component of the beam gets attenuated more strongly than higher energy ones, mainly because of the photo-electric cross-section (Fig. 2.5). Hence the beam becomes richer in high-energy photons, becoming more penetrating or "harder."

On the other hand, a heterogeneous beam of very high energy traversing a material becomes less penetrating or "softer." This happens, since the higher energy components of the beam are attenuated at a larger extent compared to the low energy ones, primarily due to the pair production events.

Of course, a mono-energetic beam becomes neither softer nor harder, as it traverses matter, since the beam, rather than having contributing photons of various energies being attenuated at different rates, contains only photons of equal energy.

2.4 Influence of target on beam quality

The influence of target material and thickness on the spectrum of the resulting bremsstrahlung photon beam and its yield has been a topic of interest for more than three decades.

This determining effect of the target material in clinical linacs was first investigated by Podgorsak et al. in 1974 when they noticed that a betatron and a high energy linac, when operated at the same nominal energies, produced markedly different x-ray spectra [4]. The results were investigated and differences in target material as well as flattening filter material were determined to be the main cause [4].

Through the next few sections, we will review the angular distribution of bremsstrahlung photon energy spectrum and its yield as a function of target material and thickness as well as the energy of the incident electrons. Of course, emphasis will be placed upon the orthogonal direction which is of interest to the content of this paper.

2.4.1 *Beam constituents*

When an electron beam strikes a target, photons are produced in all directions. The energy spectrum obtained at any given angle is composed of primary (non-scattered) bremsstrahlung photons produced and emitted in that angle, as well as scattered photons. For megavoltage incident electrons, the relative yield of primary bremsstrahlung photons to the yield of scattered photons drops significantly with angular deviation away from the forward direction[5]. Faddegon et al.[5] observed that the percentage of scattered photons to total bremsstrahlung yield is very small in the forward direction and changes slightly with target's atomic number. At larger angles, however, the relative contribution of primary photons drops significantly and this drop is strongly dependent on the target material. In the orthogonal direction for a 15 MeV incident electron beam, the scatter contribution may be anywhere between roughly 33% for high atomic number targets to almost 85% for low atomic number targets[5], as shown in Table 2.1.

θ	Be (11.67 g/cm^2)	Al (9.74 g/cm^2)	Pb (9.13 g/cm^2)
	%	%	%
1°	2±1	3±2	4±4
10°	9±2	11±2	10±1
60°	72±9	54±6	38±1
90°	85±11	73±11	33±3

Table 2.1- Yield of scattered photons from the target relative to the integrated bremsstrahlung yield. Results are from Monte Carlo simulations (Ref. 5). The target thicknesses are noted in g/cm^2.

One potential reason for the significant contribution of scattered photons to the total number of photons emitted from the target in the orthogonal direction relative to the forward direction can be described by considering Eq. (2.14). For megavoltage electrons incident on an absorbing material, bremsstrahlung photons are preferentially produced in the forward direction with much reduced intensity at larger angles. Hence, the percentage contribution of scattered photons to the integral photon yield is lowest in the forward direction and increases with increasing angular deviation due to the small yield of primary bremsstrahlung photons at larger angles.

Moreover, the yield of scattered photons relative to the integrated bremsstrahlung yield is largely dependent on the atomic number of the absorbing material at large angles (Table 2.1). One could reason that in higher Z materials, travelling electrons are more prone to being scattered. In these materials, it takes fewer collisions for the electron to change direction and travel at angles other than forward. Of course, these electrons can subsequently undergo bremsstrahlung interactions and result in primary bremsstrahlung photons that propagate with angles larger than 0°. This explains why in Table 2.1, for a given angle, the scattered photon contribution to the beam make up is much smaller for larger Z materials.

A general overview of various components of a photon beam is presented in this section to help understand the different characteristics of the bremsstrahlung beams that are discussed in subsequent chapters. In practice, however, there is little benefit in distinguishing the various components of a beam and in fact this task is often impossible to carry out experimentally.

2.4.2 *Angular distribution of the photon energy spectrum*

The angular distribution of the mean energy of a photon spectrum has also been studied in several papers[5,6,7,8]. It has been shown that for megavoltage electrons striking a given target material, the mean energy of the bremsstrahlung spectrum decreases significantly as a function of angle[4,5].

Moreover, for any given incident electron energy, the mean energy of the resulting bremsstrahlung spectrum is larger for higher atomic number targets than for lower atomic number ones past an angle of 10°. This difference becomes more pronounced at larger angles[4,5]. For angles below 10°, the situation is generally reversed with lower atomic number targets producing slightly higher energy spectra[4,5]. Hence, it can be surmised and experimentally determined that for incident megavoltage electrons, there will be a faster drop in the mean energy of the bremsstrahlung spectrum as a function of angle for lower atomic number materials. Both Fig. 2.9 and Table 2.2 show these results.

The reason for greater mean energy of spectra produced by high Z targets at large angles could be attributed to the fact that initial incident electrons in higher Z materials have to undergo fewer collisions before being scattered[6]. Therefore, the primary scattered electrons lose a smaller percentage of their energy. Of course, these higher energy scattered electrons eventually result in more energetic x-ray beams at angles other than forward.

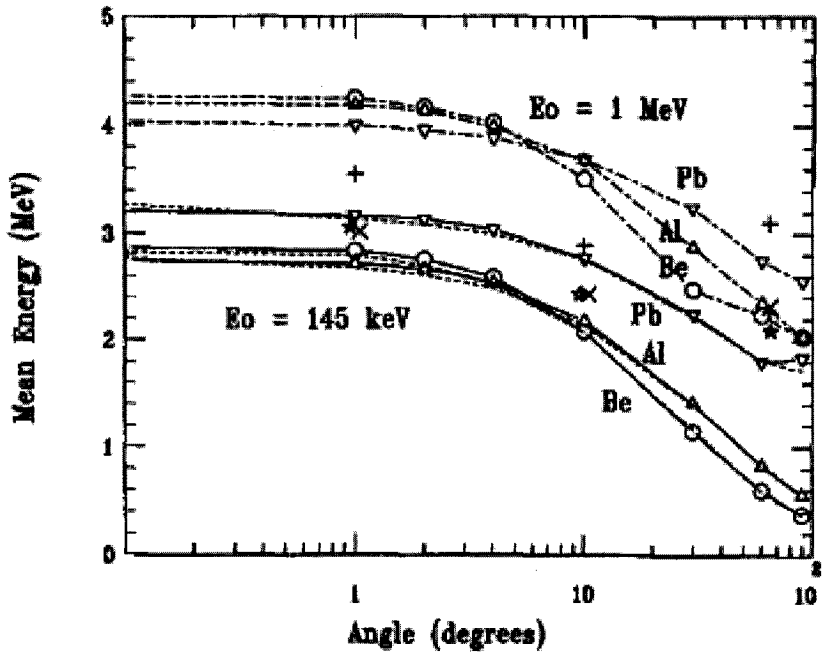

Figure 2.9: The angular distribution of mean energies of 15 MV bremsstrahlung spectra for energies above 145 keV (solid lines) and 1 MeV (broken lines) for beryllium, aluminum and lead. The curves display MC calculated results. Experimental results for angles of 1°, 10° and 60° only have also been shown (*-Be, x-Al, +-Pb) (Ref. 5)

Angle / Target	0°	5°	10°	20°	30°	45°
Aluminum	4.1	3.8	3.1	2.2	1.7	1.3
Lead	3.5	3.4	3.0	2.6	2.3	2.0

Table 2.1: Depths of dose maxima (in cm) as a function of angle for a 25 MeV electron beam striking targets of aluminum and lead (Ref. 4).

In addition, as mentioned in the previous section, with an increase in angular distribution, the contribution of lower energy scattered photons to the whole beam make-up increases. This angularly dependent increase in contribution of low energy scattered photons may also be part of the reason for an angularly dependent decrease of mean energy away from the forward direction.

The above described trends can be clearly observed through the work of Faddegon et al.[5] on angular distribution of bremsstrahlung spectra where their measurements and Monte Carlo (MC) results match with relatively good agreement (to within 2%) at energies above 140 keV for lower Z material and 400 keV for lead target. The researchers' spectral measurement results for beryllium and lead targets are displayed in Fig. 2.10.

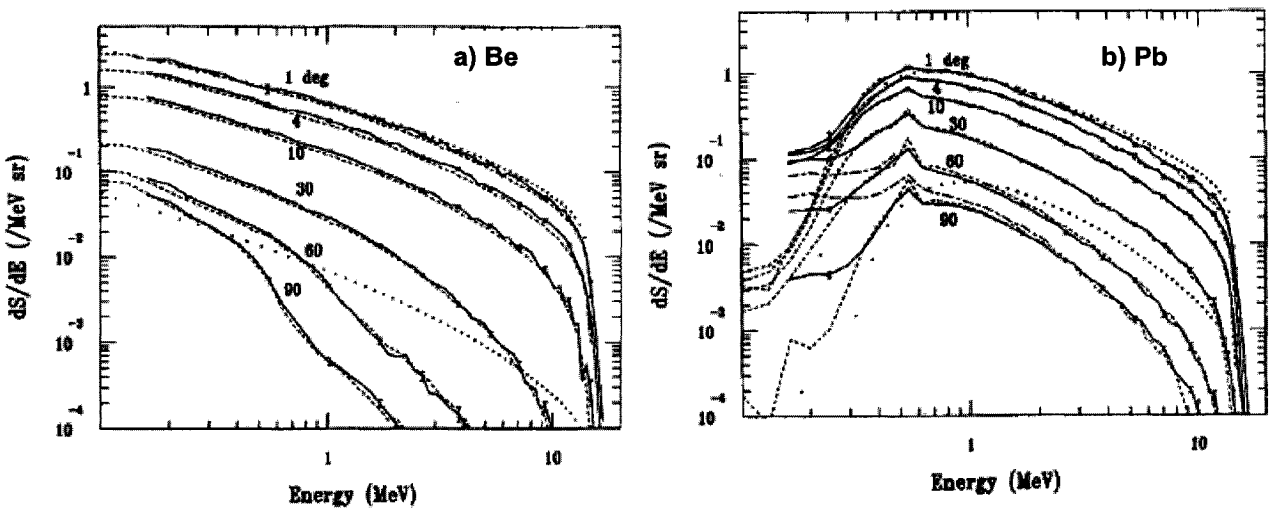

Figure 2.10: The bremsstrahlung generated at angles of 1°, 4°, 10°, 30°, 60°, 90° by 15 MeV electrons incident on a) 11.67 g/cm^2 thick, 6.72 g/cm^2 radius beryllium target and b) 9.13 g/cm^2 thick, 17.95 g/cm^2 radius lead target. The measured photon yields (solid lines) are compared to the calculated bremsstrahlung yields (dashed lines). The calculations were done using the EGS4 Monte Carlo code. Results are absolute (photons per electron). The results at 0° and 2° are left off of the graphs for clarity although they are similar to that of 1° (Ref. 5).

Figure 2.11 shows the experimental results of the energy fluence from two different targets, as obtained by Podgorsak et al[4]. The dashed curves show the energy fluence per incident 25 MeV electron as a function of angle. The results show that lower atomic number targets produce slightly higher energy fluences in the forward direction, while the situation is reversed for larger angles, as discussed previously. The total x-ray energy emitted by the targets is calculated by integrating the energy fluence from an angle of 0° to a given angle θ. The figure shows that the integral x-ray energy emitted into a solid angle defined by the angle θ is dependent on the atomic number Z of the target and it is higher for targets of higher Z (solid curves). Over small angular deviations from the forward direction, the difference between targets of high and low Z is small. This difference grows for larger angles.

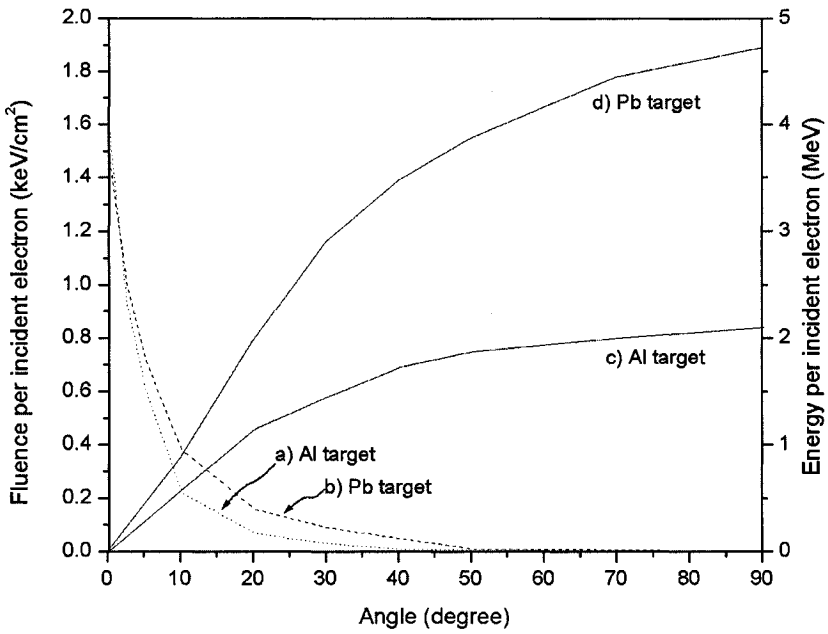

Figure 2.11: The dashed curves represent the energy fluence (dE/dA), per incident 25 MeV electron as a function of the angle θ from the central axis a) for an aluminum target and b) for a lead target. The solid curves represent the integral of the fluence, $\int_0^{2\pi}\int_0^{\theta}(dE/dA)r^2 \sin\theta d\theta d\phi$, over the surface of a sphere with radius r, equal to the target-phantom surface distance of 125 cm (Ref. 4).

2.4.3 *Angular distribution of photon fluence*

Podgorsak et al. [4] and Faddegon et al. [5] performed a thorough study of angular dependence of photon fluence or yield. Both groups found that in the forward direction, the integral bremsstrahlung yield is essentially independent of the target material[9]. However, they also showed that with an increase in angle, the total x-ray yield becomes strongly dependent on the atomic number of the target material and is higher for higher Z targets. At 10°, the bremsstrahlung yield from a beryllium target is two times lower than the yield from a lead target, while this difference increases to 5 times in the orthogonal direction[5].

The above results can be explained by noting that in a higher Z material, on the average, the electrons are deflected at larger angles than in a lower Z material. These deviated electrons subsequently produce x rays in directions other than the forward direction, resulting in a greater photon yield at larger angles for larger atomic number targets.

Equation (2.6) was used to describe the integral bremsstrahlung yield (i.e., total photon yield produced by a target in all directions). From this equation and Eq. (2.5), it can be seen that the total integral photon yield is proportional to the atomic number Z of the target material. Since both high and low atomic number targets essentially have the same rate of photon production in the forward direction, it is only reasonable that the bremsstrahlung yield for higher Z targets at larger angles is greater than that of lower Z targets[4].

Figure 2.12 shows the measured angular distribution of the integrated bremsstrahlung yield for 15 MeV electrons incident on various targets. The angular behaviour of the photon yield can easily be recognized from the figure.

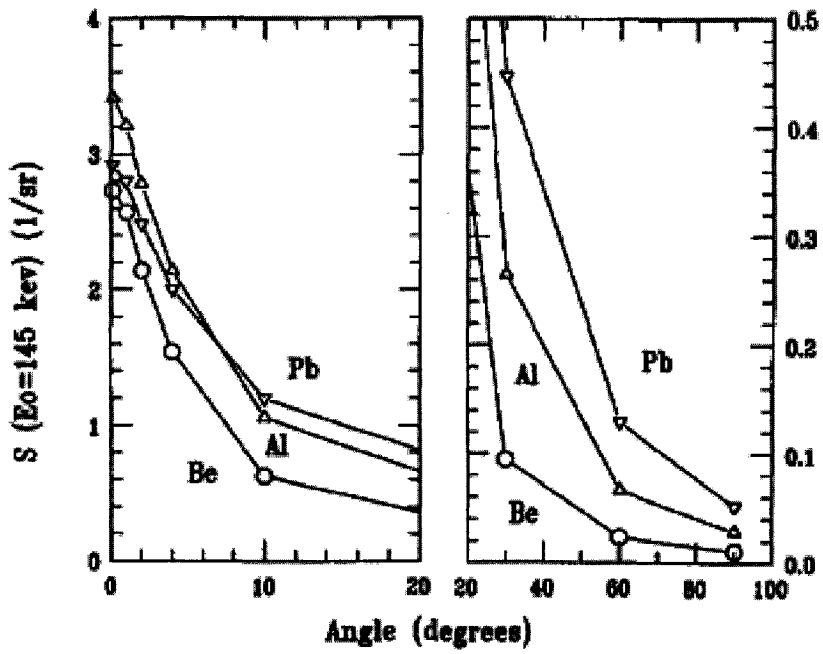

Figure 2.12: Measured angular distributions of the integrated bremsstrahlung yield of 15 MeV electrons incident on 11.67 g/cm^2 thick beryllium, 9.74 g/cm^2 thick aluminum and 9.13 g/cm^2 thick lead targets (Ref. 5).

2.4.4 *Influence of charged particle contamination and target thickness*

Charged particle contamination is defined as any charged particles emerging from the target along with bremsstrahlung photons. Since almost all charged particle contamination is often due to electrons, we will here only consider electron contamination. Target thickness in a given direction, on the other hand, is defined as the thickness of absorbing material present in between the centre of the incident beam and the exiting edge of the target. Figure 2.13 schematically shows the target thicknesses *d'* and *d*, respectively, in the forward direction and in the orthogonal direction.

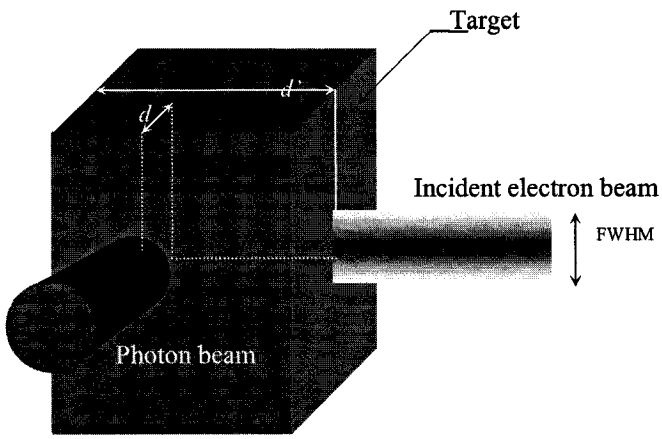

Figure 2.13: A schematic diagram of an incident electron beam with a given *f*ull *w*idth at *h*alf *m*aximum (FWHM) striking a target. Only the orthogonal component of the bremsstrahlung beam is shown for clarity.

Target thickness directly affects the contribution of contaminating electrons. A target of thickness less than the CSDA (continuous slowing down approximation) range of the incident electrons R_{csda} in the direction of interest often results in many contaminating electrons produced and observed in that direction. Figure 2.14 displays the measured percentage depth doses (PDDs) in the forward direction for targets of various thicknesses. The relatively high surface dose for small target thicknesses is due to the deposition of energy by low energy contaminating electrons near the surface of the phantom material[6]. For target thicknesses greater than the CSDA range of the primary incident electrons, the surface dose is at acceptable ranges since the majority of the primary incident electrons and the secondary electrons are attenuated and absorbed in the larger thickness of target material[10].

The effects of electron contamination can be negligible or significant depending on the experiment being performed and the extent of the contamination. In general, electron contamination results in significant uncertainties for dose measurements, while it causes little error when performing fluence measurements[8]; the reason being that electrons escaping the target deposit

much more energy at the surface than a high-energy photon, yet they both contribute equally to the fluence measurements[8].

Lastly, it should be noted that thin targets produce higher energy beams than thick targets for the same given incident electron energy and target material[8]. For thicknesses smaller than R_{csda}, an increase in thickness relates to an increased number of hard collision interactions that the primary incident electrons undergo. Hence, although the bremsstrahlung yield from a thick target is higher than the yield from a thin target (simply due to greater probability of inelastic bremsstrahlung interaction in the larger thickness), the effective energy of the beam is lower, since many of the electrons resulting in the x-ray production have lower energies[3,11].

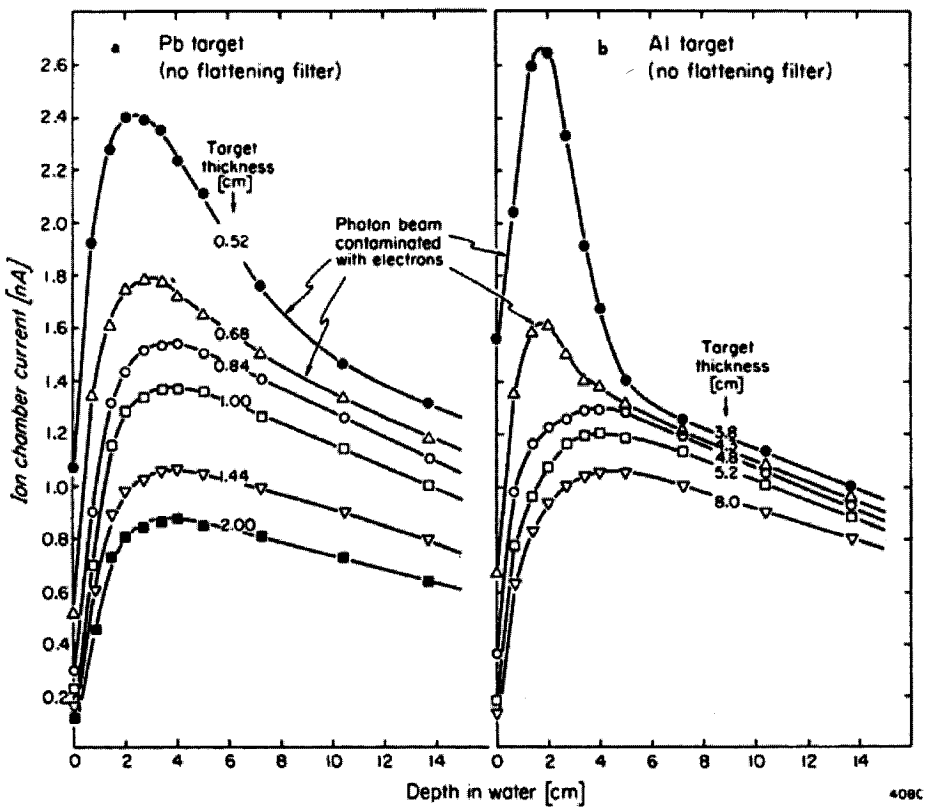

Figure 2.14: Ionization chamber current versus depth in water for unflattened x-ray beams produced by 25 MeV electrons striking targets of various thicknesses of lead (a) and aluminum (b). Circular field of 10 cm diameter at an SSD of 100 cm (Ref. 6).

For target thicknesses greater than R_{csda}, the electron contamination is negligible. Any further increase in target thickness beyond R_{csda} results in a change in photon beam's energy spectrum. From mass attenuation graphs, such as Fig. 2.5, one could predict the effect of the extra thickness of the target material on the energy of the beam depending on the beam's initial spectrum. For photons of megavoltage energy above 5 MeV, an increased thickness results in softening of the beam, whereas in the case of kilovoltage beams, it results in beam hardening.

2.5 References

1 E. B. Podgorsak, Radiation physics for medical physicists (Springer, New York, NY, 2005).

2 International Atomic Energy Agency (IAEA), Radiation oncology physics : a handbook for teachers and students. E. B. Podgoršak (International Atomic Energy Agency, Vienna, Austria, 2005).

3 F. H. Attix, Introduction to radiological physics and radiation dosimetry (Wiley, New York, NY, 1986).

4 E. B. Podgorsak, J. A. Rawlinson, M. I. Glavinovic, and H. E. Johns, "Design of X-ray targets for high energy linear accelerators in radiotherapy," Am. J. Roentgenol. Radium Ther. Nucl. Med. **121**, 873-882 (1974).

5 B. A. Faddegon, C. K. Ross, and D. W. Rogers, "Angular distribution of bremsstrahlung from 15-MeV electrons incident on thick targets of Be, Al, and Pb," Med. Phys. **18**, 727-739 (1991).

6 E. B. Podgorsak, J. A. Rawlinson, and H. E. Johns, "X-ray depth doses from linear accelerators in the energy range from 10 to 32 MeV," Am. J. Roentgenol. Radium Ther. Nucl. Med. **123**, 182-191 (1975).

7 R. Mohan, C. Chui, and L. Lidofsky, "Energy and angular distributions of photons from medical linear accelerators," Med. Phys. **12**, 592-597 (1985).

8 B. Nordell and A. Brahme, "Angular distribution and yield from bremsstrahlung targets," Phys. Med. Biol. **29**, 797-810 (1983).

9 B. A. Faddegon, C. K. Ross, and D. W. Rogers, "Forward-directed bremsstrahlung of 10- to 30-MeV electrons incident on thick targets of Al and Pb," Med. Phys. **17**, 773-785 (1990).

10 J. A. Rawlinson and H. E. Johns, "Percentage depth dose for high energy x-ray beams in radiotherapy," Am. J. Roentgenol. Radium Ther. Nucl. Med. **118**, 919-922 (1973).

11 H. E. Johns and J. R. Cunningham, The physics of radiology, 4th ed (Charles C. Thomas, Springfield, IL, 1983).

Chapter 3

BEAM QUALITY MEASUREMENTS

3.1 Introduction

The ultimate and most complete way of analyzing an x-ray beam is through measuring its energy spectrum. This consists of measuring the relative fluence of photons of every energy between zero and the kinetic energy of the electrons striking the target. Such measurements are often challenging as well as time consuming, and require expensive and very accurate instrumentation. Moreover, it is often difficult to compare the penetrability and/or energy of two beams by simply looking at their respective spectra.

For this reason, beam quality specifiers have been formulated that can be quickly and accurately measured with common, relatively inexpensive ionization chambers. These beam quality measurements can be used directly as a means to provide information regarding the penetrability and energy of x-ray beams.

In this chapter, the beam quality measurement factors used in this work are discussed. They are: percentage depth dose, attenuation and half-value layer, effective and mean energy, as well as image contrast measurements using diagnostic films.

3.2 Percentage depth dose

Percentage depth dose (PDD) for a given radiation beam in a given material, such as water or tissue, is defined as the ratio, expressed as a percentage, of absorbed dose at any depth z to the absorbed dose at a reference depth z_{ref} along the central axis of the beam. The reference depth z_{ref} is taken as the depth of the maximum dose z_{max}, as shown in Fig. 3.1.

$$PDD(z, A_{surface}, f, hv) = \frac{D(z, A_{surface}, f, hv)}{D(z_{ref}, A_{surface}, f, hv)} 100 = \frac{D_z}{D_{z_{ref}}} 100 . \qquad (3.1)$$

Taking $z_{ref} = z_{max}$, we get

$$PDD(z, A_{surface}, f, hv) = \frac{D_z}{D_{z_{max}}} 100 . \qquad (3.2)$$

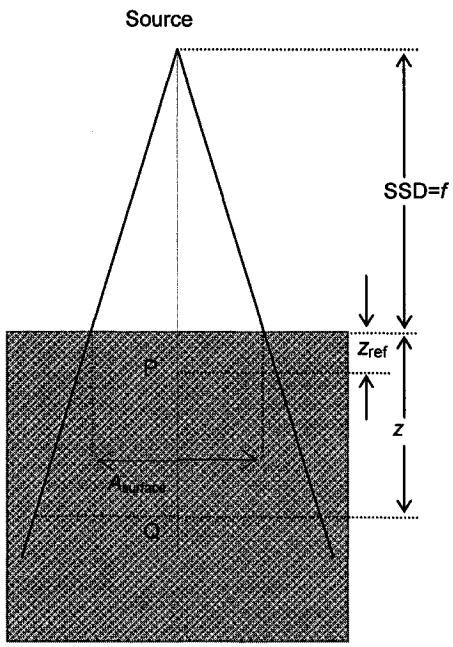

Figure 3.1: A schematic diagram showing a point source and a phantom material where P is a point at the depth of maximum dose and Q is an arbitrary point at depth z in the phantom. Both points P and Q are on the beam central axis.

As shown in Eq. (3.2), PDD is dependent on the field size on the surface of the phantom, $A_{surface}$, as well as the distance f between the source of radiation and the surface of the phantom material, SSD, in addition to the depth z inside the material and the photon beam energy hv.

For x-rays generated at potentials up to 400 kVp, the depth of dose maximum occurs essentially on the surface of the phantom due to the limited range of the secondary electrons along the beam direction (less than 0.4 mm). On the other hand, for a "clean" photon beam, i.e., a beam without any charged particle contamination, of energy greater than 400 kVp, the depth of dose maximum z_{max} occurs at some depth below the phantom surface[1]; The higher is the photon energy, the larger is z_{max}.

In the context of the PDD and absorbed dose, the concept of kerma, an acronym for the "kinetic energy released in matter," needs to be discussed as well. The transfer of energy from a photon beam to the medium involves the photon interacting with the atoms of the medium and transferring some or all of its energy to set electron(s) into motion. However, the transfer of energy from the photons to the electrons (kerma) does not occur at the same location as the absorption of the energy by the medium (absorbed dose) does[2]. The implications of the above statement will be briefly discussed here.

Kerma can be written as a function of the photon fluence by Eq. (3.3), where μ/ρ is the mass attenuation coefficient for the medium; $\langle E_{tr} \rangle$ is the average amount of energy transferred to charged particles released in the medium at each site of interaction, and ϕ is the photon fluence of the beam

$$K = \phi \cdot \left(\frac{\mu}{\rho} \right) \cdot \langle E_{tr} \rangle . \qquad (3.3)$$

There is no way, however, of expressing absorbed dose in terms of photon fluence unless a state of equilibrium between kerma and absorbed dose is reached. Figure 3.2 is used to describe the relationship between the two quantities for a high energy photon beam. When a "clean" photon beam enters a medium, the photons start interacting with the material setting charged particles (electrons and positrons) into motion. Often, for high energy beams, these electrons are also of high energy and travel preferentially in the forward direction as they deposit their energy by ionizing the atoms along their path. Since absorbed dose is proportional to the number of ionizations, it increases initially in a region termed build-up.

As photons travel through the medium more and more electrons are set into motion, increasing the number of ionizations, while, on the other hand, photon attenuation results in a reduction in the total number of photons available for energy transfer. These two opposing effects give rise to a point of equilibrium, where the number of electrons entering a given volume equals the number of electrons leaving it, thus producing a condition termed "charged particle equilibrium". This point of equilibrium corresponds to a maximum in the absorbed dose. At this point, in fact, absorbed dose equals the collision kerma, i.e., the total kerma less the energy carried away by bremsstrahlung photons.

In reality, past this equilibrium point, photon attenuation becomes the dominant factor resulting in a gradual decrease in the kerma and absorbed dose. Since the absorbed dose at any point beyond the peak is due to the kerma further upstream, the absorbed dose curve is always above the collision kerma curve[2]. The region past the depth of maximum dose is referred to as the region of the "transient charged particle equilibrium" (TCP).

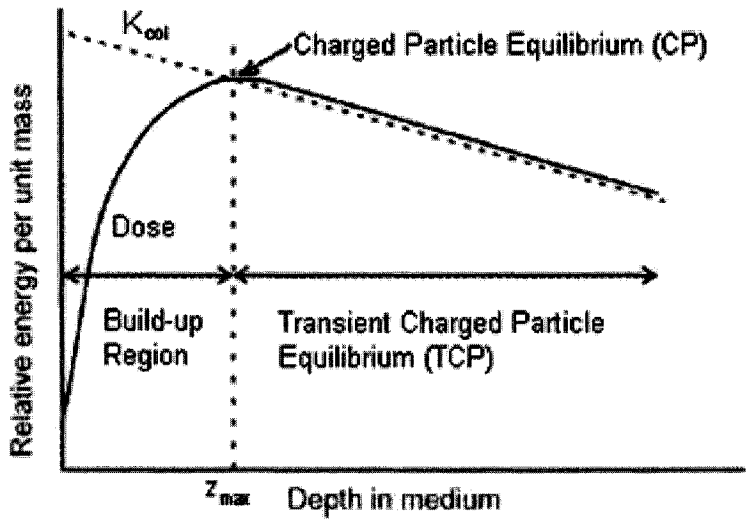

Figure 3.2: A generic graph showing the behaviour of absorbed dose and collision kerma (K_{col}) as a function of depth in medium for a megavoltage beam. The 'build-up' and 'transient charged particle equilibrium' regions as well as the point of charged particle equilibrium have also been labelled (Ref. 2).

If in Fig. 3.2 the peak absorbed dose is normalized to 100%, the PDD of the photon beam can be retrieved. In the presence of a photon beam with charged particle contamination, however, the surface dose is greater than the expected values and z_{max} occurs closer to the surface[3].

For a theoretical narrow "clean" photon beam, the behaviour of absorbed dose can easily be described by taking into account the attenuation of the beam, as it penetrates the medium, and the drop in fluence that is described by the inverse square law, as the distance from the source increases. Given D_{max}, the dose at depth of maximum dose, the primary component (excluding scatter contribution) of the dose at depth z D_z^{pri} can be described by

$$D_z^{pri} = D_{max} e^{-\mu(z-z_{max})} \left(\frac{f + z_{max}}{f + z} \right)^2, \qquad (3.4)$$

where the exponential describes the attenuation of the beam and the term in the bracket represents the inverse square law.

3.3 Half-value layer

For a photon beam, the half-value layer (HVL) is defined as the thickness of a given material that results in reduction of the air-kerma rate in air to half of its original value. Although very powerful, HVL must be measured under the so-called "good geometry" conditions in order to minimize the effects of scattered radiation and improve the reliability and reproducibility of this beam quality specifier. The "good geometry" conditions are defined as follows[4]:

1. Narrow beam geometry. Perhaps the most important condition that needs to be met is the presence of a narrow (small diameter) non-diverging beam. If the beam has a large diameter, then the scatter radiation from the attenuator may in fact reach the measuring device and contribute to the reading which in turn results in an HVL measurement that is larger than the actual expected value. Often collimators are used, if the beam is not narrow.

2. Appropriate distance between the attenuator and the measuring detector. No matter how fine the diameter of the beam, scatter radiation from the attenuator is inevitable. It is thus important to ensure that a large enough distance is maintained between the attenuator and the measuring device to minimize the amount of scatter radiation that reaches the detector.

3. Ionization chamber. Theoretically, the air kerma of a point source should be measured at a point with and without the attenuator. However, in reality, even if a point source is achieved, finding the kerma at a single point is almost impossible. Small ionization chambers, often of Farmer type, are used for this purpose. Care must be taken to ensure a chamber wall of air-equivalent material to minimize the perturbations caused by the walls.

Often, in addition to the first HVL (HVL_1), the second HVL (HVL_2) is also measured allowing for a better beam quality description. The HVL_2 is defined as the thickness of material used to reduce the air-kerma rate in air from one half down to one quarter of its original value. The ratio of the first HVL to the second HVL is often referred to as the homogeneity coefficient of the photon beam and is sometimes used as well to characterize a photon beam.

It has already been discussed in Chapter 2 that the photoelectric effect is the dominant mode of interaction in the low energy region, while Compton and pair production interactions become important at higher megavoltage energies. Since the mass attenuation coefficient of the photoelectric effect is highly Z-dependent, small thicknesses of attenuating material can have a dramatic influence on the attenuation of the beam. This is not the case in megavoltage energy ranges where the Compton mass attenuation coefficient is independent of Z and pair production mass attenuation coefficient varies linearly with Z. Hence, attenuation measurements or HVL measurements often prove to be insensitive beam quality specifiers for high energy beams, since they vary little for beams of differing energies. Of course, at large energies, large thicknesses of attenuator material need to be placed in front of the beam. This may further prove challenging or impractical.

3.4 Effective energy

The effective energy, also known as the equivalent energy of a heterogeneous photon beam $h\nu_{eq}$, may be calculated from the HVL measurements and is often used to describe the quality of a heterogeneous radiation beam. The effective energy of a heterogeneous photon beam is defined as the energy of a mono-energetic beam that has the same HVL_1 as the heterogeneous beam. Figure 3.3

shows the relationship between HVL_1 and effective energy for various attenuator materials.

3.5 Mean energy

Although less commonly used, the mean energy of a heterogeneous photon beam may also be used to describe the qualities of the beam. Mean energy is simply an average of the weighted sum of the energy bins of a given beam spectrum. From this definition, one could imagine two markedly different beam spectra that have the same mean energy. Hence, mean energy should be used in conjunction with other beam quality specifiers, if a thorough understanding of the quality of the beam is required.

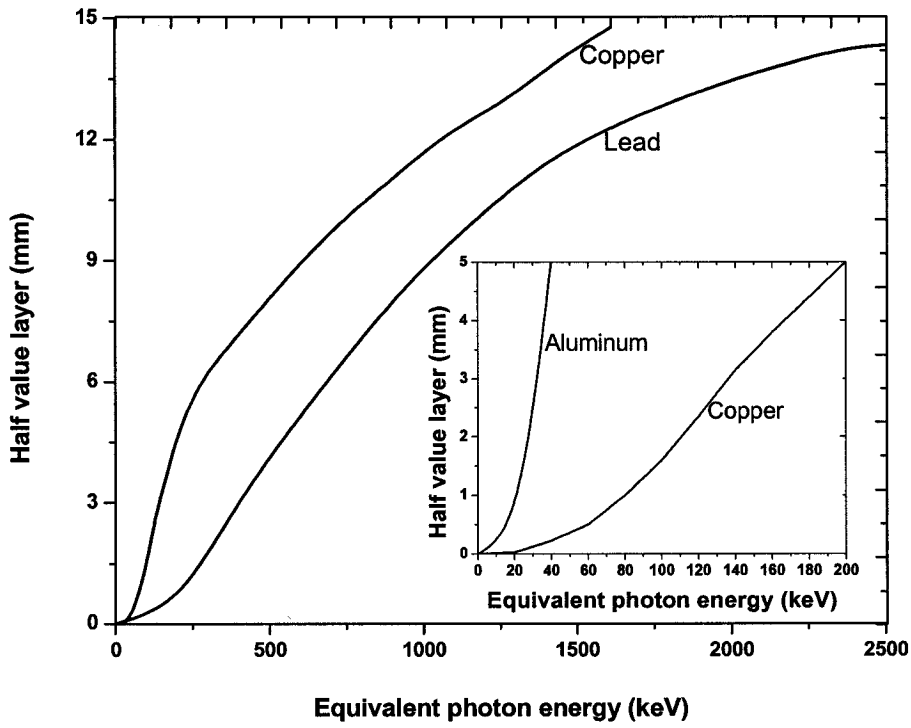

Figure 3.3: The relation between the half-value layer (HVL) and the equivalent photon energy $h\nu_{eq}$ for three absorbing materials: aluminum, copper and lead (Ref. 2).

3.6 Film

Film dosimetry has become a common practice in clinics and it may be used also for beam quality measurements. Since one of the techniques used in this work involved observation of image contrast levels of radiographic film, a brief description of film dosimetry and an explanation of image contrast is provided in this section.

A radiographic film consists of a transparent film base coated with an emulsion containing very small crystals of silver iodobromide (Fig. 3.4). When exposed to light or radiation, a chemical change takes place within the exposed crystals to form what is referred to as a latent image. Once developed, the affected crystals are reduced to small grains of metallic silver. The film is then fixed and any unaffected granules are removed by the fixing solution, leaving a clear film in their place. The metallic silver is not affected by the fixer and causes the darkening of the film. In diagnostic imaging, normally the film is sandwiched between two fluorescent screens that help increase the number of photons incident on the film, decreasing the dose to the patient, while increasing the contrast. Therapy quality films are not normally used in conjunction with screens, however.

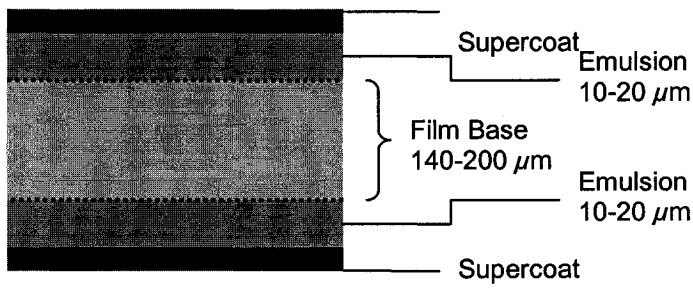

Figure 3.4: A schematic diagram of a radiographic film. The emulsion contains microscopic crystals of silver iodobromide protected by a coating on one side and backed by a film base on the other (Ref. 5). Fluorescent screens are not shown in this figure.

Although films can be used directly to measure contrast levels based on differences in intensity and two dimensional dose distributions can be obtained in this fashion, the limitations of films must also be understood.

A characteristic curve displays the relation between the optical density of a film and the log of the exposure. Figure 3.5 shows the characteristic curve for a typical x-ray film. The flat regions to the extreme left and right show an exposure independent optical density for the film (see Eq. (3.6)). The flat region to the lower left (region 1) is due to the density of the film base plus background fog. The linear portion of the graph at high exposures (region 4) is due to the chemical reaction of all available silver bromide reactants[6]. In this region the film does not turn darker with increased exposure, since no further chemical reactions can take place once all the reactants are consumed. It is best if a radiographic film is used for exposures that fall in the region characterised by the constant increase of the slope (region between 2 and 3) [7]. It is only then that a direct constant relationship between dose and optical density can be drawn[6].

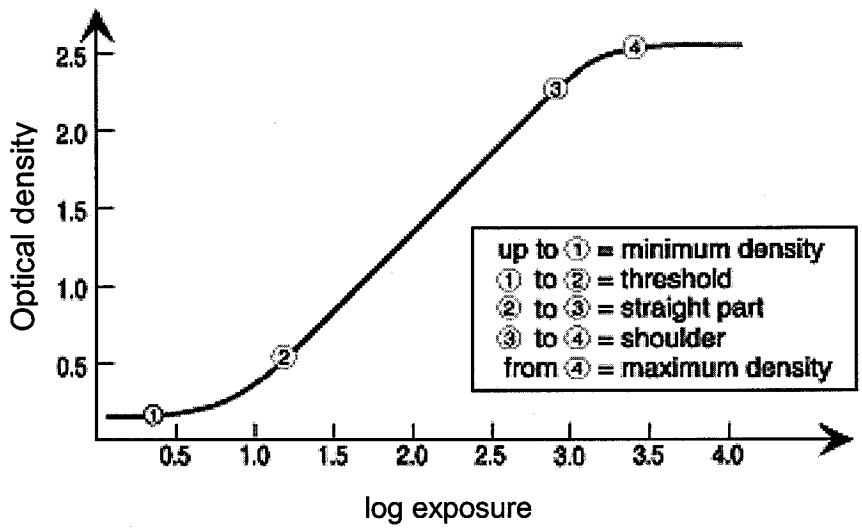

Figure 3.5: A typical characteristic density curve for a radiological film. The figure shows optical density of the film as a function of the log of the exposure (Ref. 7).

To fully describe the quality of an image, three characteristics are often used: contrast, resolution, and noise level.

Contrast *C* refers to differences in the level of brightness of parts of the image that correspond to anatomically or physiologically different parts of the body[5]. Thus, the contrast can be defined as the difference in brightness (intensity or fluence rate) between the object and background region, taken relative to the background level[5].

However, an equivalent, yet more commonly used technique, is to define radiographic image contrast *C* between two adjacent regions in a film as the difference in their optical densities *OD*:

$$C = OD_{obj} - OD_{bac} \,, \tag{3.5}$$

where the optical density *OD* is defined as,

$$OD = -\log\left(\frac{I_t}{I_o}\right) = \log\left(\frac{I_o}{I_t}\right) \,, \tag{3.6}$$

with I_o the intensity of the scanning light incident on the film and I_t the intensity of the transmitted beam emerging through the film[5].

Substituting Eq. (3.6) into Eq. (3.5), the following general equation for the contrast is obtained,

$$C = OD_{bac} - OD_{obj} = \log\left(\frac{I_o}{I_{bac}}\right) - \log\left(\frac{I_o}{I_{obj}}\right) = \log\left(\frac{I_{obj}}{I_{bac}}\right). \tag{3.7}$$

A perfectly transparent film has an *OD* of 0 and a film with an *OD* of 1 transmits 10% of the incident light . Moreover, a contrast value of zero simply means that there is no difference in the optical densities of the regions of interest.

Resolution of a system is a measure of the system's proficiency at revealing fine details[7]. The resolution is as much dependent on the quality of the imaging system, as it is on the quality of the image receptor. The resolution may be described as the minimum distance between two objects whose images can just barely be distinguished from one another[5]. Different test objects can be used clinically to test the resolution of a system. One such test object contains thin lead strips separated at different intervals. By imaging the object, a quantitative indication of the resolution in terms of the number of line pairs distinguishable per millimetre can be obtained.

Although the level of **noise** in an image is an important concept in and of itself, we will not discuss it in any detail, since that quality indicator is not addressed in our work. There are various sources of noise including quantum mottle (quantum fluctuations in the number of photons reaching the detector) and spatial variation in thickness and size of grains as well as the concentration of grains in a given area.

3.7 References

1 F. H. Attix, Introduction to radiological physics and radiation dosimetry (Wiley, New York, NY, 1986).

2 H. E. Johns and J. R. Cunningham, The physics of radiology, 4th ed (Charles C. Thomas, Springfield, IL, 1983).

3 C. C. Ling and P. J. Biggs, "Improving the buildup and depth-dose characteristics of high energy photon beams by using electron filters," Med. Phys. **6**, 296-301 (1979).

4 E. B. Podgorsak, Radiation physics for medical physicists (Springer, New York, NY, 2005).

5 A. B. Wolbarst, Physics of radiology (Medical Physics Pub., Madison, WI, 2000).

6 F. M. Khan, The physics of radiation therapy, 2nd ed (Williams & Wilkins, Baltimore, MD, 1994).

7 T. S. Curry, J. E. Dowdey, R. C. Murry, and E. E. Christensen, Christensen's physics of diagnostic radiology, 4th ed (Lea & Fabiger, Philadelphia, PA, 1990).

Chapter 4

THE MONTE CARLO METHOD

4.1 Introduction

The power of science lies in its ability to describe natural phenomena in a consistent and reproducible manner. In physics, like any other branch of science, the ability to predict a physical phenomenon is of great importance, because not only it enables one to anticipate the outcome of an event, it also demonstrates that one's understanding of the event is accurate. However, in many real life situations, formulating an analytical model to describe a phenomenon is difficult if not impossible. This is where Monte Carlo (MC) techniques become useful. In the context of radiation therapy and radiation transport, MC techniques are those which simulate and "track" the random trajectories of individual particles by using computer-generated pseudo-random numbers to sample from the probability distribution functions governing the physical processes involved[1].

Hence, the MC technique is conceptually simple, for it initially involves only the choice of a radiation source and simulation of the irradiation geometry. Subsequently, individual particles are tracked in the medium, while a random number generator is constantly used to sample the probability distribution (cross-section) of various potential interaction types in the medium. If an interaction is selected by the computer, the particle is transported to the location of the

interaction and then, based on another set of random numbers and probability distributions, the new direction and energy of the particle are determined. If other particles are formed in the particular interaction, they will be put on a stack and will be transported as well. If a large number of initial particles is simulated in such a way, information about average values of macroscopic quantities, such as energy deposition, can be obtained[1].

Electron transport in Monte Carlo simulations can be very time-consuming, since every electron can undergo a large number of elastic scatterings with nuclei of the absorber. Moreover, during their slowing down process, electrons can set other orbital electrons ("knock-ons" or delta rays) into motion leaving many atoms in an excited state. For this reason, the Monte Carlo technique uses the so-called "condensed-history," in which the particle is transported in finite steps instead of a continuous path and the effects of all interactions that may occur between two steps are grouped together and applied at the end of each step[2].

Monte Carlo codes can be divided into two broad categories called class I and class II by Berger[2]. The classification is based on the method used by a code to treat the bremsstrahlung photons and knock-on electrons. In class I models, the assumption is made that the energy and direction of the primary electrons are not affected by the creation of secondary particles and bremsstrahlung photons. Class II models use the same assumption as class I models only for energies below a certain threshold. However, in class II models the influence of secondary particles and bremsstrahlung photons on the primary electron is taken into account for primary electron energies larger than the specified threshold. Class II algorithms are, in principle, more accurate than class I codes, although the difference between the two becomes significant only in particular cases[3,4].

For our work specifically, there were a number of justifications to use the Monte Carlo technique. First, our experimental results and Monte Carlo simulation findings were compared. Possible differences encouraged us to determine the

cause of the discrepancy and often resulted in modification either in the experimental setup or in various parameters of the code, both of which helped us to understand the experiment better. Once we ensured that consistent results could be obtained reproducibly using both techniques, an extended number of simulations was run without the need to perform the experiments. Many of these simulations were experimentally difficult to reproduce and time-consuming to perform.

In this chapter the various codes used in this work are discussed. No details of the actual codes are given, however, the basic knowledge to reproduce our simulations is provided.

4.2 The EGSnrcMP code

Currently, for the purposes of electron transport, most Monte Carlo codes available are based on one of two widely used approaches, one based on the ETRAN (*e*lectron *tran*sport) developed by Berger and Seltzer[5] at the National Bureau of Standards now National Institute of Standard and Technology (NIST), and the other on EGS (*e*lectron-*g*amma-*s*hower) code developed by Ford and Nelson[6] at the Stanford Linear Accelerator Centre (SLAC).

In our work, the EGSnrcMP code, the newest version of the EGSnrc system[7], was used. Written in Fortran, the EGS algorithms are those belonging to class II. A brief comparison between the EGS system and the ETRAN is given below.

The major difference between the two codes is not so much the difference in class types but in the overall system design. The EGS system[6] is much more flexible than is the ETRAN[5], because it is a package of subroutines simulating the electron and photon transport[3]. This greater flexibility, however, comes at a cost for a need of greater familiarity of the user with the actual details of the

code[8]. On the other hand, the ETRAN system can be treated as a 'black-box,' because it requires very little knowledge of the details of the code.

Although the EGS is a class II algorithm, the ETRAN treats the bremsstrahlung production with a class II system and knock-on electron production with a class I algorithm[4,5]. Even though there are fundamental differences in calculating the electron and photon transports, the differences are often small. Only under very specific conditions are the slight approximations, made in the ETRAN code, exaggerated[4]. The ETRAN was designed originally to cover energy regimes below a few mega-electron-volts, whereas the EGS was designed to cover up to giga-electron-volts[1]. Currently, however, both codes cover a wider range. In the low energy regime, the ETRAN handles low-energy transport more accurately than does the EGS[1]. However, there are exceptions, since for instance the EGS is able to deal with the coherent (Rayleigh) scattering at very low energies while the ETRAN lacks this ability[4]. Both systems contain aspects based on an assumption of free electrons that no longer holds for very low energies. Thus, care must be taken when using either system when energies below 100 keV are used, especially if the electrons are being transported through a high atomic number material where there is a relatively large uncertainty in the stopping powers and interaction cross-sections[1,7].

4.3 The EGSnrcMP user codes

Before explaining the codes three concepts unique to MC technique must be discussed: phase space file, pegs file, and energy cut-off.

A ***phase space*** is referred to as a file that contains information about the type of particles "scored" in a 2 dimensional plane as well as their individual energy and direction of travel. As explained earlier, the MC simulation simply "follows"

particles as they travel through and interact with matter. A phase space file then reflects how the MC code keeps a summary of all particles' information that have passed a user-defined plane. A phase space contains the most complete and fundamental information from which all other properties including spectral information can be extracted.

A ***pegs file*** is the core input file for all MC programs. It contains the cross-sectional information without which no simulation can be run. For each material of interest, the density, mean excitation energy, and compositional information are included and stored in the pegs file. In addition, a pegs file contains information on electron stopping power for a given material in a user-defined energy range.

To speed up MC simulations various variance reduction techniques can be used. One such technique includes termination of particle transport once the particle has reached a minimum energy and the local deposition of all the particle's remaining energy. The introduction of such a lower energy limit can speed up the simulation significantly without necessarily increasing the uncertainty in the results. The choice of an appropriate lower energy limit, also called an ***energy cut-off***, is highly dependent on the conditions of the specific simulation at hand. Generally, if one is concerned with megavoltage photons or electrons, a higher energy cut-off can be set, while, if one is working in the orthovoltage region, a lower energy cut-off is more appropriate. An appropriate electron cut-off energy (ECUT) is more important than a photon energy cut-off (PCUT), since the electron transport requires a greater CPU time. A commonly used PCUT for photons is 0.01 MeV, while for electrons an appropriate choice of ECUT may be anywhere between 0.512 MeV for kilovoltage applications up to 0.700 MeV or even higher for simulations involving megavoltage beams. A typical choice of ECUT is 0.521 MeV. Please note that ECUT contains the rest mass energy of the electron (0.511 MeV) as well as its kinetic energy. Hence, an ECUT of 0.512

MeV sets a 0.001 MeV (or 1 keV) lower energy limit on the electrons' kinetic energy.

4.3.1 *BEAMnrc*

Perhaps the most important MC code in this work, the BEAMnrc code[9], is a MC simulation system that allows users to model the radiotherapy sources. The user-code contains several different basic pre-programmed accelerator components (also called *c*omponent *m*odules, CM) that the user can combine to form the desired accelerator. Each of the basic CMs in turn includes several variables that allow the user to adjust the shape, dimension, and material of the particular module to the desired values.

Given a simulation, initially the user must input the properties of the desired incident beam before any output can be obtained. The BEAMnrc code allows for various source types, and for all sources the user is able to define the type of particles as well as their energies. An energy spectrum may also be selected as the source[4].

Of the 20 available CMs, the four used throughout this work (slabs, xtube, conestack, and chamber) are described below.

- The SLABS module allows the user to define one or more consecutive slabs of arbitrary thicknesses and materials.

- The XTUBE module was used in this work to simulate the target. This CM simulates an x-ray tube target and hence enables the user to extract a phase space file at a given angle to the incident beam. The target material and incident angle of the primary electron beam are also user-defined[10].

- The CONESTACK module consists of a stack of coaxial truncated cones surrounded by a cylindrical wall. Due to its geometry, it allows for simulation of primary collimators as well as scattering foils and other accelerator components.

- The CHAMBER module models a parallel plate chamber in a container with top and bottom planes of arbitrary thickness and material. The chamber module is the only CM in the BEAMnrc that allows the user to collect the dose, as opposed to phase spaces. The chamber module can also be used to model phantoms of arbitrary thickness and composition. This CM is ideal for PDD calculations, since the user is able to define several dose zones on the central axis, each with its unique thickness to accommodate different resolutions.

4.3.2 *DOSRZnrc*

The DOSRZnrc is another MC code that allows the transport of particles in a specific cylindrical geometry in any given medium. Although the BEAMnrc allows the user to collect the dose in a phantom material using the "chamber" CM, the DOSRZnrc provides a much greater flexibility in dose calculations. Generally, the BEAMnrc is more efficient in calculating phase space files, while the DOSRZnrc is more appropriate for "scoring" of dose or pulse height distributions.

The DOSRZnrc code has similar source type options as the BEAMnrc code. The modelling of geometry, however, is done by construction of a grid of user-defined widths and radii, and the subsequent assignment of appropriate material to each cell.

4.3.3 *Beamdp*

The beamdp is used to analyze and extract information from an existing phase space file. Since a raw phase space file is of no use to the user, the beamdp allows for determination of several indicators that are much more valuable than individual particle information.

The spectral information in this work has been obtained by using the beamdp. The user is given the option of choosing the energy bins. Of course, larger energy bins reduce the error in the value but lower the resolution at the same time.

To obtain the mean energy of a spectrum, the "mean energy distribution" option of the beamdp is used, and the number of energy bins is set to 1 to obtain a single mean energy value for the entire spectrum, as opposed to a mean energy distribution.

4.4 References

1 D. W. Rogers, B. A. Faddegon, G. X. Ding, C. M. Ma, J. We, and T. R. Mackie, "BEAM: a Monte Carlo code to simulate radiotherapy treatment units," Med. Phys. **22**, 503-524 (1995).

2 M. J. Berger, "Monte Carlo calculation of the penetration and diffusion of fast charged particles," Methods Comput. Phys. **1**, 135-215 (1963).

3 D. W. Rogers and A. F. Bielajew, "Differences in electron depth-dose curves calculated with EGS and ETRAN and improved energy-range relationships," Med. Phys. **13**, 687-694 (1986).

4 F. Verhaegen and J. Seuntjens, "Monte Carlo modelling of external radiotherapy photon beams," Phys. Med. Biol. **48**, R107-R164 (2003).

5 M. J. Berger and S. M. Seltzer, "Etran, Monte Carlo Code System for Electron and Photon Transport Through Extended Media," Documentation for RSIC Computer Code Package CCC-107, Oak Ridge Natl. Lab, Oak Ridge, Tennessee (1973).

6 R. L. Ford and H. M. Gerstenberg, "The EGS Code System (Version 3)," SLAC Rep. 210. Stanford University, Stanford, CA (1978).

7 I. Kawrakow, "Accurate condensed history Monte Carlo simulation of electron transport. I. EGSnrc, the new EGS4 version," Med. Phys. **27**, 485-498 (2000).

8 D. W. Rogers and A. F. Bielajew, "Monte Carlo Techniques of Electron and Photon Transport for Radiation Dosimetry," Dosim. of Ion. Rad. **3**, 427-539 (1990).

9 D. W. Rogers, C. M. Ma, B. Walters, S. B. Ding, and G. Zhang, "BEAMnrc Users Manual," National Research Council of Canada Report **PIRS-0509** (2002).

10 F. Verhaegen, A. E. Nahum, S. Van de Putte, and Y. Namito, "Monte Carlo modelling of radiotherapy kV x-ray units," Phys. Med. Biol. **44**, 1767-1789 (1999).

Chapter 5

METHODS AND MATERIALS

5.1 Introduction

In the first part of this chapter, the setup, techniques and instruments used in the experimental portion of this work are described in detail. In the second part, the parameters and techniques used to calculate our beam quality measurements using MC are examined.

To analyze the properties and behaviour of bremsstrahlung beams as a function of target material and angle, percentage depth dose and attenuation measurements were performed and results were compared against those obtained by Monte Carlo calculations. The mean energy and the effective energy of the beams were also calculated.

Percentage depth dose (PDD) can be used to describe beams of both megavoltage and kilovotage effective energy. Since a desire to compare the forward megavoltage beams and the orthogonal bremsstrahlung beams of greatly reduced mean energy existed, PDD seemed like an obvious choice. Moreover, PDD is a common beam specifier for clinical beams; its use will allow comparison of our beam results to those used clinically.

The attenuation of the beam was also measured by placing copper plates of various known thicknesses in front of the photon beam. Of course, a knowledge of the entire attenuation curve enables one to determine the values of the first and second half value layer. Although attenuation measurements are quite insensitive in the megavoltage energy range, as described in Chapter 3, we still selected this technique over the others, since much information about the spectrum of a beam can be obtained through a complete knowledge of its attenuation curve[1].

In addition to beam quality specifiers, images of various simple contrast objects were obtained using both the orthogonal and forward bremsstrahlung beams produced by several targets of different atomic number. The contrast levels of all images were qualitatively investigated and compared.

5.2 Experimental setup

Figure 5.1 compares the linac head configuration for current high energy linacs capable of portal imaging and the proposed setup for linacs capable of imaging with the orthogonal component of bremsstrahlung beams.

In this work, the Varian Clinac-18 linac installed at the Montreal General Hospital (MGH) was used to study the characteristics of the orthogonal component of bremsstrahlung beams. The bending magnet of the accelerator head was turned off, the monitor chambers were disabled, and the primary electron beam was made to exit through a beryllium window in the forward direction (research port). In order to allow the beam to exit centered and in a scatter-free manner, the bending magnets that are used to transport the clinical beam needed to be demagnetized by briefly running through them a reverse current.

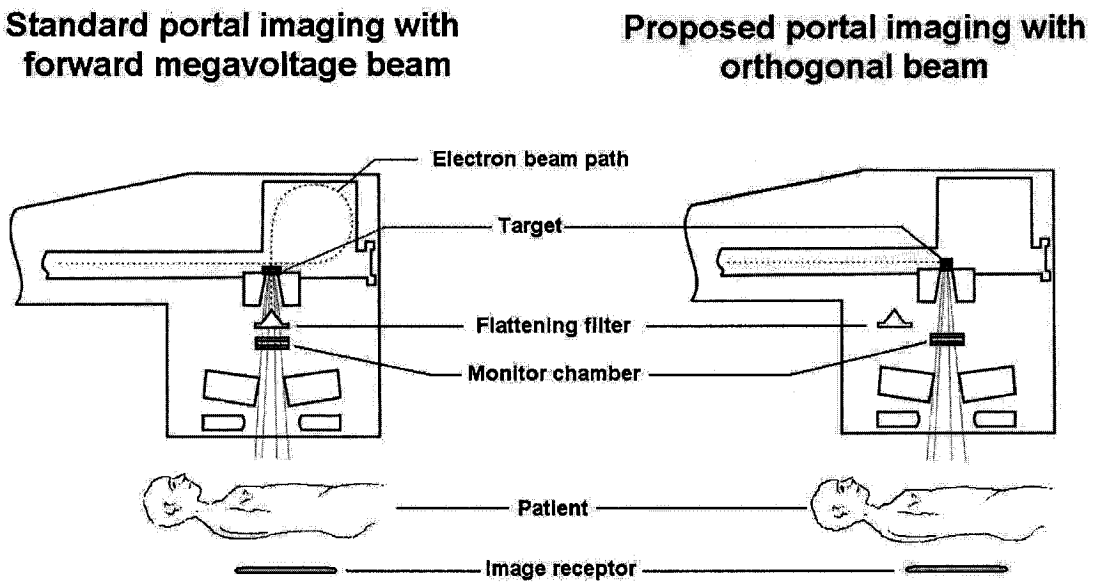

Figure 5.1: A schematic comparison between the linac head configuration for current portal imagers operating with the megavoltage forward beam (a); and our proposed technique of imaging using the orthogonal component of the bremsstrahlung beam (b).

As explained in Chapter 3, the photon yield is lower in the orthogonal direction than it is in the forward direction. Hence, the need to maximize the signal to background ratio for measurement of orthogonal bremsstrahlung beams was deemed important and in fact proved to be essential during the experimental phase of this work. It was observed that in the orthogonal direction, the yield from low atomic number targets was too low to make PDD measurements past depths of few centimeters possible. The background level was at times up to 15% of our readings, and the leakage current (dark current) of the chamber also proved to be substantial, counting for as much as 10% of the signal. Although increasing the exposure time enhances the signal to background ratio, it does not significantly reduce the error introduced due to the leakage current.

In order to improve the accuracy of our measurements, we determined that the machine needs to be operated in the "photon mode" in which the linac produces roughly a thousand times greater fluence of electrons than what is normally emitted when operated in the "electron mode."

Although the high bremsstrahlung yield in the forward direction results in a large signal to noise and signal to background ratio even when the machine is operated in the electron mode, the same settings as in the orthogonal direction were used for the sake of consistency. The polarity correction was negligible for all our measurements.

Although in the electron mode the Clinac-18 could produce electrons with energies as low as 6 MeV, when operated in the photon mode we only had access to 10 MeV electrons. Use of higher energy electrons in fact turned out to be advantageous. It was determined that for electron energies below 10 MeV, the electron beam divergence in air is unacceptably large[2] resulting in very little control over the positioning of the beam on the target. We measured that a 10 MeV electron beam immediately after exiting the beryllium window has a Gaussian fluence spectrum with a FWHM of 2 mm. After traveling through 26 cm of air, the length of the research port, the beam's fluence spectrum was measured to have a FWHM of 8.5 mm. Although narrower beams would have been preferable, the 10 MeV broad beam was deemed acceptable and actually resulted in good agreement between experimental data and calculated ones.

To summarize, for all PDD and attenuation measurements in this work, the Clinac-18 was operated in the photon mode to produce 10 MeV electrons that were made to strike three different targets: carbon, aluminum, and copper. Except correcting for the background, no other correction factors were applied to our readings. The error introduced due to ignoring the leakage, polarity, and temperature and pressure corrections was measured to be lower than 2% and was taken into account when displaying the error bars.

The exact direction of electron propagation was determined by shining back a laser light through the centres of the images produced on two pieces of HD Gafchromic films placed directly in front of the electron beam outside the research port at a separation of 10 cm.

The target was positioned with respect to the laser beam such that in the orthogonal direction the distance between the centre of the electron beam to the target edge was 8.5 g/cm^2 for carbon, 13.5 g/cm^2 for aluminum and 22.8 g/cm^2 for copper (refer to Fig. 3.9 for a schematic diagram of target setup). In the forward direction the thickness of the target was set to 11.9 g/cm^2 for carbon, 14.8 g/cm^2 for aluminum and 40.0 g/cm^2 for copper. The thickness values were experimentally optimized for our settings in order to minimize the electron contamination emerging from of the target.

For contrast measurements, however, a 6 MeV electron beam, the lowest available electron energy on the linac, was used, while the linac was operated in the electron mode. It was experimentally determined that the Agfa 400 diagnostic films used in this work were sensitive enough to radiation to produce images of acceptable contrast levels even in the presence of low photon fluences[3]. The choice of the lowest available electron energy on the Clinac-18 was made in an attempt to minimize the mean energy of the resulting orthogonal bremsstrahlung beam and hence improve the image contrast. Our inability to position the beam accurately on the target as a result of its broadness was not significant since the film contrast levels were only analyzed qualitatively.

5.2.1 *Percentage depth dose setup*

Figures 5.2 and 5.3 show the schematic diagram and a photograph of the experimental setup used to measure PDD in the orthogonal direction. Since in our setup, the primary beam did not travel through the linac's monitor chambers, an NE2571 (Nuclear Enterprises, Fairfield, NJ) Farmer type chamber with a collecting volume of 0.6 cm^3 was placed in front of the beam throughout all measurements to monitor the fluctuations in electron output of the Clinac-18.

A Wellhöfer PPC40 (Scanditronix Wellhöfer North America, Barlett, TN) parallel plate chamber with a collecting volume of 0.4 cm^3 was used to measure the PDD. The small collecting volume improves the positional accuracy of the chamber. Moreover, the parallel plate chamber allows us to measure the surface dose as well as the energy deposited at larger depths in phantom.

Certified solid water slabs of known densities and thicknesses were used for PDD measurements. A specially designed stand was used to hold solid water slabs in a vertical position, while squeezing them to remove any air gap during the time of the measurement (Fig. 5.3). Lead collimation was added at a distance of 16 cm from the incident electron beam's central axis in the orthogonal direction and 75 cm in the forward direction. The collimation consisted of solid 10 cm lead blocks placed in front of the beam with the centre block containing an opening of radius 1.5 cm. In both the orthogonal and forward setups, the solid water slabs were positioned such that the surface of the front slab was 9 cm away from the collimator.

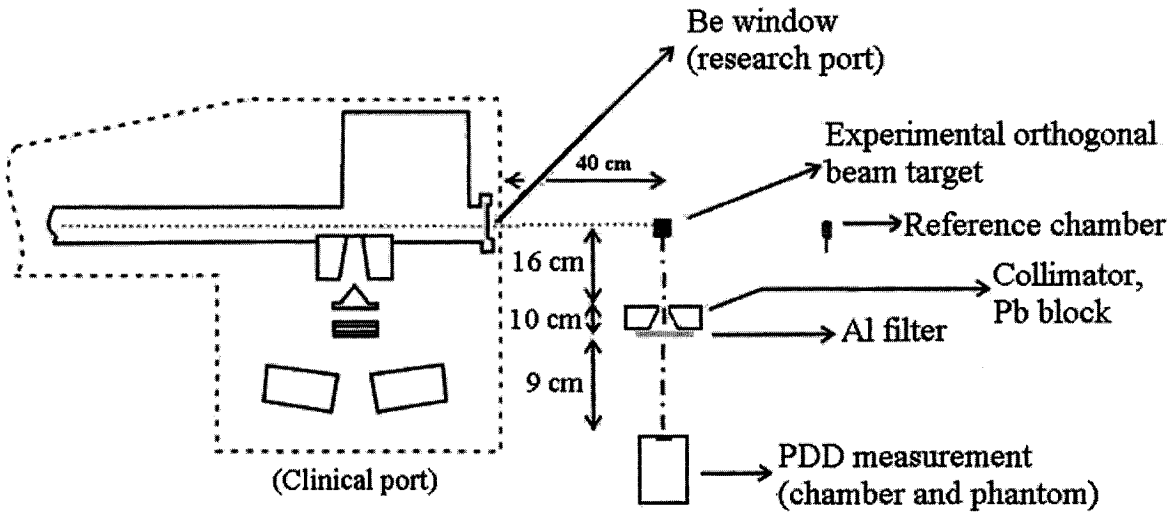

Figure 5.2: A schematic diagram of the percentage depth dose measurement setup in the orthogonal direction. The thickness of the aluminum filter was 2 mm for carbon targets, and 3 mm for aluminum and copper targets. The linac was operated in the photon mode. A fan, not shown, was used at all times to cool the target in order to prevent overheating.

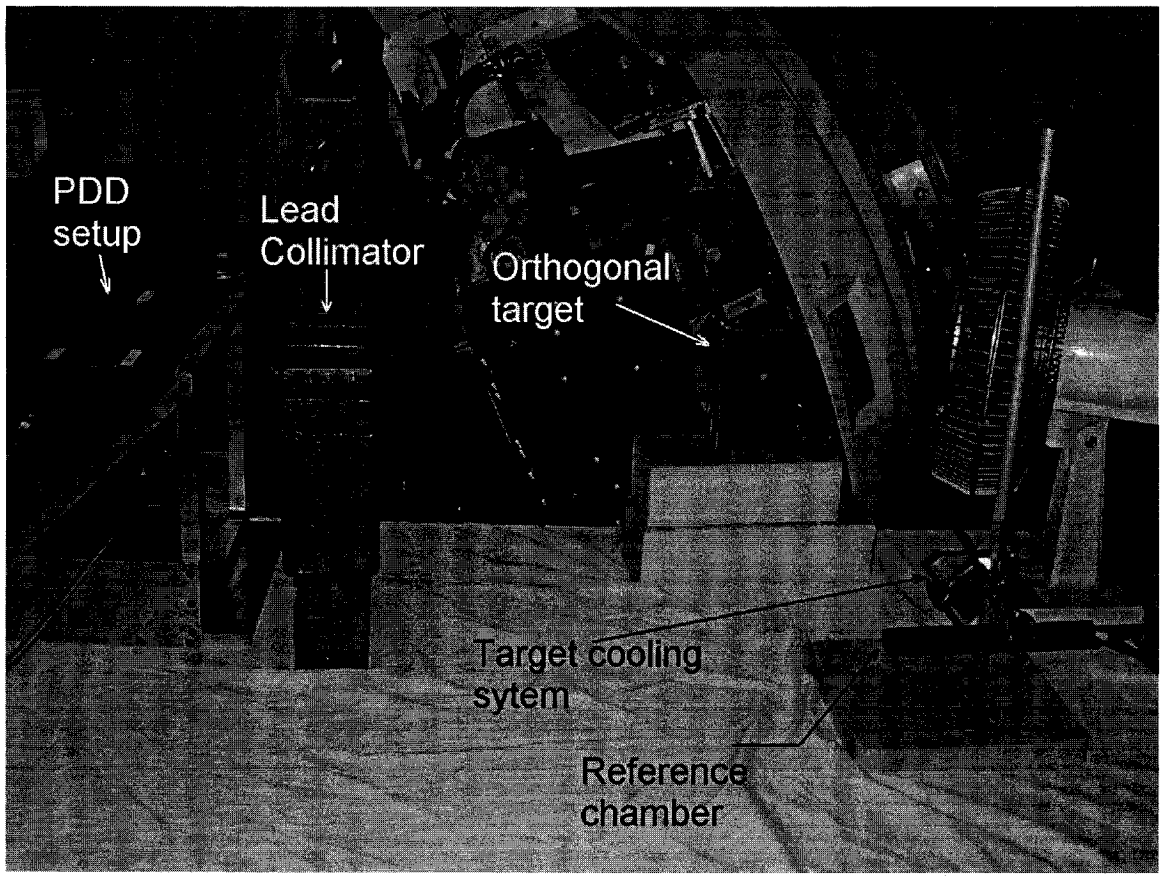

Figure 5.3: A diagram of the actual experimental setup with major components identified. The reference chamber identified is an NE2571. The chamber used for PDD measurement is a Wellhöfer PPC40 parallel plate chamber.

We established that only a primary collimator placed directly in front of the primary bremsstrahlung beam, as shown in Fig. 5.2, is sufficient to collimate the beam and remove the majority of scattered particles. Although further collimation around the chamber would reduce the background contribution of the reading, we determined that a simple background correction can also account for all the scattered radiation. Our background correction technique is described later in this chapter.

Aluminum filters were also placed behind the collimator opening, as shown in Fig. 5.2. These were used to filter out the contaminating electrons that left the target or were produced in the collimator. We determined that the contamination

is large enough to significantly reduce the accuracy of our results. The filter thickness values were measured experimentally for our settings. This was in fact done through measuring the attenuation of the beam in the filter material and plotting the results on a logarithmic scale. The exponential attenuation of a clean beam in aluminum is well-known. We rationalized that for a contaminated beam, the low energy contaminating electrons would result in a higher than expected chamber reading. As the thickness of the filter material is increased, a greater fraction of the contaminating electrons is removed from the beam. Figure 5.4 shows the result of such an experiment performed for a 10 MeV beam striking a carbon target. It is clear that, for aluminum filter thicknesses smaller than 2 mm, the dose deposited by the contaminating electrons results in a higher than expected ionization reading. The initial sharp drop of the chamber reading corresponds to the removal of contaminating electrons from the beam. For filter thicknesses greater than 2 mm, however, the expected exponential attenuation of a clean beam is recovered attesting to the removal of the majority of contaminating electrons. The exponential attenuation of the beam is shown by the straight line on the logarithmic scale of Fig. 5.4. For aluminum and copper targets the thickness of the aluminum filter was found to be 3 mm.

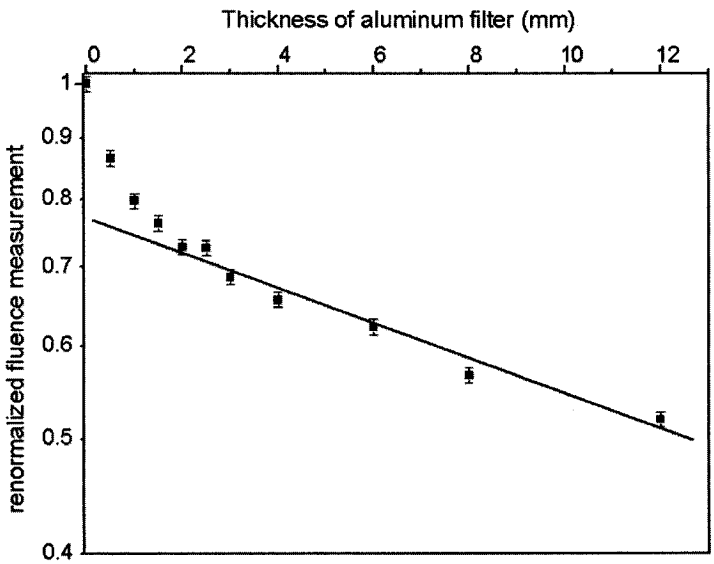

Figure 5.4: Renormalized ionization chamber measurements for a 10 MeV electron beam striking a carbon target as a function of the thickness of aluminum filters placed directly in the path of the beam.

Finally, as shown in Fig. 5.3, a fan was used at all times to cool down the target, since the high fluence of electrons would otherwise result in overheating of the target.

5.2.2 *Attenuation measurement setup*

Figure 5.5 shows the experimental setup for the measurement of the attenuation curve in the orthogonal direction. In this experiment, copper was selected as the attenuating material. To measure the attenuation, copper plates of known thicknesses were placed in front of the collimator opening on the side facing the target. In the orthogonal setup, an Exradin ball chamber model A4 (Standard Imaging, Inc., Middleton, WI) with a collecting volume of 30 cm^3 was employed. Although such a large volume chamber drastically increases the signal to background ratio, it also increases the scatter component of the reading. The increased contribution of scattered photons to the signal was corrected for by performing background measurements, as described at the end of this section. Moreover, accurately determining the exact position of a chamber of such large volume is difficult, although fortunately positional accuracy is relatively un-important for accurate attenuation measurement. The reason is that throughout the entire length of the measurement, the chamber to source distance is not altered, while all the readings are normalized to the initial beam fluence. In this experiment the source to chamber distance was set to 35 cm in the orthogonal direction and 97 cm in the forward direction, identical to the SSDs used for PDD measurements.

It should be noted that the setup for attenuation measurement in this experiment did not comply with the "good-geometry" setup described in Chapter 3. We established, however, that in spite of the absence of a pencil-sharp beam and a small volume ionization chamber, the results obtained are significant and reproducible.

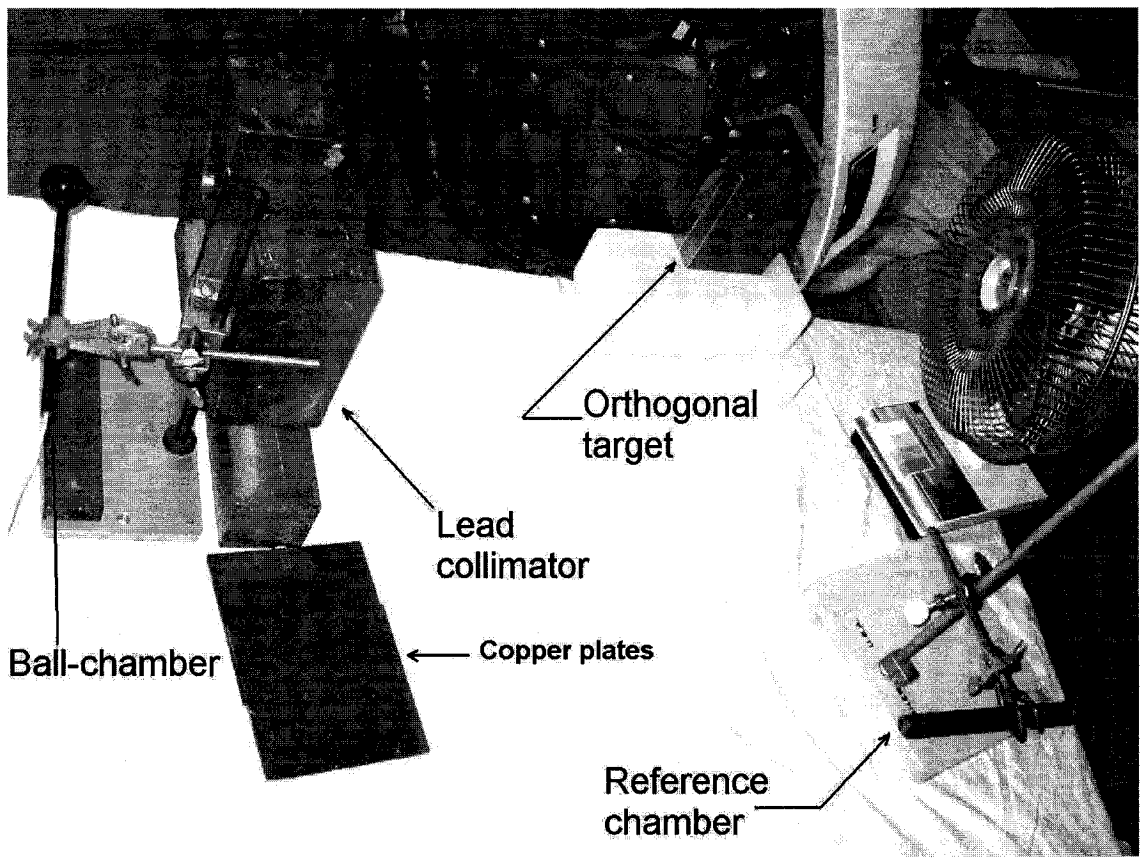

Figure 5.5: A diagram of the experimental setup for the attenuation measurement of the orthogonal component of a bremsstrahlung photon beam produced by 10 MeV electrons striking a target material.

Since in the forward direction the bremsstrahlung yield is much larger, we used a smaller volume PPC40 chamber for attenuation measurements. All measurements using the PPC40 were made at a depth of 25 mm in solid water to provide the chamber with sufficient build-up in the high energy beam.

Removal of contaminating electrons by filtering the beam was unnecessary in the attenuation measurement setup, because the copper attenuators acted as filters themselves. Only the initial reading of the beam intensity that was made in the absence of any copper attenuator was strongly affected by the electron contamination.

For both PDD and attenuation measurements, background contribution was measured for every individual reading by the so-called "shadow technique". This was done by completely blocking the collimator opening with a piece of lead, thick enough to attenuate the primary beam to roughly 0.4% of its initial fluence. The experiment was then repeated and any reading at this stage was attributed to background and scatter. Subsequently, every reading was corrected for its corresponding background and scatter contribution.

Table 5.1 above has been included to summarize the properties and specifications of all chambers used in this work in more detail. As noted, the Keithley 6517A electrometer was used for all measurements. The electrometer was operated in charge (Coulomb) mode. The nominal voltage applied to the chambers was +300 V. The polarity supplied to the chambers positively biased the inner electrode and grounded the outer electrode (a configuration known as positive polarity). Our warm up procedure involved connecting the chamber and turning on the electrometer ten minutes prior to irradiation and pre-irradiating the chamber with approximately 15 Gy.

Ionization Chamber	**NE2571**	**Exradin ball chamber (A4)**	**PPC40**
Sensitive Volume	0.69 cm^3	30 cm^3	0.40 cm^3
Wall material	Graphite (1.70 g/cm^3)	Shonka C552 (1.72 g/cm^3)	Polymethyl Methacralate (PMMA) (1.19 g/cm^3)
Wall thickness	0.36 mm	0.50 mm	0.67 mm
Inner diameter of outer electrode	6.3 mm	38.2 mm	N/A
Length of inner electrode	20.5 mm	25.1 mm	N/A
Collecting electrode diameter	N/A	N/A	16.0 mm
Electrode separation	N/A	N/A	2.0 mm
Electrometer	Keithley 6517A	Keithley 6517A	Keithley 6517A

Table 5.1: Ionization chamber construction properties and specifications, as well as associated electrometers used.

5.2.3 *Contrast measurement*

Figure 5.6 shows schematically the experimental setup for contrast measurement setup in the orthogonal direction. In this experiment, the linac was operated in the electron mode at 6 MeV. The details of the setup are similar to those of the PDD measurement except that a 5 mm layer of polymethyl methacrylate (PMMA) filter was used (instead of the aluminum filters) to reduce the effects of the electron contamination emerging from the target. The thickness of the PMMA filter was determined experimentally by comparing the image contrast of films that were filtered with various thicknesses of PMMA plates. We observed that as the thickness of PMMA filter was increased, an initial rapid drop in film darkening occurred. For PMMA thicknesses larger than 5 mm, however, a relatively low and constant film darkening level was obtained. Therefore, we rationalized that a PMMA thickness of 5 mm is sufficient to remove the majority of low energy contaminating electrons that would otherwise deposit their energy in a thin layer of film.

Several image receptors were attempted for this part of the experiment: computed radiography (CR) plates, Agfa® 400 diagnostic quality films, EBT Gafchromic® films, and PP-L Kodak® portal ready-pack therapy quality films. The EBT Gafchromic films required long exposure times (when the linac was operated in the electron mode) before any significant film darkening occurred. The therapy quality films produced poor contrast compared to the diagnostic films because of their wider characteristic curves. CR plates and Agfa 400 diagnostic films were both desirable candidates, since with relatively short exposure times, large contrast levels could be achieved. We selected the diagnostic films over CR plates, however, due to the films' better resolution. The sharp characteristic curve of the Agfa 400 diagnostic films resulted in high contrast levels as long as care was taken not to overexpose the films and exceed their saturation point. Figure 5.7 schematically shows the simple contrast objects that were imaged in this work.

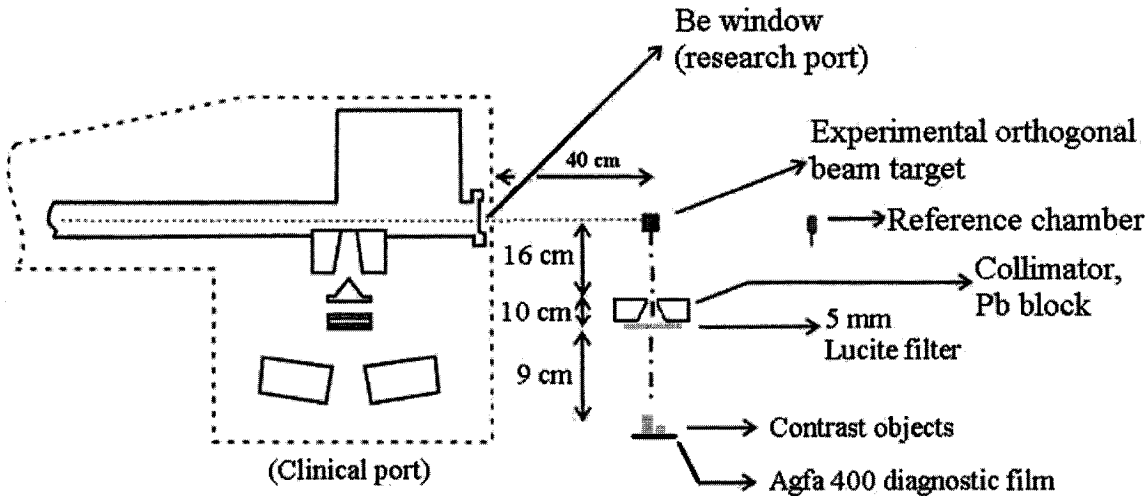

Figure 5.6: A schematic diagram of the image contrast measurement setup. Agfa 400 diagnostic films were used for all image contrast measurements.

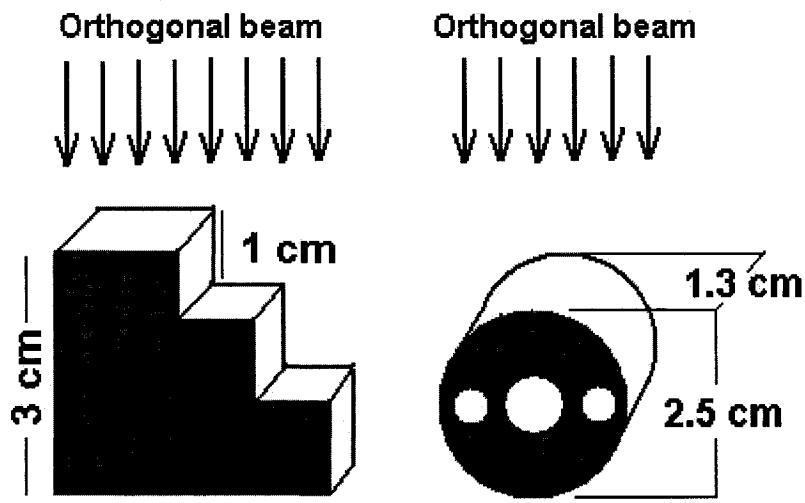

Figure 5.7: A schematic drawing of the simple test objects used to evaluate the contrast level of our images. The cylindrical test object is 25 mm in diameter with a large central hole of 9 mm in diameter, and two smaller holes of 5 mm in diameter each. The central hole contains grooves of thickness of 0.7 mm. The 'step' object is made of polymethyl methacrylate (PMMA) with a density of 1.19 g/cm^3, and the cylindrical test object is made of nylon with a density of 1.15 g/cm^3.

5.3 Monte Carlo simulations

The target and the primary incident electron beam were simulated and a phase space file was obtained immediately after the target using the BEAMnrc code. This was deemed to be the most efficient technique of calculating PDD and attenuation, since the same initial phase space file could have been used for both experiments. Hence, the time-consuming task of transporting the incident electrons through the target and collecting a phase space in the orthogonal or forward direction did not have to be repeated for every experiment.

The simulation of the target in the orthogonal direction involved using the XTUBE component module with a target tilt of zero degrees, as shown in Fig. 5.8. In the forward direction the SLAB component module was used. It was established that approximating the shape of the incident beam to be circular with a diameter equalling the FWHM of the measured Gaussian shaped fluence of the actual beam was acceptable. Although ECUT values as low as 512 keV along with the Rayleigh scattering option turned on were initially used, we determined that in fact an ECUT of 521 keV with the Rayleigh scattering option turned off produces similar results, while significantly reducing the simulation time. Boundary crossing algorithm was set to EXACT and electron-step algorithm was set to PRESTA-II. Furthermore, for all our simulations, the Koch-Motz (KM) bremsstrahlung angular sampling data and the National Institute of Science and Technology (NIST) bremsstrahlung cross sectional data were used[4]. Spin effects and bound Compton scattering were also both turned on. Although insignificant, there was a 0.003 g/cm^3 difference in the density of the simulated solid water and that used in the actual experiment.

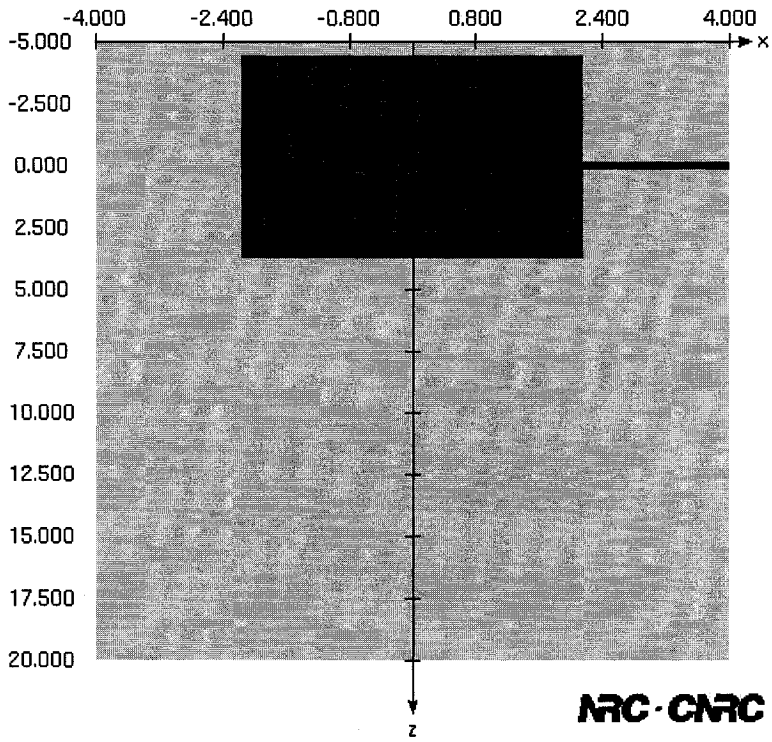

Figure 5.8: A preview of the target simulation in the orthogonal direction. The target has been created using the XTUBE module and is the dark colour rectangular shaped object. The incident electron beam has been indicated as the straight horizontal line incident on the target. A large phase space file is collected 20 cm downstream from the reference point (in the z-direction).

5.3.1 *Percentage depth dose simulation*

The PDD was calculated using both the DOSRZnrc code as well as the BEAMnrc code. We compared the two techniques and established that both methods return identical results to within the range of uncertainty. However, we further determined that the use of DOSRZnrc in determining the PDD requires significantly lower computational time. Both techniques will be explained below, although it should be noted that for the majority of the Monte Carlo PDD calculations, the DOSRZnrc was the only technique used.

In the BEAMnrc technique, the initial phase space collected just past the target was used as the source and the entire experimental setup was fully simulated, as shown in Fig. 5.9. The CHAMBER module was used to simulate the phantom and the dose was calculated in 8 mm radius voxels along the central axis of the beam. The first 15 voxels had a thickness of 3 mm for increased resolution in the build-up region, while the thickness was increased to 10 mm for subsequent voxels in order to reduce the uncertainty on the dose.

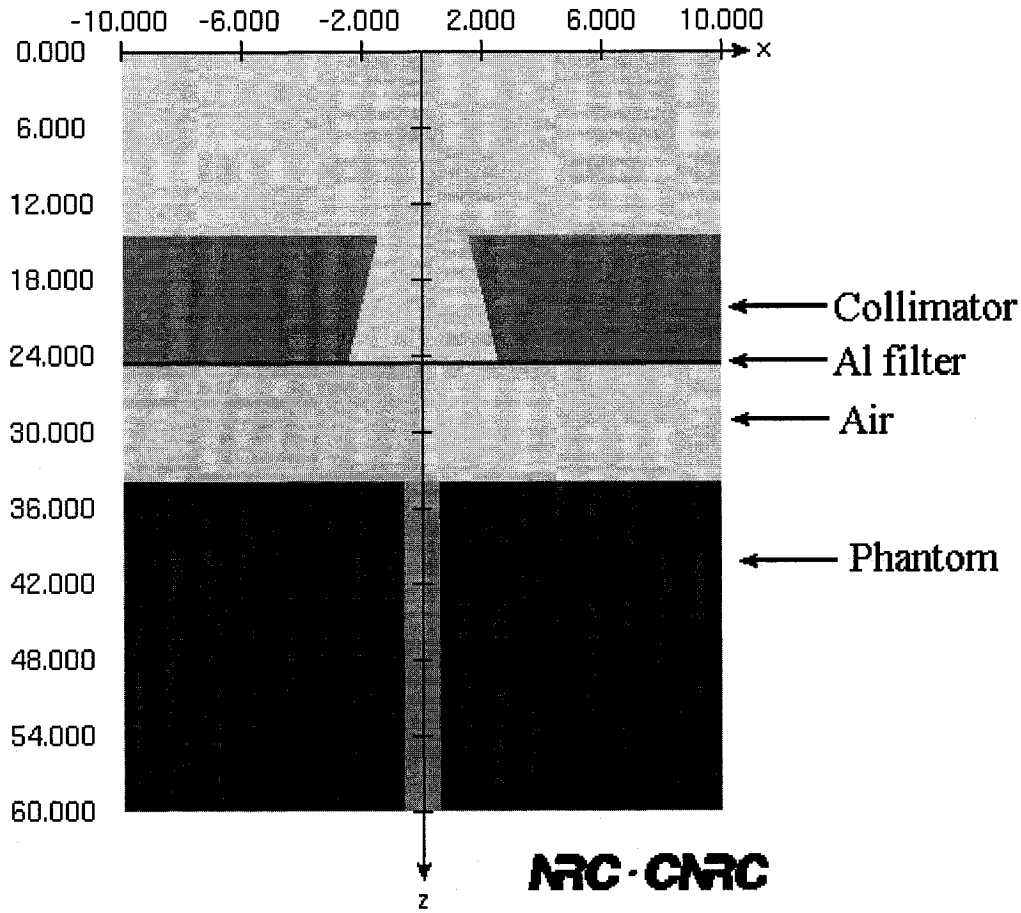

Figure 5.9: A preview of the simulation fully describing the main components of our setup. The lead collimator, the aluminum filter as well as the phantom materials have been indicated. The colour of the central axis of the phantom material has been slightly changed to show the 8 mm radius width of the volume that the PDD was collected in. The phase space file obtained from Fig. 5.7 was used as the source and was positioned at the reference depth (z = 0 cm).

In the DOSRZnrc technique, a photon spectrum was extracted from the initial phase space file using the beamdp code. It is important to note that, unless otherwise stated, for all phase space manipulations using the beamdp program only the photons present in an area of 1 cm radius around the central axis of the phase space file were used. All other particles in the phase space file (a relatively constant contribution of 1% for the carbon target, 1.5% for the aluminum target, and 6.5% for the copper target) were ignored.

In the process of obtaining a spectrum from a phase space file, the user is prompted to provide the number of energy bins ΔE. A maximum of 200 bins can be used. A choice of an appropriate ΔE is somewhat arbitrary, although a small ΔE results in a better resolution, while a large ΔE results in smaller uncertainty on the fluence of photons per energy bin. In this work, often the energy distribution spectrum was split into 150 bins, each of roughly 67 keV.

The DOSRZnrc user-code was subsequently used with a point source emitting a spectrum of photons, as given by the previously calculated spectral distribution. The collimator was not simulated in this technique, while its effect was indirectly taken into account by setting the source to emit photons in a solid angle defined by the size of the collimator's opening. The aluminum filter and the phantom were simulated in the process.

It is obvious that this technique is much more efficient that the first, since the majority of the photons that are emitted by the source reach the phantom. This is not the case with the BEAMnrc code because many of the particles are attenuated in the lead collimator. Not only would this result in greater uncertainty in the final results, but it would also increase the simulation time. As explained in Chapter 4, particle transport, especially in high density materials, is very demanding on the CPU time.

5.3.2 *Attenuation simulation*

Using the beamdp user-code, a spectrum was extracted from the phase space data taking only the photons into account, as described in Section 5.3.1. With a full knowledge of the spectrum, its resulting attenuation and HVL values can be determined. This was done through a simple in-house made program which calculated the attenuation of the spectrum through different thicknesses of copper.

Using this program, each energy bin of the full spectrum was treated as a mono-energetic beam; thus any given spectrum was represented by a sum of many mono-energetic beams each weighted by the relative photon fluence of their respective energy bins. Using this approximation, the simple attenuation equation $I = I_o e^{-\mu d}$ was applied to each energy bin. The attenuation of the heterogeneous beam by a copper attenuator was found by considering its cumulative effect on each mono-energetic component of the beam, as shown in Eq. (5.1)

$$Attenuation = \frac{\sum \left\{ \left(E_i \phi_i \mu_{en}^{air}(E_i) \right) \times \left(e^{-\mu_m^{Cu}(E_i)\rho_{Cu}x} \right) \right\}}{\sum E_i \phi_i \mu_{en}^{air}(E_i)} \qquad (5.1)$$

where,

E_i	is the energy of the i^{th} bin (MeV)
ϕ_i	is the normalized fluence of the i^{th} bin
$\mu_{en}^{air}(E_i)$	is the energy absorption coefficient in air calculated at E_i (cm^{-1})
$\mu_m^{Cu}(E_i)$	is the mass attenuation coefficient in copper calculated at E_i (cm^2/g)
ρ_{Cu}	is the density of copper (8.960 g/cm^3)
x	is the thickness of copper material placed in front of the beam (cm)

5.3.3 *Photon fluence and charged particle contamination*

In addition to the beam quality measurements that were discussed in the previous sections, the dependence of the photon yield and charged particle contamination on the target material and target thickness in the orthogonal direction were investigated using Monte Carlo simulations. The ability to understand and control both quantities proved invaluable throughout this project. For imaging purposes, a high photon yield and minimal charged particle contamination are most desirable.

In our simulations, the photon yield is defined as the ratio of the number of photons reaching the phase space file to the total number of primary incident electrons. Furthermore, we define charged particle contamination as the ratio, expressed as a percentage, of the number of charged particles reaching the phase space over the total number of primary electrons incident on the target material. Since the majority of contaminating charged particles were electrons, we use the terms 'charged particle contamination' and 'electron contamination' interchangeably.

Figure 5.10 shows the geometry used in this study. In order to standardize our target thickness measurements within different experiments, the thicknesses were measured in terms of the percentage of the CSDA range of the electrons striking the targets.

To study the dependence of photon yield and electron contamination on target thickness in the orthogonal direction, the thickness *x,* as indicated in the Fig. 5.10, was varied between 5% to 160% of the CSDA range of the primary incident electrons in the target material. Two different incident electron energies of 6 and 10 MeV were made to strike two targets of carbon and lead. The photon yield and electron contamination were both determined by analyzing the resulting phase space file with the beamdp user-code.

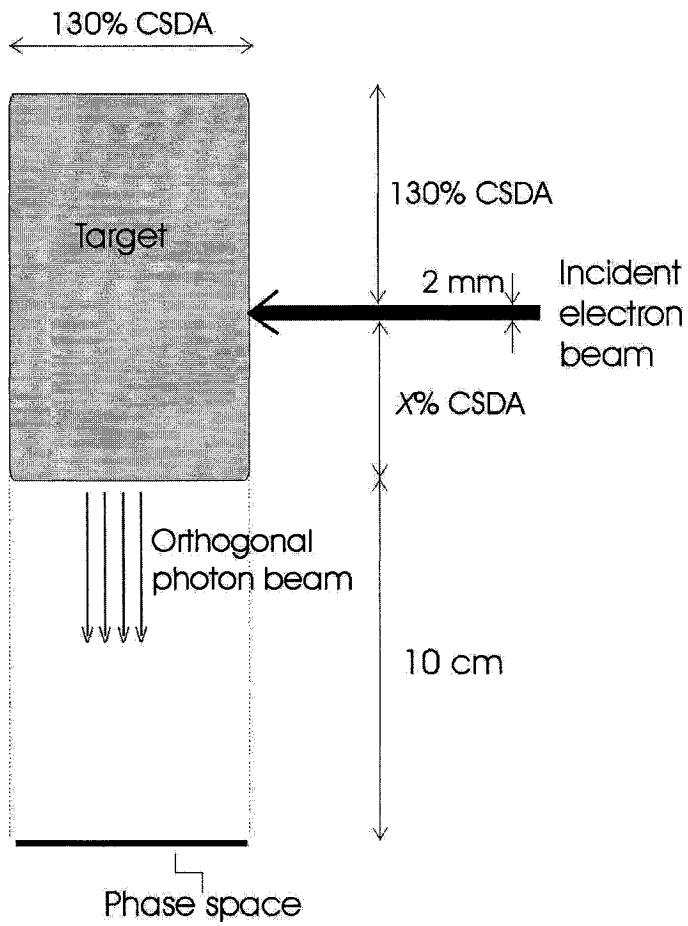

Figure 5.10: The simulation geometry used to determine the photon yield and electron contamination as a function of target thickness and target material in the orthogonal direction. Target thicknesses have been indicated in terms of the percentage of the CSDA range of the incident electrons in the target material.

For the second part of this study, the dependence of photon yield and electron contamination on the target material was studied. Table 5.2 summarizes the important properties of the ten different target materials that were simulated. In this part, the target thickness in the orthogonal direction *x* was fixed to 80% of the CSDA range of the incident electrons when a 6 MeV electron beam was made to strike the targets. In the case of a 10 MeV incident electron beam, *x* was set to 110% of the CSDA range of the primary incident electrons in the target material.

Target Material	Atomic Number (Z)	Density (g/cm^3)	CSDA range of 10 MeV electrons in target (cm)
Beryllium (Be)	4	1.848	3.41
Graphite (C)	6	1.700	3.33
Aluminum (Al)	13	2.699	2.17
Silicon (Si)	14	2.330	2.42
Titanium (Ti)	22	4.540	1.34
Copper (Cu)	29	8.960	0.69
Silver (Ag)	47	10.500	0.58
Tantalum (Ta)	73	16.654	0.37
Gold (Au)	79	19.320	0.32
Lead (Pb)	82	11.350	0.54

Table 5.2: The properties of various target materials used in a study of photon yield and electron contamination dependence on the quality of the absorbing material. The density and CSDA range have been obtained from the National Institute of Standards and Technology (NIST).

5.4 References

1 M. Scheithauer, M. Schwedas, T. Wiezorek, A. Keller, T. G. Wnedt, and D. Harder, "Erhohung der Genauigkeit der Laplace-Transformations-methode zur Bestimmung des Bremsstrahlungsspektrums klinischer Linearbeschleuniger," Z. Med. Phys. **13**, 22-29 (2003).

2 C. M. Ma and S. B. Jiang, "Monte Carlo modelling of electron beams from medical accelerators," Phys. Med. Biol. **44**, R157-R189 (1999).

3 J. R. Sykes, H. V. James, and P. C. Williams, "How much does film sensitivity increase at depth for larger field sizes?," Med. Phys. **26**, 329-330 (1999).

4 F. Verhaegen and J. Seuntjens, "Monte Carlo modelling of external radiotherapy photon beams," Phys. Med. Biol. **48**, R107-R164 (2003).

Chapter 6

RESULTS AND DISCUSSION

6.1 Introduction

In this chapter the results of our experimental and Monte Carlo studies on the quality of orthogonal and forward bremsstrahlung beams are presented and analyzed. In many of the figures presented in this chapter, the error bars for MC results have been omitted for better clarity. However, in all such cases, the uncertainty on the MC values is smaller than 1%.

6.2 Percentage depth dose

Figure 6.1 shows the PDD results obtained for the orthogonal and the forward bremsstrahlung beams. Although the PDD measurements have been carried out in solid water, the values have been adjusted to reflect an equivalent PDD measurement in water. For each target, the experimental PDD results (solid curves) and the respective MC-calculated PDD findings (symbols) have been plotted to allow for better comparison of the two.

The experiment for each target material was repeated between two to five times on different sessions (i.e., on different days) using identical setups. A best-fit curve describing each set of experiments was obtained using Tablecurve® software. The best-fit curves from various sessions were subsequently averaged and the uncertainty on the final curve was determined. The experimental curves shown in Fig. 6.1 have been obtained using this technique.

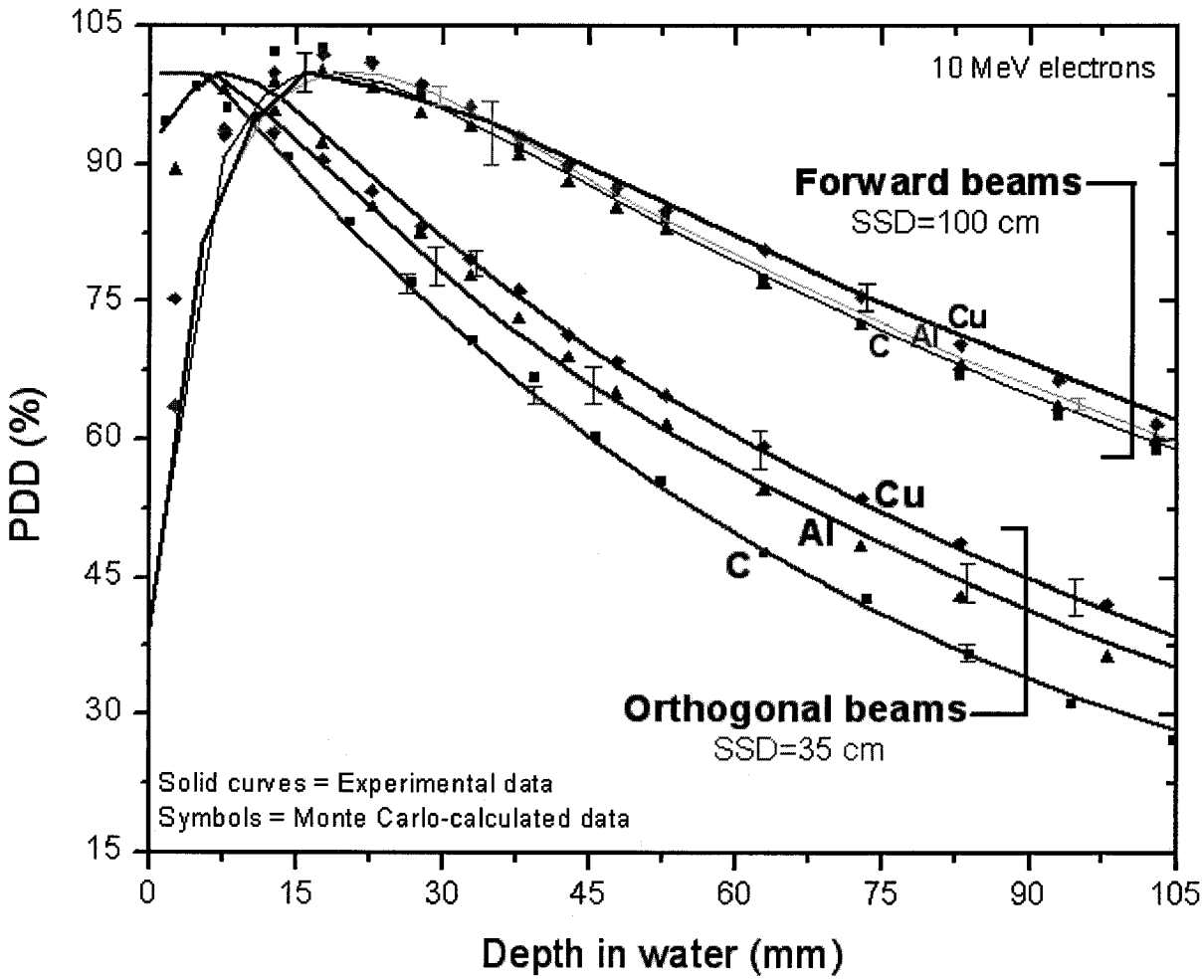

Figure 6.1: PDD results for forward and orthogonal beams produced by a 10 MeV electron beam incident onto C, Al, and Cu targets. Note that the PDD measurement for the forward beam is performed at an SSD of 97 cm, while in the orthogonal direction the SSD was set to 35 cm.

Figure 2.9 showed Faddegon et al.'s results[1] of mean energy of beams produced by 15 MeV electrons striking targets of beryllium, aluminum and lead as a function of angle. We can find strong agreement between our PDD results shown in Fig. 6.1 and the results obtained by Faddegon (at the lower energy threshold of E_0 = 145 keV). From our experiment in the forward direction, the carbon and aluminum targets result in PDD curves that are very similar. This agrees well with Faddegon's observation of the similarity of the mean energy of beams produced by two targets of beryllium and aluminum. Moreover, in our experiment the forward PDDs of beams produced by the carbon and aluminum targets have a smaller depth of maximum dose and fall more rapidly than the PDD of the photon beam produced by the copper target. Both characteristics suggest that the beams produced by the lower atomic number targets are slightly softer than the beam produced by the copper target. Again, this agrees with Faddegon's findings that a lead target (a distinctly higher atomic number target than the other targets used in his experiment) produces a beam of higher mean energy than do beryllium and aluminum targets.

In the orthogonal direction, our results also agree with what we anticipated. Faddegon et al.[1], Podgorsak et al.[2], and Nordell et al.[3] all concluded from their research findings that at large angles, higher atomic number targets produce beams of higher mean energy. From the depth of maximum dose and the slope of the PDD fall-off, we can also conclude that in the orthogonal direction, the effective energy of higher atomic number targets is in fact significantly higher than that of beams produced by lower atomic number targets. The reason for this effect was explained by Podgorsak et al.[2] and is discussed in detail in Section 2.4.2.

Since the orthogonal and forward PDD measurements were not performed at the same SSD, they cannot directly be compared in Fig. 6.1. Hence we have included Fig. 6.2 in which we have simulated our setup geometry and have adjusted the SSD in both the orthogonal and forward directions to 97 cm.

Therefore, all calculations have been performed under identical simulated setups. In the forward direction, only the PDD for copper target has been shown to maintain clarity.

By using the depth of maximum dose z_{max} and the gradient of the PDD fall-off past z_{max} as indicators of a beam's effective energy, we conclude that, for a given target material and incident electron energy, the orthogonal component of the bremsstrahlung beam is always softer than the forward component. Moreover, the difference between the two effective energies is strongly dependent on the target material used to produce the beams and is significantly larger for lower atomic number targets in comparison with high atomic number targets.

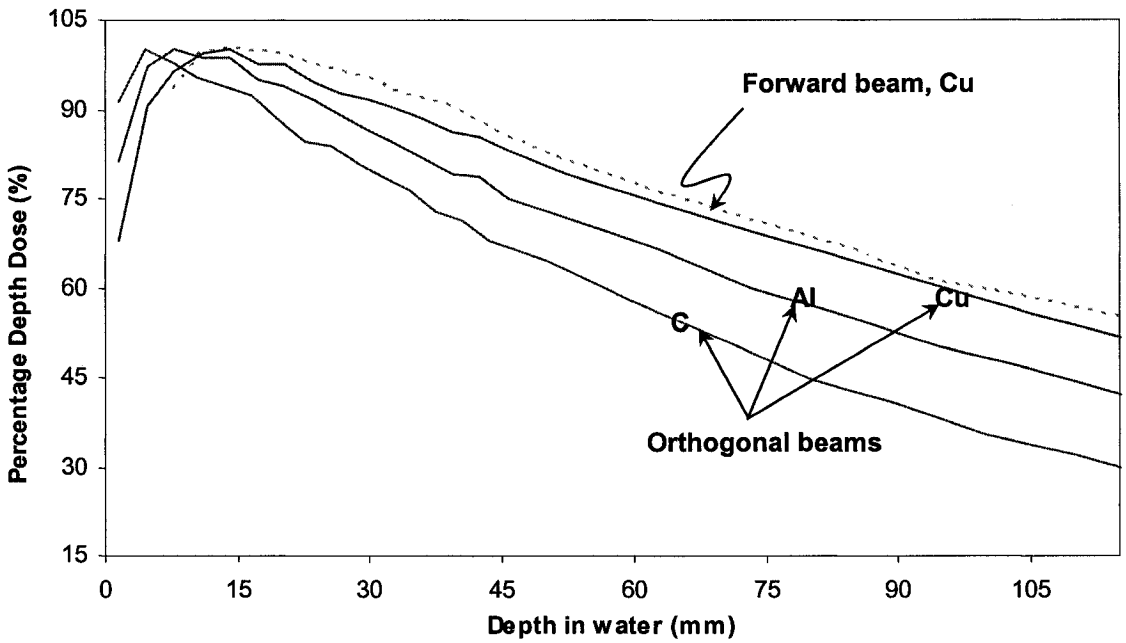

Figure 6.2: MC-calculated PDD results for forward and orthogonal bremsstrahlung beams produced by a 10 MeV electron beam incident on carbon, aluminum and copper targets. All simulations are carried out for an SSD of 97 cm.

6.3 Attenuation measurements

Figure 6.3 shows our attenuation measurement results. In the forward direction, only the attenuation curve for the aluminum target has been shown because there is little difference between attenuation of beams produced by various targets. The attenuation measurement, as described in Chapter 3, is a relatively insensitive beam quality specifier in high energy ranges.

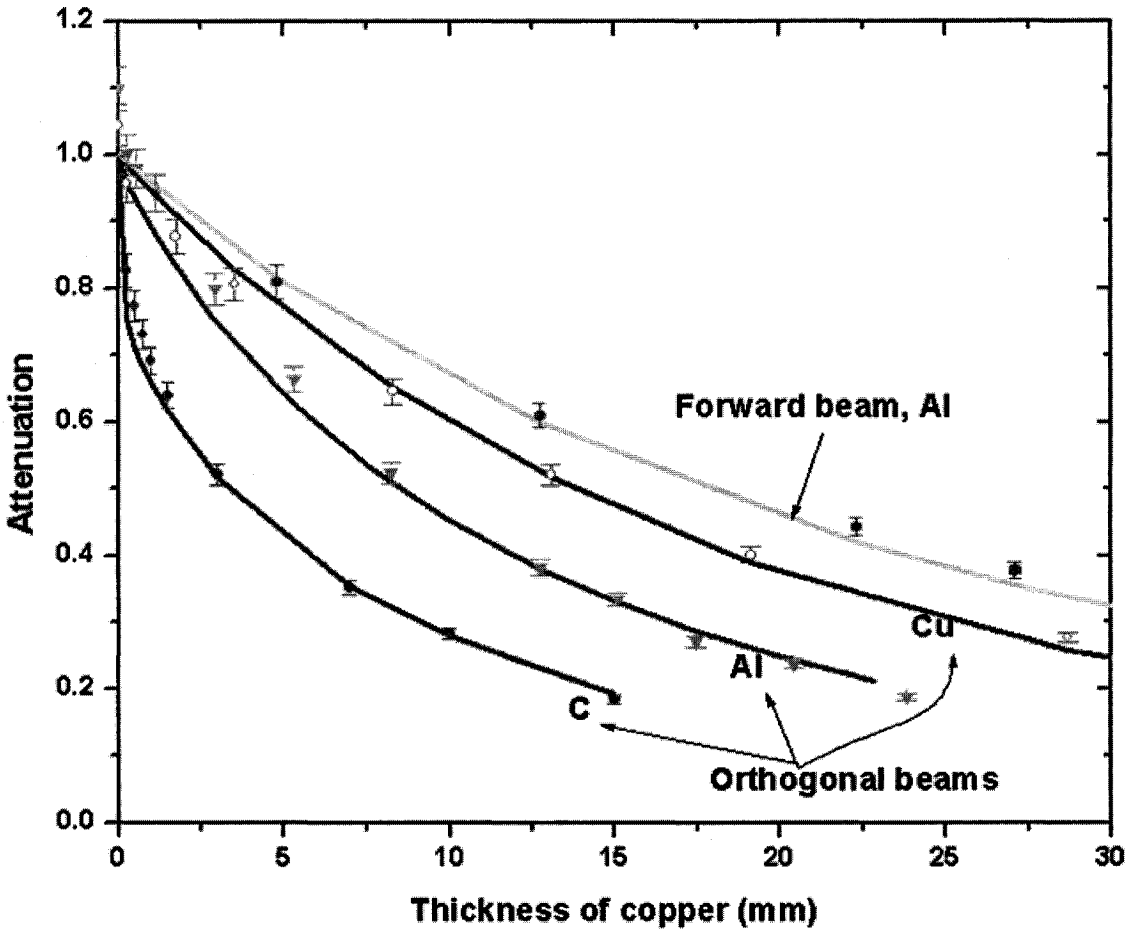

Figure 6.3: Measured and calculated attenuation curve data for the forward and orthogonal bremsstrahlung beams produced by a 10 MeV electron beam incident on carbon, aluminum and copper targets. For the forward beam, since the differences between attenuation curves of various targets were minimal, only results for the aluminum target are shown. The attenuation measurements for the forward beams are performed at a depth of 2.5 cm in solid water, as described in Chapter 5.

Similarly to our PDD experiment, the calculations and measurements of the beam attenuation agree well to within the uncertainty, except at very low thicknesses of the copper attenuator. Due to the energy deposition by the contaminating electrons in the chamber, the measurements at these points have larger values in comparison with the calculated values. We discuss this discrepancy in greater detail in Section 6.5. Here it suffices to say that the Monte Carlo attenuation calculations will be used to produce the HVL values for each of the beams. We have corrected our simulations such that the effect of contaminating electrons is not taken into account and the curves solely represent the attenuation of photons' spectra. As described in Chapter 5, although the percentage contribution of contaminating charged particles is very small (1% for the carbon target and up to 6.5% for the copper target), their effect on the dose reading can be significant if they are not filtered out of the beam. If the initial points in our experiment that are affected by the electron contamination were included during the HVL calculations, the HVL results would be smaller than expected and would falsely indicate a softer beam. In Fig. 6.3, the MC-calculated data have been normalized to the highest reading. The experimental results have been plotted such that the difference between the experimental and MC-calculated attenuation curves is minimized.

	Orthogonal		**Forward**	
	HVL_1 (mm copper)	HC	HVL_1 (mm copper)	HC
Carbon	3.29	0.41	16.09	0.86
Aluminum	8.50	0.75	17.66	0.90
Copper	13.78	0.89	17.30	0.91
CT quality	0.52	0.60		
X-ray quality	0.26	0.48		

Table 6.1: Experimental HVL and homogeneity coefficient (HC) values for orthogonal and forward beams produced by a 10 MeV electron beam incident on targets of carbon, aluminum and copper. Typical CT and x-ray quality beams have also been included for comparison purposes.

Table 6.1 shows the HVLs and homogeneity coefficient. The beam quality results of a typical CT beam produced by a 140 kVp tube with a tungsten target of 7 degrees tilt along with a 9 mm aluminum filter have also been shown[4]. The last entry corresponds to the beam quality results of a typical x-ray quality beam produced by a 120 kVp tungsten target of 7 degrees tilt along with a bowtie filter of graphite and aluminum[4]. Although some properties of these diagnostic beams will be noted and referred to throughout this chapter as a means of comparison between the orthogonal bremsstrahlung beams and a diagnostic quality beam, the reader must keep in mind that the purpose of this work is to investigate the potential use of orthogonal bremsstrahlung beams as an alternate means of imaging to the currently used megavoltage x-ray imaging. Thus, it is perhaps more reasonable to evaluate the beam qualities of orthogonal x rays against those of forward beams rather than against diagnostic kilovoltage beams. We do not claim in this work that the orthogonal bremsstrahlung photons are suitable replacements for diagnostic quality x rays.

6.4 Spectral measurements

Although the strong agreement between Monte Carlo-calculated and experimental results of PDD and attenuation may be used to demonstrate that our beam spectral calculations are accurate to within the uncertainty range, we decided to use our MC system to simulate the spectral distribution of the beams that were experimentally measured by Faddegon et al.[1]

The results of this comparison are shown in Fig. 6.4. The simulation conditions were matched with those experimentally used by the researchers including a 15 MeV electron beam striking three different target materials: beryllium, aluminum and lead.

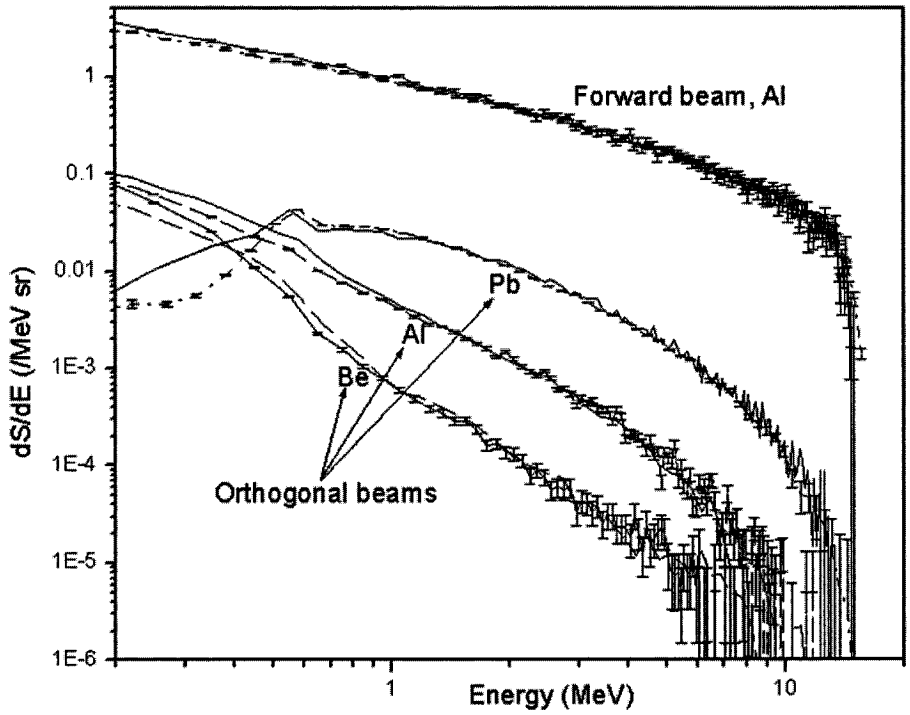

Figure 6.4: A comparison between our MC calculated spectral distributions (solid curves) and the experimentally measured spectra, as determined by Faddegon et al.[1](dotted curves). The error bars for the measured spectral points have been omitted for clarity.

The agreement between our calculated results and the Faddegon's measurements[1] is very promising and it serves as yet another confirmation that the EGSnrcMP code and our simulations are capable of accurate beam spectral calculations in both the forward and orthogonal directions. It is interesting to note that in the orthogonal direction for the lead target in the low energy range, our Monte Carlo-calculated spectrum agreed better with Faddegons's experimental measurements than did his own MC-calculated results (refer to Fig. 2.10(b)).

A number of factors may account for the greater accuracy of our calculations. We used a much lower energy cut-off than Faddegon. Moreover, the EGSnrcMP code used by our group has been improved significantly over the older EGS4 code that was used by Faddegon 15 years ago. Many new implementations including the PRESTA algorithm[5], the inclusion of angular distribution of bremsstrahlung photon[5], and the low energy photon cross section

enhancements[6] have made the EGSnrcMP code a more accurate code for dose and spectral calculations in the low energy ranges compared to the older EGS4 system.

Figure 6.5 displays our Monte Carlo-calculated spectra for the forward and orthogonal bremsstrahlung beams of 10 MeV electrons striking aluminum and carbon targets. The spectrum of the previously mentioned CT beam has also been included. Our experimental setup, as described in Chapter 5, was fully simulated to produce the spectral results shown in Fig. 6.5. Hence, the spectral distributions shown correspond to the beams described and analyzed in the previous two sections.

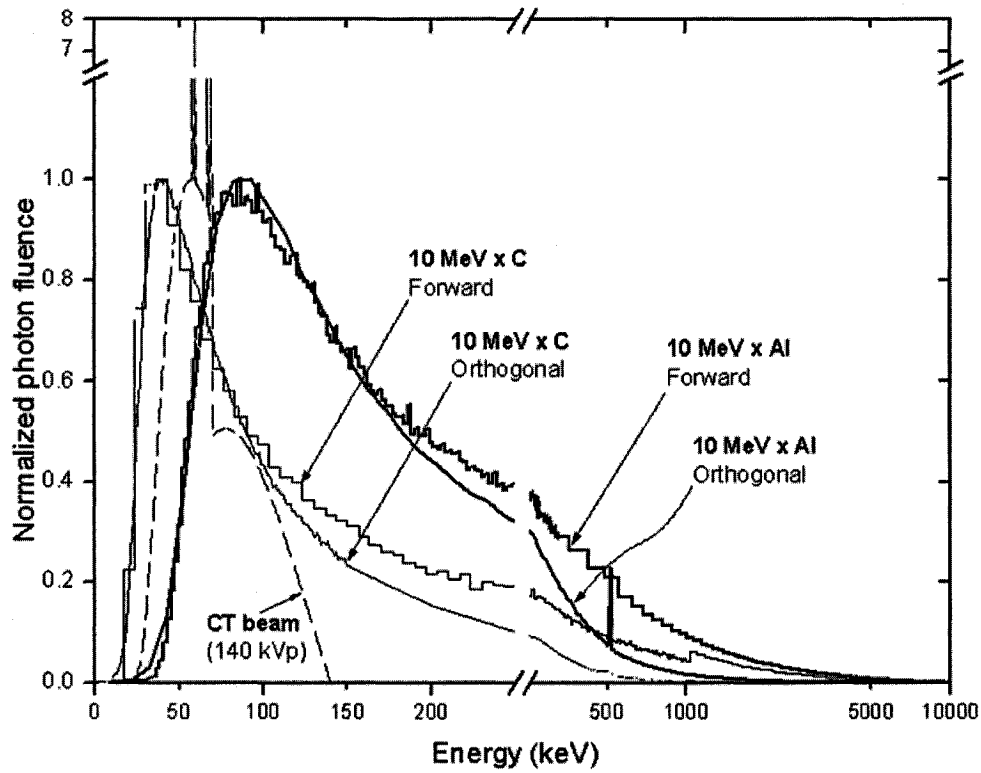

Figure 6.5: Spectral comparison between various MC-calculated orthogonal and forward beams studied in this work. All spectra have had their peak bremsstrahlung fluence renormalized to 1. The spectra correspond to those obtained by a 10 MeV electron beam striking an aluminum target (dark solid curves), and a carbon target (light solid curves). The spectra in both the orthogonal (smooth curve) and forward (steps) directions have been shown. The spectrum of a typical CT beam (dotted curve) has also been shown.

Table 6.2 demonstrates the mean and effective energies of the beams that we studied in this work. The photon yield is defined as the ratio of the number of photons produced to the total number of incident electrons on the target. The photon yield and mean energy have been determined using MC calculations. The same phase space used earlier for attenuation calculations was used to calculate the photon yield and mean energy. Only particles in an area of 1 cm radius around the central axis of the phase space file were used for the analysis. The effective energies were obtained from the HVL values listed in Table 6.1. In the forward direction, the uncertainty on the listed effective energies is relatively high because of the low sensitivity of the HVL measurements in high energy beams.

The significant reduction in the mean and effective energy of the orthogonal beams relative to the forward bremsstrahlung beams can readily be observed from Table 6.2. For instance, the effective energy of a beam produced by 10 MeV electrons striking a carbon target is ten times lower in the orthogonal direction than it is in the forward direction.

	Orthogonal			**Forward**		
	Mean Energy (keV)	Effective Energy (keV)	Photon Yield	Mean Energy (keV)	Effective Energy (keV)	Photon Yield
Carbon	207	151	1.7%	1015	1535	46.3%
Aluminum	411	425	1.9%	1424	1880	47.4%
Copper	1040	1107	4.8%	1754	1760	41.4%
CT beam (140 kVp)	69.7	59				

Table 6.2: Various beam quality measurement results for a 10 MeV electron beam incident on targets of carbon, aluminum and copper. The mean energy and photon yield are determined based on MC-calculated phase space data. The effective energy is determined using the measured HVL_1 values of various spectra.

A look at Fig. 6.5 explains the reasons for such marked differences between the effective energies of the orthogonal and forward beams, as well as the beams produced by various target materials. First, it is important to note, however, that the peak energy of a spectrum is essentially only a function of the target material's atomic number. We observed that the peak energy is not a function of angle and does not even depend strongly on the energy of the incident electron beam. Given our setup, the peak energy of a spectrum produced by a 10 MeV electron beam striking a carbon target was determined to be 40 keV, while for an aluminum target it was determined to be 90 keV. The peak energies of spectra produced by 6 MeV incident electrons were similar to those produced by 10 MeV electrons.

The reason for the difference in the effective energies of beams produced by different target materials can be attributed to both the differences in peak energy as well as the photon fluence drop-off at higher energies. It is evident from Fig. 6.5 that the contribution of high energy photons is markedly larger for a beam produced by an aluminum target than one produced by a carbon target.

The significantly lower effective energy of the orthogonal bremsstrahlung beams compared to the forward beams produced by the same target cannot, however, be attributed to the peak energy differences. On the other hand, it can be observed from Fig. 6.5 that the spectra of the forward beams drop much slower than those of the orthogonal beams. The more gradual fall-off corresponds to a greater contribution of high energy photons to the forward beam which in turn translates to higher mean and effective energies. We should emphasize that due to the use of a logarithmic energy scale past the breakpoint in Fig. 6.5, large differences in fluence drop may be underestimated, if care is not practiced.

Figure 6.6 shows the Monte Carlo-calculated mean energies of the orthogonal bremsstrahlung beams produced by 6 MeV and 10 MeV electrons striking ten different target materials.

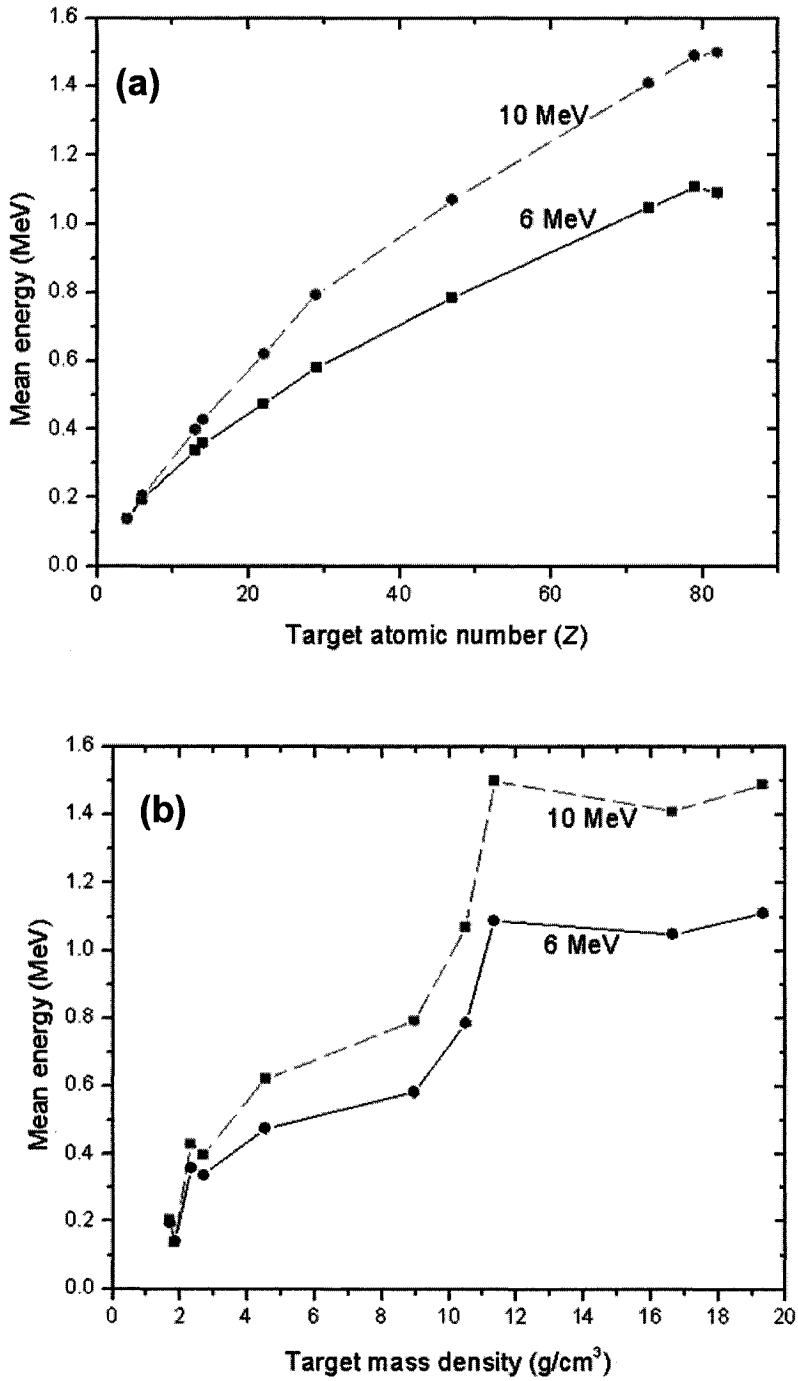

Figure 6.6: The Monte Carlo-calculated mean energies in the orthogonal direction as a function of target's atomic number (a) and target's mass density (b) for a 10 MeV incident electron beam (dashed curve) and a 6 MeV incident electron beam (solid curve). The incident electron beam has a radius of 1 mm. The phase space used to calculate the quantities was collected at 10 cm away from the edge of the target in the orthogonal direction. It has a half-width of 65% of the CSDA range of the primary incident electrons in the target material.

All the results in Fig. 6.6 have been obtained using the same simulation geometry as that described in Section 5.3.3, and used to study the dependence of the photon yield and electron contamination on target material. Since the mean energy is very dependent on the actual simulation setup, the absolute values listed in Fig. 6.6 are only accurate for the particular geometry that we simulated. As expected, the mean energy of the orthogonal component of the bremsstrahlung beam increases with the target's atomic number, as shown in Fig. 6.6(a). Moreover, for a given target, the mean energy of the resulting orthogonal x rays is higher for higher energy primary incident electrons. This is obvious, since the energy of the primary incident electrons directly determines the energy of the resulting bremsstrahlung photons. The higher the energy of the incident electrons, the greater the amount of energy that they can lose in an interaction to form bremsstrahlung photons. The dependence of mean energy on a target's mass density is interesting to note, however, because it reaches a maximum for targets of mass density around 11 g/cm^3. For targets of higher mass density, the mean energy seems to reach essentially a state of equilibrium, as shown in Fig. 6.6(b).

6.5 Photon yield and charged particle contamination

Since the eventual goal of this project is to use the orthogonal bremsstrahlung beams for improved imaging in radiotherapy, it is important to ensure that the photon yield is within acceptable range. A very low photon yield may result in unacceptably long exposure time requirements.

On the other hand, a large electron contamination may result in an undesirable increase in surface dose. From our experiments, the significant effect of the contaminating electrons on our results can be seen. In Fig. 6.1, it can easily be observed that the measured surface doses are much larger than the calculated

ones. It is only past the depth of maximum dose that the majority of contaminating electrons are removed, and the measurements and calculations start agreeing. The energy deposition in the build-up region by the low energy contaminating electrons often results in large discrepancies between measurements and calculations in this region. Although the aluminum filters used throughout the process greatly reduced the level of contamination, they did not eliminate it, especially, since filters can also be a source of electron production.

We already discussed in the context of Fig. 6.3 that the electron contamination results in a much higher reading for the first few points in the attenuation measurement. Especially, when no copper attenuator was used, the dose reading was up to 15% higher than the expected values. Due to the copper's high density, the majority of contaminating electrons were removed past a thickness of roughly 1 mm.

The absolute values of the photon yield and charged particle contamination are very much dependent upon the actual experimental or simulation setup. Therefore, the yield and contamination values that were listed in this section are only valid for the specific geometry and definition used to produce them. This is not to say that general trends and patterns cannot be drawn; in fact in this section, we will frequently refer to other papers to show similarities between our results and those of others.

6.5.1 *Dependence of yield and contamination on target thickness*

Figure 6.7 shows the results of our study of photon yield and electron contamination in the orthogonal direction as a function of target thickness. Figure 6.7(a) shows the behaviour of the two quantities for a large atomic number target (lead) and Fig. 6.7(b) shows the results for a low atomic number target (carbon).

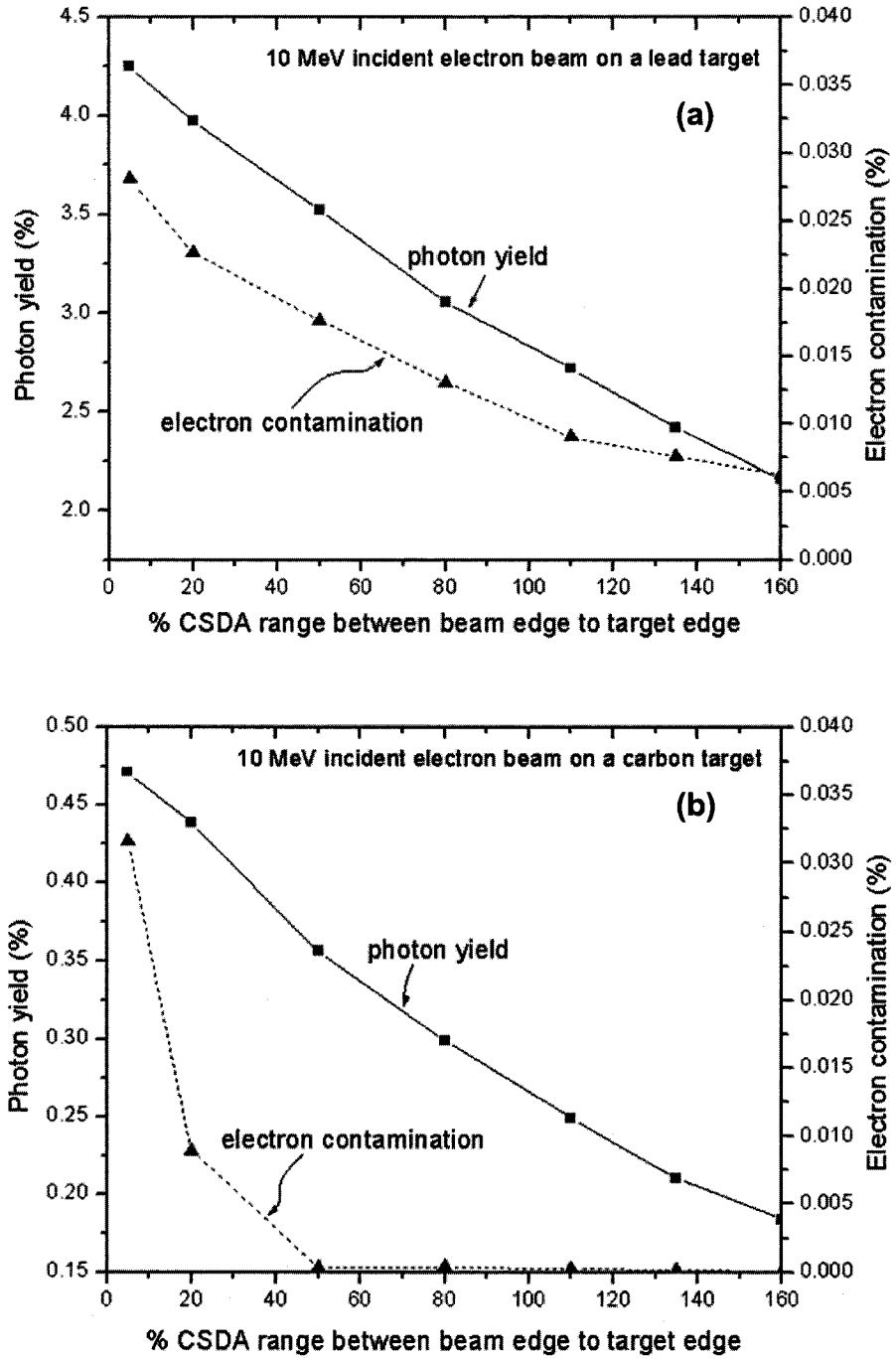

Figure 6.7: The Monte Carlo-calculated photon yield (solid curve) and electron contamination (dotted curve) for orthogonal bremsstrahlung beams produced by a 10 MeV electron beam striking a lead target (a) and a carbon target (b) as a function of target thickness. The incident electron beam has a radius of 1 mm. The phase space used to calculate the quantities was collected at 10 cm away from the edge of the target in the orthogonal direction. It has a half-width of 65% of the CSDA range of the primary incident electrons in the target material.

As we expect, in the orthogonal direction, the yield is much larger for higher atomic number targets than for lower atomic number ones for any given target thickness. Furthermore, the photon yield seems to drop linearly with target thickness regardless of target material. The percentage drop in the photon yield over the same range of target thicknesses, however, is slightly larger for smaller atomic number targets.

Nordell and Brahme[3] carried out a similar study of the photon yield in the forward direction for a 50 MeV electron beam incident on three different targets of tantalum, aluminum and carbon. They found that initially the yield increases sharply as a function of target thickness up to a maximum after which the x-ray yield drops linearly with any further increase in thickness. Two opposing effects determine the value of the photon yield: an increase in the thickness of target material results in an increased probability of bremsstrahlung photon production; however, it also results in an increased probability of photon attenuation in the larger thickness of material. As a result, a maximum is obtained when the two effects reach equilibrium.

Although in our experiment, the yield in the orthogonal direction was investigated, the same two factors mentioned above are responsible for determining its value. However, care must be practiced when interpreting our results. In the forward direction, the thickness of the target material is simply defined as the amount of absorbing material in front of the narrow incident electron beam, as shown in Fig. 2.13. However, in the orthogonal direction the situation is more complicated since the target thickness in the orthogonal direction is not the only parameter influencing the x-ray yield. The thickness of the material in the direction of the incident electron propagation also plays a role in the x-ray yield at 90°. Even if the target thickness in the orthogonal direction is small, given a large thickness of material in the forward direction, the yield at 90° may still be significant. It should be emphasized that the target thickness in the forward direction, in our

experiment, was kept at the 130% CSDA range of the incident electrons in the target material, as shown in Fig. 5.10.

The electron contamination at 90° also decreases with an increase in target thickness. This behaviour is expected because with an increase in thickness of the absorbing material in the orthogonal direction, a greater percentage of electrons will interact within the target and will never be able to leave the target. Our results suggest that the percentage of electron contamination drops more rapidly as a function of target thickness, expressed in terms of the CSDA range of the incident electron, for a carbon target than for a lead target.

The percentage of electron contamination escaping the target as a function of target thickness was also studied for 6 MeV electrons striking various target materials[7]. Figure 6.8 shows the results obtained. In the orthogonal direction for a 6 MeV electron beam striking targets of various atomic number, the relative contribution of electron contamination becomes insignificant for target thicknesses greater than 80% of the CSDA range of the electrons in the target material.

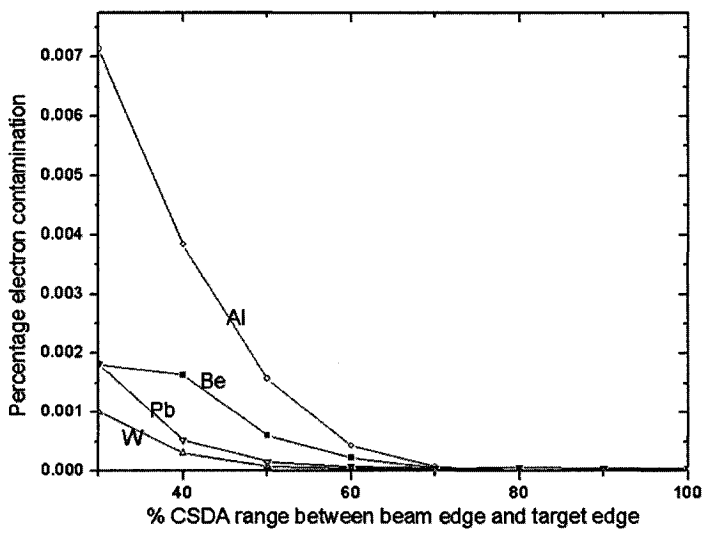

Figure 6.8: The calculated relationship between percentage electron contamination and target thickness for a 6 MeV incident electron beam on targets of tungsten (W), lead (Pb), aluminum (Al), and beryllium (Be).

6.5.2 *Dependence of yield and contamination on target material*

Our results from Table 6.2 show that in the orthogonal direction, the yield increases with the target's atomic number. In fact, given our specific setup geometry, a 10 MeV electron beam striking a copper target produces a fluence of photons three times larger than when it is made to strike a carbon target, as noted in Table 6.2. The reason for this phenomenon was explained by Podgorsak et al. [8] and is discussed in detail in Section 2.4.3. In short, in a high atomic number target, on the average, the electrons are deflected at larger angles than in a low atomic number target. These deviated electrons subsequently produce x rays in directions other than the forward direction.

In order to understand the dependence of the photon yield and electron contamination on target material better, a more robust experiment with ten targets using the geometry shown in Fig. 5.10 was performed. Figure 6.9 (a) and (b) display the results as a function of the atomic number and mass density of the target materials, respectively.

It is clear from Fig. 6.9(a) that in the orthogonal direction the photon yield increases with the atomic number of the target material. The change in yield as a function of target's atomic number seems to be larger for smaller Z targets and somewhat levels off for larger Z targets. The percentage of electron contamination leaving the target and reaching the phase space file also seems to be a function of target material and seems to follow generally the same trend as the yield. Percentage-wise, however, electron contamination increases much more rapidly than photon yield over the same range of atomic numbers. The yield from a lead target is 14 times that from a beryllium target, while the percentage of electron contamination leaving a lead target is roughly 90 times that of a beryllium target.

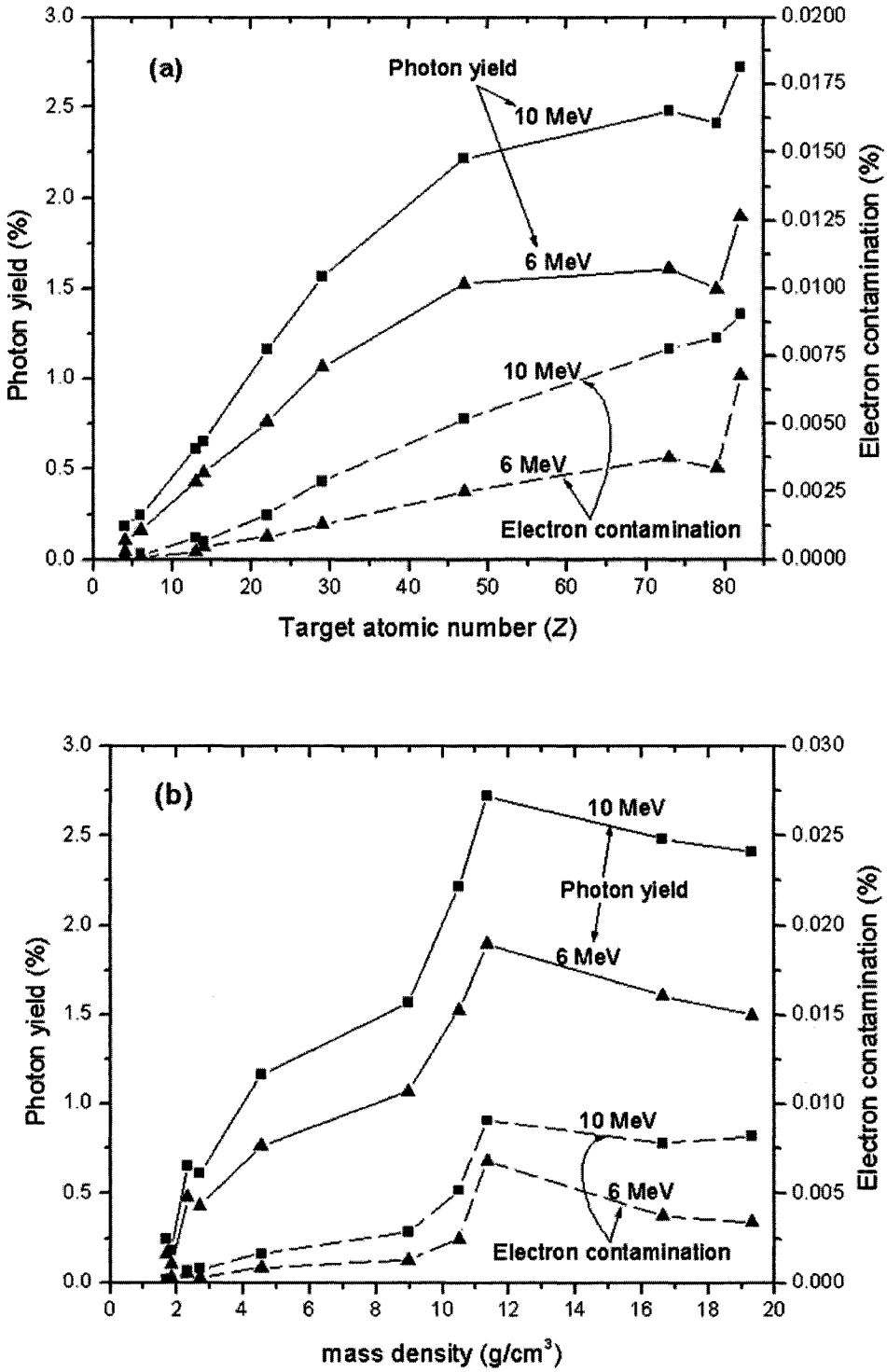

Figure 6.9: The Monte Carlo-calculated photon yield (solid curve) and electron contamination (dotted curve) in the orthogonal direction as a function of target's atomic number (a) and target's mass density (b) for a 10 MeV incident electron beam (square symbols) and a 6 MeV incident electron beam (triangle symbols).

The mean energy of the contamination electrons emerging from a lead target was found to be (1.0 ± 0.4) MeV, while for an aluminum target this was found to be (0.5 ± 0.4) MeV. Although it seems that the mean energy of the contaminating electron spectrum is also target dependent, this could not have been verified due to the high uncertainty on the mean energy values.

Figure 6.9(b) shows the photon yield and electron contamination as a function of mass density of the target material. The figure shows an increase of both x-ray yield and electron contamination as a function of mass density up to a value of roughly 11 g/cm^3 after which there is in fact a drop in both quantities. It is evident from all figures in this section that the photon yield and electron contamination are both larger for incident electron beams of higher energy.

6.6 Image contrast

In the previous sections, through various beam quality measurements and spectral distribution calculations, we established that the orthogonal component of bremsstrahlung beams produced by megavoltage electrons striking low atomic number targets can have effective energies in the kilovoltage range. Since we had proposed earlier to use this phenomenon to obtain higher-contrast images in radiotherapy, we will test our hypothesis by providing some of the images obtained using these beams.

Figure 6.10 displays the image contrast results obtained from imaging two simple contrast objects, as shown in Fig. 5.7, using the orthogonal or forward component of bremsstrahlung beams produced by 6 MeV electrons incident on an aluminum target. Figure 6.11 shows the image contrast results from a similar experiment that involved imaging the same two objects with orthogonal bremsstrahlung beams produced by 6 MeV electrons striking targets of carbon, aluminum and lead.

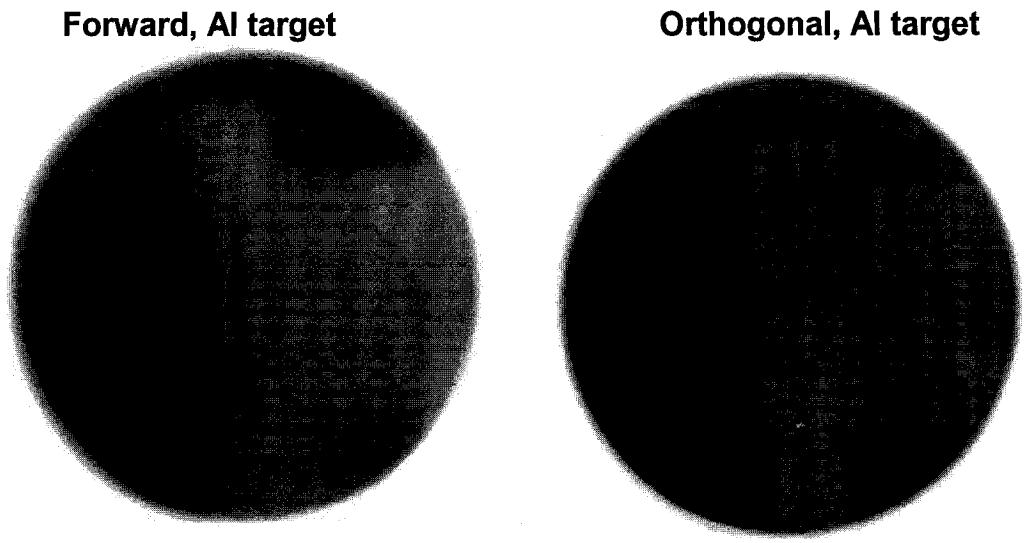

Figure 6.10: Image contrast results using Agfa 400 diagnostic films and the forward and the orthogonal component of a bremsstrahlung beam produced by 6 MeV electrons striking an aluminum target. Contrast test objects have been shown in Fig. 5.7. The image taken using the forward bremsstrahlung beam is intended to show the quality of current portal images.

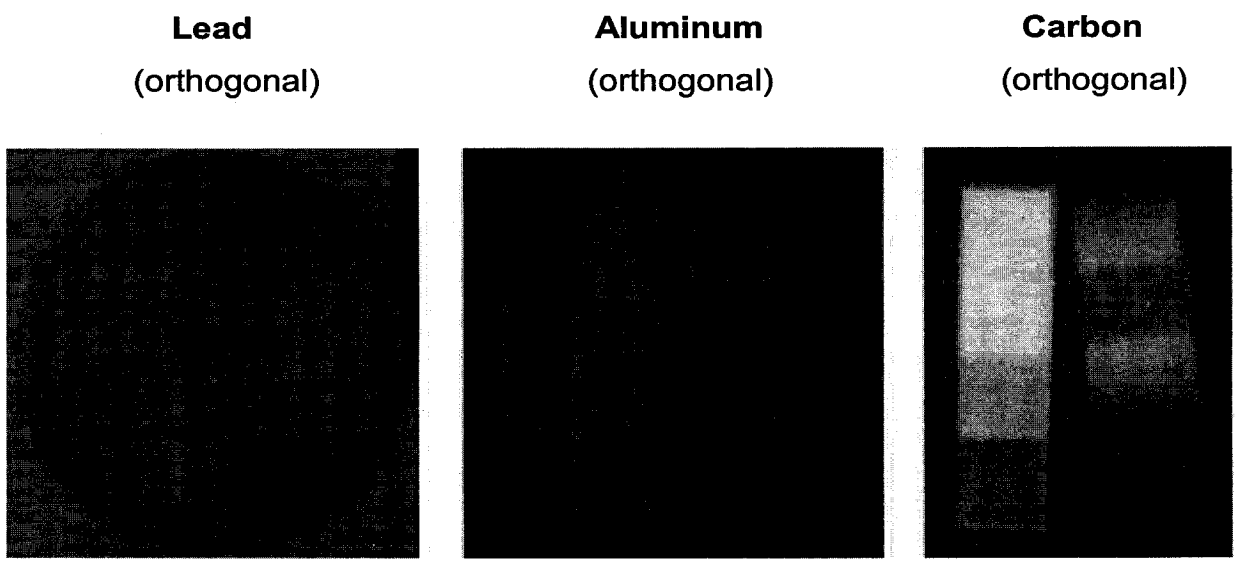

Figure 6.11: Image contrast results using Agfa 400 diagnostic films and the orthogonal component of bremsstrahlung beams produced by 6 MeV incident electron beams on targets of carbon, aluminum and lead. Contrast test objects are shown in Fig 5.7. The step object is made of PMMA with a density of 1.19 g/cm^3, and the cylindrical test objects is made of nylon with density 1.15 g/cm^3.

It is evident from both figures that the orthogonal bremsstrahlung beams produced by low atomic number targets result in images of much higher contrast than those produced by high atomic number targets or by forward beams. The grooves visible in the cylindrical test object when imaged by the orthogonal beam from a carbon target, as shown in Fig. 6.11, are only 0.7 mm thick. It is not a surprise, however, that such high contrast levels can be reached. We have already shown in previous sections that the effective energy of the orthogonal bremsstrahlung spectrum produced by 10 MeV electrons incident on a carbon target is only twice that of typical x-ray CT quality beams. For our setup, the effective energy of the orthogonal beam produced by 6 MeV electrons striking a carbon target (the same beam used to produce the images in Fig. 6.11) was determined to be 144 keV. Since the total mass attenuation coefficient is larger in the kilovoltage energy range than in the megavoltage energy range, for a given thickness of material, a kilovoltage beam undergoes a larger attenuation compared to a megavoltage beam. The significantly lower contrast of the images produced by megavoltage forward beams compared to the contrast of images produced by the kilovoltage effective energy orthogonal bremsstrahlung beams is a direct consequence of this phenomenon.

It can qualitatively be observed that the contrast level of the image produced by the orthogonal component of a lead target, Fig. 6.11, is not superior to the contrast level of the image taken using the forward bremsstrahlung beam from an aluminum target. This is expected because we already discussed that the effective energy of the orthogonal component of the bremsstrahlung beams produced by high atomic number targets is in the megavoltage range (see Fig. 6.6(a)). In fact, our PDD results from Fig. 6.2 as well as the effective energy results of Table 6.1 suggest that the difference between the effective energy of the orthogonal and forward beams becomes smaller for larger atomic number targets. Therefore, it is no wonder that the contrast levels of images taken with the orthogonal bremsstrahlung beams produced by high atomic number targets

are similar to the contrast levels achieved when imaging the objects with the forward beams.

Although not experimentally verified in this work, we believe that similar to other kilovoltage diagnostic x rays, orthogonal bremsstrahlung beams with kilovoltage effective energies produce images of enhanced soft-tissue contrast. The photoelectric effect is the main mode of interaction in the kilovoltage energy range, and because of the very strong atomic number dependence of the photoelectric mass attenuation coefficient, as described in Section 2.3.3, images taken with beams of kilovoltage effective energies can differentiate better between objects of slightly different effective atomic number. Soft tissues and fatty tissues, for example, have slightly different atomic number; however, when imaged with kilovoltage beams, the minor differences in the effective atomic number of these materials can in fact result in pronounced contrast differences. On the other hand, Compton interaction is the dominant mode of photon interaction in megavoltage energy ranges. However, the Compton mass attenuation coefficient is independent of the atomic number of the absorbing material. Hence, images taken with megavoltage effective energy x rays do not take advantage of the potential differences in the effective atomic number of the materials that are being imaged. Given objects of identical thicknesses, the contrast levels of images produced by megavoltage beams are solely determined by the differences in the electron densities of the objects. Since these differences are often very small, and the Compton mass attenuation coefficient is only linearly dependent on the electron density, the contrast levels achieved by megavoltage imaging is inferior to that achieved by kilovoltage imaging. This is indeed the greatest shortcoming of all high energy imaging techniques in radiotherapy. The significantly lower effective energy of orthogonal bremsstrahlung beams clearly overcomes this problem.

We have discussed earlier that the x-ray yield in the orthogonal direction is much lower relative to the yield in the forward direction. Nevertheless, we have

established that even the low photon fluence in the orthogonal direction is in fact large enough to produce high contrast images in relatively short periods of time. The longest exposure time required in this work to produce images of acceptable contrast level was 1.5 minutes when the linac was operated in the electron mode. However, if the linac was to be operated in the photon mode, the 1.5 minutes exposure time would be reduced to 0.09 seconds due to the much greater primary electron output in this mode. As a result, we conclude that high-contrast images can be obtained using the orthogonal component of bremsstrahlung beams from low atomic number targets in a fraction of a second.

6.7 References

1 B. A. Faddegon, C. K. Ross, and D. W. Rogers, "Angular distribution of bremsstrahlung from 15-MeV electrons incident on thick targets of Be, Al, and Pb," Med. Phys. **18**, 727-739 (1991).

2 E. B. Podgorsak, J. A. Rawlinson, and H. E. Johns, "X-ray depth doses from linear accelerators in the energy range from 10 to 32 MeV," Am. J. Roentgenol. Radium Ther. Nucl. Med. **123**, 182-191 (1975).

3 B. Nordell and A. Brahme, "Angular distribution and yield from bremsstrahlung targets," Phys. Med. Biol. **29**, 797-810 (1983).

4 K. Cranley, B. J. Gilmore, G. W. A. Fogarty, and L. Desponds, "Catalogue of Diagnostic X-ray Spectra and Other Data," Report No. 78. Institute of Physics and Engineering in Medicine (1997)

5 I. Kawrakow and D. W. Rogers, "The EGSnrc Code System: Monte Carlo Simulation of Electron and Photon Transport.," NRCC Report PIRS-701(A) Ionizing Radiation Standards National Research Council of Canada (2000)

6 Y. Namio, H. Hirayama, and S. Ban, "Improvements of low-energy photon transport in EGS4," Radiation Phys. Chem. **53**, 283-294 (1998).

7 K. Jabbari, E. B. Podgorsak, and J. Seuntjens, "Feasibility Study of Orthogonal Bremsstrahlung Beams for Improved Radiation Therapy Imaging," Med. Phys. **32**, 2022 (2005).

8 E. B. Podgorsak, J. A. Rawlinson, M. I. Glavinovic, and H. E. Johns, "Design of X-ray targets for high energy linear accelerators in radiotherapy," Am. J. Roentgenol. Radium Ther. Nucl. Med. **121**, 873-882 (1974).

Chapter 7

CONCLUSIONS

7.1 Thesis summary

The effective and mean energies of the forward and orthogonal component of bremsstrahlung beams produced by 10 MeV electrons striking targets of carbon, aluminum and copper were experimentally determined using percentage depth dose, as well as attenuation and half-value layer measurements. The experimental findings agreed well within the uncertainty range to the results obtained by Monte Carlo simulations. We established that the effective energy of the orthogonal bremsstrahlung beam is always lower than the forward component of the beam for a given target material and incident electron energy. Furthermore, larger atomic number targets produce higher effective energy beams at large angles.

In the orthogonal direction, beams with effective energies in the kilovoltage range can be obtained from megavoltage electrons striking low atomic number targets. We determined that such low energies are obtained not because of a shift in the peak energy of the spectrum, but rather because of a sharper fluence fall-off of the spectrum and a lower contribution of high energy photons to the overall beam make-up.

The photon yield and the percentage of electron contamination in the orthogonal direction were also studied with Monte Carlo. Results showed that both quantities decrease with the target thickness and increase with the target atomic number.

The images of few simple contrast objects were taken using both the forward and orthogonal component of the bremsstrahlung beams and the contrast levels of the images were qualitatively compared. We established that the orthogonal beams produced by low atomic number targets indeed result in contrast levels approaching those of diagnostic quality beams. The images produced using these beams resulted in a superior contrast relative to most common portal images.

It was further established that although the fluence of photons in the orthogonal direction is much lower than that in the forward direction, the yield is nevertheless large enough for imaging purposes as long as diagnostic quality films are used. We believe that images of acceptable contrast can be obtained in a fraction of second if the linac is operated in the photon mode.

7.2 Future work

This work completes the first phase of the feasibility study of the use of orthogonal bremsstrahlung beams for improved imaging in radiotherapy. It has been established and shown, both experimentally and using Monte Carlo calculations, that orthogonal bremsstrahlung beams can be a practical substitute for megavoltage beams as far as imaging in radiotherapy is concerned.

The next phase of this work involves the implementation of the technique. A prototype linac capable of orthogonal imaging needs to be designed and built. The degree of improvement in the quality of treatment care received by patients can only be measured if this technique is implemented in clinics under a carefully monitored protocol.

This work potentially opens the door for an integrated, linac-based cone beam imaging system without the need for additional x-ray generators and tubes.

BIBLIOGRAPHY

(N. B. The numbers in the square parentheses refer to the pages in which the references are cited)

1 F. H. Attix, Introduction to radiological physics and radiation dosimetry (Wiley, New York, NY, 1986).

[12,37,42]

2 M. J. Berger, "Monte Carlo calculation of the penetration and diffusion of fast charged particles," Methods Comput. Phys. **1**, 135-215 (1963).

[54]

3 M. J. Berger and S. M. Seltzer, "Etran, Monte Carlo Code System for Electron and Photon Transport Through Extended Media," Documentation for RSIC Computer Code Package CCC-107, Oak Ridge Natl. Lab, Oak Ridge, Tennessee (1973).

[55,56]

4 T. S. Curry, J. E. Dowdey, R. C. Murry, and E. E. Christensen, Christensen's physics of diagnostic radiology, 4th ed (Lea & Fabiger, Philadelphia, PA, 1990).

[7,49,51]

5 G. A. Ezzell, J. M. Galvin, D. Low, J. R. Palta, I. Rosen, M. B. Sharpe, P. Xia, Y. Xiao, L. Xing, and C. X. Yu, "Guidance document on delivery, treatment planning, and clinical implementation of IMRT: report of the IMRT Subcommittee of the AAPM Radiation Therapy Committee," Med. Phys. **30**, 2089-2115 (2003).

[3]

6 B. A. Faddegon, C. K. Ross, and D. W. Rogers, "Forward-directed bremsstrahlung of 10- to 30-MeV electrons incident on thick targets of Al and Pb," Med. Phys. **17**, 773-785 (1990).

[34]

7 B. A. Faddegon, C. K. Ross, and D. W. Rogers, "Angular distribution of bremsstrahlung from 15-MeV electrons incident on thick targets of Be, Al, and Pb," Med. Phys. **18**, 727-739 (1991).

[28,29,30,31,32,34,35,87,91]

8 R. L. Ford and H. M. Gerstenberg, "The EGS Code System (Version 3)," SLAC Rep. 210. Stanford University, Stanford, CA (1978).

[55]

9 A. Gustafsson, B. K. Lind, and A. Brahme, "A generalized pencil beam algorithm for optimization of radiation therapy," Med. Phys. **21**, 343-356 (1994).

[3]

10 International Atomic Energy Agency (IAEA), Radiation oncology physics : a handbook for teachers and students. E. B. Podgoršak (International Atomic Energy Agency, Vienna, Austria, 2005).

[11,15]

11 K. Jabbari, E. B. Podgorsak, and J. Seuntjens, "Feasibility Study of Orthogonal Bremsstrahlung Beams for Improved Radiation Therapy Imaging," Med. Phys. **32**, 2022 (2005).

[101]

12 H. E. Johns and J. R. Cunningham, The physics of radiology, 4th ed (Charles C. Thomas, Springfield, IL, 1983).

[37,42,43,44,47]

13 I. Kawrakow and D. W. Rogers, "The EGSnrc Code System: Monte Carlo Simulation of Electron and Photon Transport.," NRCC Report PIRS-701(A) Ionizing Radiation Standards National Research Council of Canada (2000)

[92]

14 F. M. Khan, The physics of radiation therapy, 2nd ed (Williams & Wilkins, Baltimore, MD, 1994).

[49]

15 K. M. Langen, J. Pouliot, C. Anezinos, M. Aubin, A. R. Gottschalk, I. C. Hsu, D. Lowther, Y. M. Liu, K. Shinohara, L. J. Verhey, V. Weinberg, and M. Roach, 3rd, "Evaluation of ultrasound-based prostate localization for image-guided radiotherapy," Int. J. Radiat. Oncol. Biol. Phys. **57**, 635-644 (2003).

[4,5]

16 C. C. Ling and P. J. Biggs, "Improving the buildup and depth-dose characteristics of high energy photon beams by using electron filters," Med. Phys. **6**, 296-301 (1979).

[44]

17 C. M. Ma and S. B. Jiang, "Monte Carlo modelling of electron beams from medical accelerators," Phys. Med. Biol. **44**, R157-R189 (1999).

[65]

18 R. Mohan, C. Chui, and L. Lidofsky, "Energy and angular distributions of photons from medical linear accelerators," Med. Phys. **12**, 592-597 (1985).

[30]

19 J. Morr, T. DiPetrillo, J. S. Tsai, M. Engler, and D. E. Wazer, "Implementation and utility of a daily ultrasound-based localization system with intensity-modulated radiotherapy for prostate cancer," Int. J. Radit. Oncol. Biol. Phys. **53**, 1124-1129 (2002).

[4]

20 Y. Namio, H. Hirayama, and S. Ban, "Improvements of low-energy photon transport in EGS4," Radiation Phys. Chem. **53**, 283-294 (1998).

[92]

21 B. Nordell and A. Brahme, "Angular distribution and yield from bremsstrahlung targets," Phys. Med. Biol. **29**, 797-810 (1983).

[30,36,37,87,100]

22 E. B. Podgorsak, Radiation physics for medical physicists (Springer, New York, NY, 2005).

[10,14,17,21,23,24,45]

23 E. B. Podgorsak, J. A. Rawlinson, M. I. Glavinovic, and H. E. Johns, "Design of X-ray targets for high energy linear accelerators in radiotherapy," Am. J. Roentgenol. Radium Ther. Nucl. Med. **121**, 873-882 (1974).

[28,30,31,33,34,102]

24 E. B. Podgorsak, J. A. Rawlinson, and H. E. Johns, "X-ray depth doses from linear accelerators in the energy range from 10 to 32 MeV," Am. J. Roentgenol. Radium Ther. Nucl. Med. **123**, 182-191 (1975).

[30,43,37,87]

25 B. W. Raaymakers, A. J. Raaijmakers, A. N. Kotte, D. Jette, and J. J. Lagendijk, "Integrating a MRI scanner with a 6 MV radiotherapy accelerator: dose deposition in a transverse magnetic field," Phys. Med. Biol. **49**, 4109-4118 (2004).

[4]

26 J. A. Rawlinson and H. E. Johns, "Percentage depth dose for high energy x-ray beams in radiotherapy," Am. J. Roentgenol. Radium Ther. Nucl. Med. **118**, 919-922 (1973).

[36]

27 D. W. Rogers and A. F. Bielajew, "Differences in electron depth-dose curves calculated with EGS and ETRAN and improved energy-range relationships," Med. Phys. **13**, 687-694 (1986).

[54,56]

28 D. W. Rogers and A. F. Bielajew, "Monte Carlo Techniques of Electron and Photon Transport for Radiation Dosimetry," Dosim. of Ion. Rad. **3**, 427-539 (1990).

[56]

29 D. W. Rogers, B. A. Faddegon, G. X. Ding, C. M. Ma, J. We, and T. R. Mackie, "BEAM: a Monte Carlo code to simulate radiotherapy treatment units," Med. Phys. **22**, 503-524 (1995).

[53,54,56]

30 D. W. Rogers, C. M. Ma, B. Walters, S. B. Ding, and G. Zhang, "BEAMnrc Users Manual," National Research Council of Canada Report **PIRS-0509** (2002).

[58]

31 M. Scheithauer, M. Schwedas, T. Wiezorek, A. Keller, T. G. Wnedt, and D. Harder, "Erhohung der Genauigkeit der Laplace-Transformations-methode zur Bestimmung des Bremsstrahlungsspektrums klinischer Linearbeschleuniger," Z. Med. Phys. **13**, 22-29 (2003).

[63]

32 J. R. Sykes, H. V. James, and P. C. Williams, "How much does film sensitivity increase at depth for larger field sizes?," Med. Phys. **26**, 329-330 (1999).

[66]

33 D. L. Van den Berge, M. D. Ridder, and G. A. Storme, "Imaging in radiotherapy," Eur. J. Radiol. **36**, 41-48 (2000).

[3]

34 F. Verhaegen, A. E. Nahum, S. Van de Putte, and Y. Namito, "Monte Carlo modelling of radiotherapy kV x-ray units," Phys. Med. Biol. **44**, 1767-1789 (1999).

[58]

35 F. Verhaegen and J. Seuntjens, "Monte Carlo modelling of external radiotherapy photon beams," Phys. Med. Biol. **48**, R107-R164 (2003).

[54,56,58,75]

36 A. B. Wolbarst, Physics of radiology (Medical Physics Pub., Madison, WI, 2000).

[48,50,51]